Julius-Maximilians-Universität Würzburg
Graduate School of Science and Technology

Doctoral thesis / *Dissertation*

for the doctoral degree / *zur Erlangung des Doktorgrads*

Doctor rerum naturalium (Dr. rer. nat.)

Enhancement of geometric complexity and predictability of melt electrowriting for biomedical applications

Fortentwicklung von geometrischer Komplexität und Kalkulierbarkeit des Melt Electrowriting für biomedizinische Anwendungen

Submitted by / *Vorgelegt von*

Andrei Hrynevich

from / *aus*

Minsk

Würzburg, 2020

Submitted on / *Eingereicht am*:
…….

Stamp / *Stempel* Graduate School

Members of thesis committee / *Mitglieder des Promotionskomitees*

Chairperson / *Vorsitz*:
…….....

1. Reviewer and Examiner / *1. Gutachter und Pürfer:*
……..

2. Reviewer and Examiner / *2. Gutachter und Pürfer:*
……..

3. Examiner / *3. Prüfer:*
.....

Additional Examiners / *Weitere Prüfer*:
.....

……
……

Day of thesis defense / *Tag des Promotionskolloquiums:*
…….

Die vorliegende Arbeit wurde in der Zeit von November 2015 bis Januar 2020 am Lehrstuhl für Funktionswerkstoffe der Medizin und der Zahnheilkunde der Julius-Maximilians-Universität Würzburg unter der Betreuung von Herrn Prof. Dr. Paul D. Dalton angefertigt.

Abstract

This thesis encompasses the development of the additive manufacturing technology melt electrowriting, in order to achieve the improved applicability in biomedical applications and design of scaffolds. Melt electrowriting is a process capable of producing highly resolved structures from microscale fibres. Nevertheless, there are parameters influencing the process and it has not been clear how they affect the printing result. In this thesis the influence of the processing and environmental parameters is investigated with the impact on their effect on the jet speed, fibre diameter and scaffold morphology, which has not been reported in the literature to date and significantly influences the printing quality. It was demonstrated that at higher ambient printing temperatures the fibres can be hampered to the extent that the individual fibres are completely molten together and increased air humidity intensifies this effect. It was also shown how such parameters as applied voltage, collector distance, feed pressure and polymer temperature influence the fibre diameter and critical translation speed. Based on these results, a detailed investigation of the fibre diameter control and printing of scaffolds with novel architectures was made. As an example, a 20-fold diameter ratio is obtained within one scaffold by changing the collector speed and the feed pressure during the printing process. Although the pressure change caused fibre diameter oscillations, different diameter fibres were successfully integrated into two scaffold designs, which were tested for mesenchymal stromal cell suspension and adipose tissue spheroid seeding. Further design and manufacturing aspects are discussed while jet attraction to the printed structures is illuminated in connection with the fibre positioning control of the multilayer scaffolds. The artefacts that appear with the increasing scaffold height of sinusoidal laydown patterns are counteracted by layer-by-layer path adjustment. For the prediction of a printing error of the first deposited layer, an algorithm is developed, that utilizes an empirical jet lag equation and the speed of fibre deposition. This model was able to predict the position of the printing fibre with up to ten times smaller error than the of the programmed path. The same model allows to qualitatively assess the fibre diameter change along the nonlinear pattern as well as to indicate the areas of the greatest pattern deformation with the growing scaffold height. Those results will be used in the later chapters for printing of the novel MEW structures for biomedical applications. In the final chapter the concept of multimodal scaffold was combined with the suspended fibre printing, for the manufacturing of the MEW scaffolds with controlled

pore interconnectivity in three dimensions. Those scaffolds were proven to be a promising substate for the control of the neurite spreading of the chick DRG neurons.

Zusammenfassung

Diese Arbeit umfasst die Entwicklung der additiven Fertigungstechnologie Schmelzelektroschreiben, um die verbesserte Anwendbarkeit in biomedizinischen Anwendungen und die Konstruktion von Gerüsten zu erreichen. Schmelzelektroschreiben ist ein Verfahren, das in der Lage ist, hochaufgelöste Strukturen aus mikroskaligen Fasern zu erzeugen. Dennoch gibt es Parameter, die den Prozess beeinflussen, und es ist nicht klar, wie sie sich auf das Druckergebnis auswirken. In dieser Arbeit wird der Einfluss der Verarbeitungs- und Umweltparameter mit der Auswirkung auf deren Einfluss auf die Polymerstrahlgeschwindigkeit, den Faserdurchmesser und die Gerüstmorphologie untersucht, was bisher in der Literatur nicht berichtet wurde und die Druckqualität wesentlich beeinflusst. Es konnte gezeigt werden, dass bei höheren Umgebungstemperaturen die Entstehung von zylindrischen Fasern soweit behindert werden können, dass die einzelnen Fasern vollständig zusammengeschmolzen werden und eine erhöhte Luftfeuchtigkeit diesen Effekt verstärkt. Es wurde auch gezeigt, wie solche Parameter wie angelegte Spannung, Kollektorabstand, Vorschubdruck und Polymertemperatur den Faserdurchmesser und die kritische Translationsgeschwindigkeit beeinflussen. Basierend auf diesen Ergebnissen, wurde eine detaillierte Untersuchung der Faserdurchmessersteuerung durchgeführt und Gerüsten mit neuartigen Architekturen wurden gedruckt. Als Beispiel wird ein 20-fach Durchmesserverhältnis innerhalb eines Gerüstes durch die Änderung der Kollektorgeschwindigkeit und des Vorschubdrucks während eines Druckvorgangs erreicht. Obwohl die Vorschubdruckveränderung spürbare Oszillationen des Faserdurchmessers verursachte, wurden Fasern mit unterschiedlichen Durchmessern erfolgreich in zwei Scaffoldmuster integriert, die für mesenchymale Stromazell und L929 Zellsuspension und die Aussaat von Fettgewebe-Sphäroiden getestet wurden. Weitere Design- und Herstellungsaspekte werden diskutiert, während die Polymerstrahlanziehung auf die gedruckten Strukturen in Verbindung mit der Faserpositionierungssteuerung der mehrschichtigen Scaffolds beleuchtet wird. Den Artefakten, die mit zunehmender Gerüsthöhe sinusförmiger Ablagemuster auftreten, wird durch schichtweise Anpassung von Verfahrweg des Kollektors entgegengewirkt. Für die Vorhersage eines Druckfehlers der ersten abgelegten Schicht wurde ein Algorithmus entwickelt, der die empirischen Zusammenhänge zwischen Kollektorgeschwindigkeit, Nachlauf, und die Geschwindigkeit der Faserablage verwendet.

Dieses Modell war in der Lage die Position der gedruckten Faser mit einem bis zu zehnmal kleinerem Fehler als die Position auf dem programmierten Pfad vorherzusagen. Dasselbe Modell erlaubt es, die Änderung des Faserdurchmessers entlang des nichtlinearen Musters qualitativ zu bewerten und die Bereiche mit der größten Musterdeformation mit zunehmender Gerüsthöhe anzuzeigen. Diese Ergebnisse werden in anderen Kapiteln für den Druck der neuartigen MEW-Strukturen für biomedizinische Anwendungen verwendet. Im letzten Kapitel wurde das Konzept des multimodalen Gerüstes mit dem Druck von hängenden Fasern kombiniert, um MEW-Gerüste mit kontrollierter Porenvernetzung in drei Dimensionen herzustellen. Diese Gerüste erwiesen sich als vielversprechendes Substrat für die Kontrolle der Neuritenausbreitung der Nervenzellen aus Spinalganglien.

List of Publications

As the first author:

1. **Hrynevich, A.**, Elçi, B.Ş., Haigh, J.N., McMaster, R., Youssef, A., Blum, C., Blunk, T., Hochleitner, G., Groll, J. and Dalton, P.D., 2018. Dimension-Based Design of Melt Electrowritten Scaffolds. Small, 14(22), p.1800232.

2. Liashenko, I.*, **Hrynevich, A.***, Dalton P.D., Designing Outside the Box: Unlocking the Geometric Freedom of Melt Electrowriting using Microscale Layer Shifting. Advanced Materials, 2020, 2001874.

3. **Hrynevich, A.***, Liashenko, I.*, Dalton P.D., Accurate prediction of melt electrowritten pattern from simple geometrical considerations. Advanced Materials Technologies, 2020, 2000772.

4. **Hrynevich, A.,** Achenbach, P., Jüngst, T., Brook, G., Dalton, P.D., Design of Suspended Melt Electrowritten Fiber Arrays for Schwann Cell Migration and Neurite Outgrowth. Macromolecular Bioscience, 2021, 2000439.

*Equal contribution

As a co-author:

5. Hochleitner, G., Youssef, A., **Hrynevich, A.**, Haigh, J. N., Jungst, T., Groll, J., & Dalton, P. D., 2016. Fibre pulsing during melt electrospinning writing. BioNanoMaterials, 17(3-4), 159-171.

6. de Ruijter, M., **Hrynevich, A.**, Haigh, J. N., Hochleitner, G., Castilho, M., Groll, J., Malda, J. and Dalton, P. D., 2018. Out-of-Plane 3D-Printed Microfibers Improve the Shear Properties of Hydrogel Composites. Small, 14(8), 1702773.

7. Schaefer, N., Janzen, D., Bakirci, E., **Hrynevich, A.**, Dalton, P. D., & Villmann, C., 2019. 3D Electrophysiological Measurements on Cells Embedded within Fiber-Reinforced Matrigel. Advanced healthcare materials, 8(5), 1801226.

8. McMaster, R., Hoefner, C., **Hrynevich, A.**, Blum, C., Wiesner, M., Wittmann, K., Dargaville, T.R., Bauer-Kreisel, P., Groll, J., Dalton, P.D. and Blunk, T. 2019., Tailored Melt Electrowritten Scaffolds for the Generation of Sheet-Like Tissue Constructs from Multicellular Spheroids. Advanced healthcare materials, p.1801326.

9. Kotz, F., Risch, P., Arnold, K., Sevim, S., Puigmartí-Luis, J., Quick, A., Thiel, M., **Hrynevich, A.**, Dalton, P.D., Helmer, D. and Rapp, B.E., 2019. Fabrication of arbitrary three-dimensional suspended hollow microstructures in transparent fused silica glass. Nature Communications, 10(1), p.1439.

10. Youssef, A., **Hrynevich, A.**, Fladeland, L., Balles, A., Groll, J., Dalton, P.D. and Zabler, S., 2019. The Impact of Melt Electrowritten Scaffold Design on Porosity Determined by X-Ray Microtomography. Tissue Engineering Part C: Methods, 25(6), pp.367-379.

11. Tylek, T., Blum, C., **Hrynevich, A.**, Schlegelmilch, K., Schilling, T., Dalton, P.D. and Groll, J., 2019. Precisely defined fiber scaffolds with 40 µm porosity induce elongation driven M2-like polarization of human macrophages. Biofabrication, 12, 025007

12. Bakirci, E., Schaefer, N., Dahri, O., **Hrynevich, A.**, Strissel, P., Strick, R., Dalton, P.D., Villmann C., 2020. Melt Electrowritten In Vitro Radial Device to Study Cell Growth and Migration. Advanced Biosystems. 2000077.

13. Großhaus, C., Bakirci, E., Berthel, M., **Hrynevich, A.**, Kade, J.C., Hochleitner, G., Groll, J., Dalton P.D. Melt electrospinning of 275 nm diameter fibers from medical-grade poly(ε-caprolactone) with a modified nozzle. Small 2020, 2003471.

14. Kim, J., Bakirci, E., O'Neill, K., **Hrynevich**, A., Dalton, P.D. Fiber bridging during melt electrowriting and the influence of fiber diameter and wall height. Macromolecular Materials and Engineering (submitted to Macromolecular Materials and Engineering).

All listed first author publications have been partially used in this work. The permission for the material reuse was obtained from the respective copyright owning publishing companies. Each taken or adapted figure contains an additional reference in the caption.

Contents

List of Abbreviations

3D – three-dimensional

ANOVA – Analysis of variance

CAD – Computer-aided design

CTS – Critical translation speed

DAB – 3,3'-Diaminobenzidine

DMEM – Dulbecco's modified eagle medium

DRG – Dorsal root ganglion

ECM – extracellular matrix

FCS – Foetal calf serum

FDM – Fused deposition modelling

hASC – human adipose stem cell

HBSS – Hanks balanced salt solution

hMSC – human mesenchymal stromal cell

IF – Immunofluorescent

JCP – Jet contact point

L – Lag

L_{stable} – Stable lag

L_{FJ} – ‚Falling jet' lag

MEW – Melt electrowriting

MFS – Minimal fibre spacing

NP – Nozzle position

PCL – poly (ε-polycaprolactone)

PBS – Phosphate buffer saline

PBS-T – Phosphate buffer saline with 0.5% Triton X-100

rH – Relative humidity

RL – Ray length

SD – Standard deviation

SEM – Scanning electron microscopy

SF – Suspended fibre

SR – Speed ratio

TE – tissue engineering

UV – Ultraviolet

V_{MA} – Move away speed

V_{NP} – Nozzle position speed

V_{JCP} – Jet contact point speed

ε – Minimal lag

Chapter 1: Introduction

1.1 From implants to scaffolds in biomedicine

Medical implants have been continuously improving with new material and processing availability. In ancient times, flax and plant fibres were used as sutures to repair open wounds but were replaced with refined materials such as silk or catgut threads. Such an evolution can be seen for many types of medical implants, including the metal screws and plates for fracture treatment in the 20th century [1] now being replaced with customized additively manufactured products. Alongside the development of the orthopaedic implants, other medical devices were appearing and in the 1952 the first polymeric hernia mesh was implanted [2]. These textile-based implants aided in mechanical functionality or structural stability, and the idea that structures made of biomaterials can aid in healing and regeneration of various tissues and organs emerged. Nowadays medical implants have become a major medical products class [2], with a clear regulatory path to their use in humans. With the expanding spectrum of available materials and structures, medical and scientific application of scaffolds has broadened: It has become possible to investigate cell and tissue behaviour in controlled geometrical conditions, both *in vitro* and *in vivo*. After successful research and development, these benefits can be applied in a clinical setting [3, 4].

While the implants with porous microstructure, which allow cell infiltration, have already proven their benefits in promoting healing primarily for bone defects in clinical conditions [2], the implants targeting other tissues and organs are still in different research stages, with only a few of them, e.g. vascular stents [5], reaching clinical trials. Such constructs, that are meant to introduce a specific engineered three-dimensional (3D) environment for the cells are called scaffolds. Scaffolds manufactured of appropriate biomaterials can either directly serve as an implant or be modified by additional bioactive substances or cells and maturated in a bioreactor. A field of tissue engineering (TE) is dealing with such modifications [6] which promise greater healing potential in contrast to scaffolds alone. Nevertheless adding biologically active substances (hormones, signalling molecules, drugs) and, especially, living cells makes the clinical translation problematic in contrast to scaffolds manufactured of the known biomaterials and by manufacturing processes, which do not affect the chemical composition of the material [7].

The original idea of a perfect scaffold was of one that can copy the structure and composition of the natural extracellular matrix (ECM) of the replaced tissue as close as

possible [4]. As a result, scaffolds made of biological biomaterials and decellularized tissues and organs were a subject of a comprehensive research [8, 9]. However, several disadvantages, including high variability in natural biomaterials, immunogenicity, and the deficit of organs for decellularization incentivised the utilization of synthetic biomaterials [10]. Replication of the ECM with synthetic materials is challenging due to imperfection of manufacturing methods with limited resolution and processable materials range. As a consequence, parallel to the attempts for accurate ECM reproduction, scaffold designs with various architectures and material compositions have been developed aimed to obtain the necessary properties for the tissue regeneration despite the little resemblance to the original ECM [11].

The properties, required for the successful scaffold functioning, include the bulk materials biocompatibility and mechanical properties (stiffness, yield strength, fatigue resistance etc.) [12, 13] as well as the scaffold shape and microarchitecture [14-16] and even surface roughness on a micro- and nanoscale level [17]. Important integral parameters of the scaffolds, that depend on its architecture, are porosity and pore interconnectivity. They characterize the volume that can be infiltrated by the host body's own or preliminary seeded cells and can vary significantly, depending on the required properties and the manufacturing method. The size and shape of the pores is important as well – it was found to influence the cell behaviour, including motility [18], proliferation [19], matrix deposition [20], differentiation [21] and polarization [22].

Due to a complex interplay between the scaffold parameters and the biological outcomes, scaffolds design can be a challenging task. Thus, the same mechanical properties of a scaffold can be achieved by choosing a stiffer material and highly porous microstructure or having a softer material with higher material fraction or different pore shape. Therefore, scaffolds with similar bulk properties can demonstrate different biological outcomes [23]. An accurate control over the cell behaviour through mechanical stimuli typically requires the finite element method (FEM) analysis of the stress distribution in the scaffold [24]. From some scaffolds it is required to provide the topographical cues to guide the cells migration, growth and orientation [25-27].

Scaffold degradation is an additional factor that needs to be taken into account for the constructs made of biodegradable materials: The mechanical stiffness and strength of such an

implant is decreasing with time and degradation products are being released. Ideally the scaffold degradation speed needs to be matched to the speed of the tissue healing and ECM deposition [28]. Again, the speed of the degradation can be dramatically different between the biomaterials and depends on the structure as well [29] e.g., through the wall thickness or structure induced cellular activity [30].

All in all, it is both the bulk properties of the scaffold biomaterial and its nano- and microstructure define the scaffold behaviour and the body response to it [31]. Although scaffolds can invoke certain adverse effects after implantation, including unwanted immune reactions, prevention of cell to cell contact and nutrient diffusion, and toxic degradation products [32], scaffolds stay a leading topic in TE research [33] despite the appearance and development of scaffold-free TE approaches [34].

1.2 Scaffold manufacturing strategies

With the variety of scaffold manufacturing technologies such as phase separation, salt leaching, gas foaming and electrospinning it has become possible to generate structures with very different geometries and feature sizes [35]. Yet, within each of those technologies the morphology spectrum was quite narrow. For instance, while electrospinning generates thin sheets with fibre diameters in the nanometre to micrometre range, there is limited control on the fibre positioning and scaffold porosity. On the contrary, in the scaffolds produced by salt leaching the pore sizes are defined through the appropriate salt grain selection but the polymer fraction still has a statistical thickness distribution instead of fully 3D controlled architecture.

Despite an ongoing development of these techniques, it is the adaptation of additive manufacturing technologies for biomedical applications, which provided additional interest in TE scaffold development [36, 37]. In additive manufacturing, objects are created by introducing material in a layer-by-layer manner. A further step forward is provided by the techniques which enable the assembly of the TE construct building blocks into an object simultaneously in three dimensions [38, 39].

As mentioned above, next to the scaffold mechanical properties and material biocompatibility, scaffold porosity, pore size and interconnectivity are considered critically important characteristics of a scaffold [35]. The generative principle of structure forming in

additive manufacturing technologies allows the formation of a microstructure with the fully adjustable geometry. This shape freedom can be utilized to facilitate the population of the scaffold by different kinds of cells and control their behaviour, simultaneously acting as a load bearing structure and maintaining nutrients and oxygen supply. From the comparatively simple melt extrusion printed scaffolds [28] for bone TE, scaffold architectures evolved into complex, mathematically defined shapes, optimized for mechanical strength and perfusion [40]. The resolution of some additive manufacturing technologies, such as two photon polymerization stereolithography, allows to include designed topographic elements with the size comparable to the cell dimensions for precisely defined single cell microenvironments [41]. Nevertheless, every additive manufacturing technology has its limitations in terms of resolution, object size, production performance, materials, and microstructure [42]. Thus, the extremely high resolution of the two photon polymerization is balanced by the limited specimen dimensions [43], manufacturing speed [44] and high equipment costs. Relative affordability of extrusion-based methods comes along with the comparatively large minimal feature size [45] due to the Barus effect [46].

1.3 Melt electrowriting

Melt electrowriting (MEW) is a technique, that combined the melt electrospinning ability to produce polymer fibres in the micrometre sizes, with a direct writing approach for production of biomedically relevant 3D scaffolds [47]. The MEW printed objects occupy a niche of high resolution scaffolds with practically unlimited size in two dimensions [48] and extremely high porosity [49], which can be made from a wide and constantly expanding range of available materials. Due to the utilization of polymer melts, minimal complications are expected for the MEW manufactured products market admission, ensuring a straightforward pathway from research to a customized medical device manufacturing [2].

Currently, MEW scaffolds are actively applied in the studies, related to cartilage replacement [50], cardiovascular [51-53], musculoskeletal [54, 55], neural [56] and adipose TE [57]. Next to the work on potentially implantable medical devices, MEW meshes have been utilized as substrates for immune cell therapy strategies [58] and cancer research [59].

As other additive manufacturing technologies, MEW has its limitations, related to the physics of the process and the technology development stage. The thickness of the MEW scaffolds that can be printed without manufacturing defects has a limit of several millimetres

to centimetres and depends on the pore size, which, in turn, also cannot be indefinitely small [60, 61]. Printing with a continuous fibre with a diameter that cannot be immediately changed and has a non-infinitesimal bending radius applies certain boundaries on the feature sizes, shapes and scaffold design in general. Therefore, most of the MEW scaffold architectures are represented by orthogonal fibre lattices and only few alternative geometries have been so far presented [62, 63].

The aim of this research was to further increase the accuracy and predictability of fibre diameter and positioning in MEW so that novel TE scaffold architectures, containing different fibre sizes and patterns, including overhanging structures could be manufactured and tested in cell and tissue culture.

Chapter 2: Theoretical concepts of Melt Electrowriting

2.1 Physical background of electrospinning and MEW

In MEW, under the influence of a strong electrical filed, a polymer melt, extruded from a nozzle forms a Taylor cone [64] and is drawn to the collecting surface, in the form of a gradually thinning jet, where it is deposited on a collector, moving in a plane [47]. Due to the similar process of the jet formation, the physical principles of melt electrowriting can be described, using the literature on the solution and melt electrospinning, taking into consideration the changes in the applied materials and processing setup where the jet is additionally subjected to mechanical tension.

There are several electrohydrodynamic phenomena that need to be highlighted to appreciate the similarity and difference between electrospinning and MEW. Firstly, since the fluids used for both solution and melt electrospinning are usually dielectric, the leaky dielectric mathematical model, developed by Melcher and Taylor [65], where charged species are able to move within the material and accumulate at the surface of the fluid in the presence of a strong electric field, can be applied. It is this phenomenon that Faraday discovered in the 19th century. The jet is formed as a result of shear stresses, induced by the electrostatic force, counteracted by the surface tension and viscosity [66, 67].

For electrospinning, a high charge density on the surface of a fluid column becomes a reason for bending instabilities [68] (also termed whipping) causing the well-known effect of random reposition of nanofibers (Figure 2.1A, B) [69]. High viscosity of polymer melts not only resists Rayleigh instabilities but also, counteracts the bending instabilities of a thinning jet [70], thus elongating the straight segment length.

Due to the presence of a straight segment with a length up to several centimetre, where surface charges in a fluid column suppress the surface tension driven Rayleigh instabilities [64] do not interact strongly enough to cause bending instabilities, a fluid column can be direct written at low flow rates. By moving the collector surface closer to the nozzle where the fluid emerges, it is possible to accurately place this jet onto a collector with good prediction (Figure 2.1C). Depending of the collector speed, the deposition patterns in this case are defined by the programmed collector path alone or in combination with the intrinsic jet buckling pattern [71] and insulating effect of the deposited fibres [72].

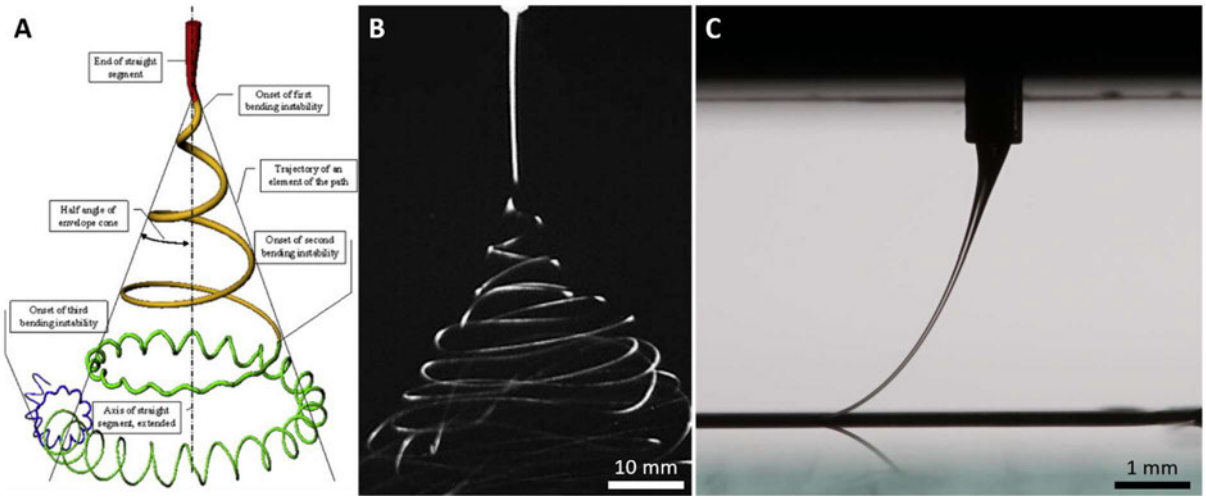

Figure 2.1. Electrically charged jets. A: A schematic, demonstrating stable region and bending instabilities for electrospinning. B: A photographic image of an electrospinning jet. C: Image of a jet during MEW. (A, B: Copyright Elsevier, taken from Ref. [73] and adapted from Ref. [74] respectively).

Mathematically the flow of an incompressible Newtonian fluid can be represented by an equation combining the gradient of the pressure and the divergence of the Maxwell stress tensor:

$$\rho \frac{D\boldsymbol{u}}{Dt} = -\nabla p + \nabla \cdot \sigma^M + \mu \nabla^2 \boldsymbol{u} \quad (2.1)$$

where q is the fluid density, $\boldsymbol{u}$ is the fluid velocity, p is the fluid pressure, and μ is the dynamic viscosity. Transformation of the gradient and Maxwell tensor equation members highlights the body forces acting on the charges by the electrical field and accelerating the fluid [75]:

$$\rho \frac{D\boldsymbol{u}}{Dt} = -\nabla \left[p - \frac{1}{2} \varepsilon_0 \rho \left(\frac{\partial \varepsilon}{\partial \rho} \right)_T \boldsymbol{E} \cdot \boldsymbol{E} \right] - \frac{1}{2} \varepsilon_0 \mathbf{E} \cdot \mathbf{E} \nabla \varepsilon + \rho^e \boldsymbol{E} + \mu \nabla^2 \boldsymbol{u} \quad (2.2)$$

where ε_0 is the permittivity of vacuum, ε is the permittivity of the fluid, $(\partial\varepsilon/\partial\rho)_T$ is the partial derivative at constant temperature, $\mathbf{E}$ is the electrical field, and ρ^e is the local free charge density.

The electrical field, charge density, temperature, and mechanical properties of a polymer in a MEW jet are not uniform and depend on the printing material, setup, and conditions. This means that a correct mathematical description requires inclusion of these effects. Although there is a limited amount of data on the MEW physics explicitly, the

processes of jet charging are deemed equivalent to the ones described for electrospinning and electrohydrodynamics in general. The mechanisms of the jet cooling and solidification have been previously studied for melt electrospinning and fibre deposition on the moving collector is considered similar to the fall of viscous fluids and elastic rods on a moving belt.

2.1.1 Charge induction, transmission, and dissipation

Charges can be injected into the liquid dielectric material by two mechanisms: dissociation [76] and electronic emission [77]. Electronic emission typically occurs under the local field strength above 10^8 V/m when the quantum tunnelling effect becomes possible [75, 78]. The maximal electric field strength can be estimated by an equation for a tip-plane configuration [79]:

$$E_{Tip} = \frac{2V}{r\ ln(1 + \frac{4d}{r})}, \quad (2.3)$$

where V is applied voltage, r – tip radius, d – distance to the collector or by finite element analysis [60]. In both cases the obtained values are around 10^7-10^8 kV/m. Since the emission mechanism was previously observed for typical solution electrospinning conditions [80] (13.5 kV applied voltage, 15.5 mm collector distance), it is possible that charge emission can also happen during MEW. The ion dissociation mechanism was described for polar [81] and non-polar [76] liquids and is intensified in the presence of an electrical field [82]:

$$K(E) = K(0)\exp\frac{2q^{2/3}(E/\varepsilon)^{1/2}}{kT}, \quad (2.4)$$

where *K(0)* is a dissociation constant in the absence of an external electric field, *q* is the electronic charge, *ε* is the relative permittivity, *k* is the Boltzmann constant and *T* is the polymer temperature.

Several mechanisms have been described for the transport and storage of charges in the jet and deposited fibres. The injected charges are transported inside the material by the fluid movement and via conduction. Apart of that, a fraction of them can be dissipated in the form of corona discharge, surrounding the jet [83]. The solidified fibres contain the charges, trapped in the in the bulk of the polymer and on the fibres' surface, bound to the surface defects, impurities and adsorbed molecules [84]. For instance, in solidified semi-crystalline polymers, charges can be trapped in the amorphous regions between the spherulites and in

the spherulite core itself [85]. After solidification charge transport in the polymer occurs differently for electrons and holes and is facilitated by the motility of the polymer chains [86, 87]. Removal of the charges from the deposited fibres on the collector can undergo either through conduction or the discharge between the fibres and the collector [88], while the conduction component for dielectric jet materials plays a significantly smaller role. The charge transmission to the collector depends on the collector properties as well as air humidity [89, 90]. Thus, a non-conductive collector induces fibres to retain the residual charges and prevents fibre stacking. The progression of the charge decay suggests that the surface charges are removed from the fibres much faster than the ones, trapped in the bulk of the polymer [91, 92] which could stay in the polymer for days. The transport processes could be accelerated with higher temperature [93] and surrounding air humidity [94, 95].

2.1.2 Jet cooling and solidification

Parallel to the jet elongation and thinning its temperature is decreasing and when it falls below the melting point the crystallization can start. Depending on polymer type, the speed of crystallization can affect the mechanical properties of the jet. For slowly crystallizing materials it is sufficient to consider the general viscosity growth with the temperature decrease along the jet for an adequate mathematical description of the process. Then a Giesekus constitutive model can be used for the simulation of viscoelastic [96]. For quickly crystallizing polymers it is required to take into account the crystal density and growth rate, which, next to the temperature, is affected by the shear due to the flow induced crystallization phenomenon [97]. The crystallization rate in this case was estimated by an equation for the crystallization degree ϑ [98]:

$$v\frac{d\theta}{dz} = (1-\theta)N\left[2A_f G\right], \quad (2.5)$$

where v is the average polymer velocity, z is the distance from the nozzle and A_f is the jet cross-section area. Crystal growth rate G and crystallization centres density N can be calculated, using the data, preliminary obtained by the polarized optical microscopy [99] and digital scanning calorimetry [100] respectively. The obtained data can be then substituted into the Phan-Thien and Tanner constitutive model [98].

The same group described a mechanism for the jet cooling, termed electrohydrodynamic quenching [101]. It explains the significant difference between the measured jet temperature and modelling result, calculated for temperature exchange by convection and radiation only. Furthermore, this effect can be either amplified by a higher applied voltage and humidity or disrupted by an external air flow, providing addition ways to control the fibre solidification.

2.2 Fibre deposition

By adding an XY stage, a direct writing principle was added first to solution [102, 103] and later to melt electrospinning [47]. The solution electrohydrodynamic printing, also sometimes called near field electrospinning or mechano-electrospinning, was initially focused on the printing of single layer patterns for electronics and, up to now, a only a little amount of complex 3D architectures has been demonstrated, despite the known stacking ability [104, 105]. Although solution-based electrohydrodynamic printing allows a wider range of available materials [106], it is the absence of toxic solvents that facilitated the rapid expansion of biomedical applications for MEW and moved its progress towards increased accuracy and complexity of the printed structures.

The behaviour of viscous liquid columns and elastic rods, falling on a moving collector was shown to be dependent on the collector speed [107]. When the collector was moving faster than the speed of the flow in the point where the fluid encounters the collector surface, further referred to as jet speed, the liquid was deposited as straight line [108]. Collector movement at lower speeds lead to the jet buckling and deposition of various periodic patterns [109]. In MEW the collector speed at which the transition from the coiling behaviour to the straight fibre deposition happens is called critical translation speed (CTS) [110].

Both coiling and straight fibre printing approaches have been applied in MEW [63, 111]. Despite of a relative variety of ‘natural’ coiling patterns, their limited range of shapes and sizes, pattern instability [112] and unpredictable stacking [113], scaffolds with patterns, consisting of parallel straight fibre arrays [114] have been mostly utilized. When structure-induced mechanical properties or cell alignment is required, non-linear patterns, programmed by the collector movement are preferred, although accurate and reproducible printing of such patterns requires additional effort in collector path programming and parameter adjustment [52, 115].

2.3 MEW processing principles

A schematic for MEW is presented in Figure 2.2A. The extruded polymer melt under a high voltage, applied between the nozzle and the collector, forms a Taylor cone, which is then stretched further and accelerated towards the collector, where it is deposited in a programmed manner as micrometre size fibres, which can be stacked to form 3D structures. The following aspects are deemed important for the MEW processing [116]: The polymer, work zone setup, processing parameters and environmental factors. The division between those factor groups is not strict but is introduced for a clear distinguishing between them in the text below.

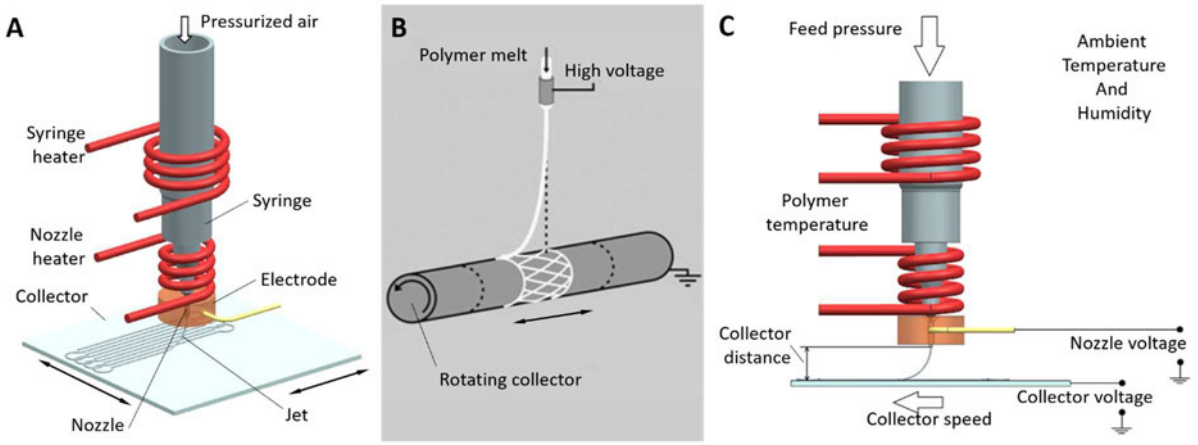

Figure 2.2. Schematics of MEW configurations. A: MEW configuration with a flat collector, moving in XY plane. B: Schematic of MEW with a rotating collector, installed on a translating stage. C: MEW processing parameters and ambient conditions (B: Copyright AIP Publishing. Adapted from Ref. [117]).

2.3.1 Materials

The used polymer melt not only defines the final mechanical and morphological properties of the scaffold but can affect the processability in terms of polymer degradation, stacking behaviour and diameter stability [118]. In general, to be processable by MEW, the material must have a melting point below the thermal degradation onset and have appropriate viscosity and chain entanglement to form a stable jet.

Polymer, to which MEW owns a significant part of its success is ε-Polycaprolactone (PCL). Its properties, such as high thermal stability, low melting point and glass transition temperature, combined with biocompatibility were a reason behind a wide use in extrusion

printing, melt electrospinning and MEW for biomedical applications [119]. The list of other materials, successfully processed by MEW includes polyoxazolines [110, 120], polypropylene [121], poly(vinylidene difluoride) [122], poly(methyl methacrylate) [123], thermoplastic elastomers [113], polymer blends [124, 125] and copolymers [126].

2.3.2 Setup

The setup features usually include the nozzle and surrounding electrode geometry, collector material and shape and their mutual arrangement. Kinematically, two different MEW setups have been presented so far, with a collector, moving in a plane and a manually set or perpendicularly moving printing head [47, 110, 126, 127] or with a rotating cylindrical collector(Figure 2.2B) , installed on a planar stage [117, 128, 129]. The nozzle size is chosen, regarding printing of different fibre diameters. Advanced nozzle systems (coaxial, pin electrode) may be applied for multi-material printing or additional charge injection for obtainment of thinner fibres [130, 131]. Typical collecting substates are represented by conductive (e.g., stainless steel, Indium tin oxide coated glass, titanium), semiconductor (silicone) and insulating (glass, polystyrene, polylactic acid) materials [63, 89, 90]. The use of non-conductive collectors eliminates the risk of electric breakdown [132] but can lead to the worsened charge transition from the fibres and excessive residual charge accumulation, leading to the fibre repulsion [90] and jet disturbance in the most critical cases. The shape of the collector is normally flat, which not always corresponds to the shape of the desired implant or scaffold. Printing on various 3D surfaces is possible as well [89, 133], yet it requires appropriate adjustment of the printing toolpath, including head movement along the Z-axis.

2.3.3 Processing parameters

The list of processing parameters comprises factors that can be readily changed immediately prior or during the printing and includes polymer temperature and flow rate (usually defined by the feed air pressure), collector distance and voltage applied to the nozzle and the collector (Figure 2.2C). For the materials, sensitive to the water presence in the air, pressurized atmospheric air can be replaced by an inert gas [121].

From the printing process requirements, the collector distance for MEW needs to be within the stable jet length range and be able to maintain sufficient field strength, preventing the fibre pulsing effects [134, 135]. It can span the values starting from 1 mm or lower up to

more than 20 mm. There is no exact rule or a formula for the collector distance calculation. When the collector distance in set constant during the printing, it should exceed the final construct height by a sufficient distance for the jet to form (approximately 1-2 mm) and avoid attraction of the deposited fibres by the nozzle and surrounding electrode. When a MEW printer has a motorized Z-axis for changing of the collector distance along with the scaffold height increase, the starting collector distance can be reduced in order to fulfil other requirements, such as minimal fibre spacing (see Chapter 3). Since the collector distance affects the jet velocity, the maximal speed acceleration of the XY stage have to be taken into account to enable collector movement above the jet speed [47]. The applied voltage, in combination with the collector distance controls the field strength. Increased voltage also makes the jet diameter more stable and increases the jet speed [136].

Polymer feed rate is controlled by the feed air pressure, nozzle diameter and polymer temperature. Changing the feed rate via the feed pressure is a straightforward way for predictable fibre diameter adjustment (Chapter 4). The upper and lower boundaries are defined by the zone of the stability of the jet [134]. The decrease in viscosity, caused by a higher polymer temperature also leads to the diameter increase but the collateral impact on the fibre morphology (Chapters 3 and 7) implies that the temperature is not an optimal parameter for diameter control.

The fastest way to change fibre diameter is through the variation of collector speed. The mechanical stretching of the jet starts when the collector is moving faster than the jet speed and no diameter increase is possible by further collector speed drop. The fibre thinning is in theory limited only by the XY-stage characteristics. For actual scaffold printing, the size of the scaffold needs to be taken into account (see Chapter 6) due to the delay of the diameter change after the corresponding acceleration or deceleration [137]. Although direct writing is usually done with the speed, exceeding the jet speed, in order to avoid fibre buckling, the repeatability of buckling patterns can be sufficient to use the printing regimes below the jet speed for manufacturing of scaffolds with adjustable mechanical properties [113].

Ambient conditions, including temperature and humidity require climate control environment for their systematic study. Due to equipment costs and relative steadiness and repeatability of a MEW process under a wide range of processing parameter combinations,

only a few studies have investigated the influence of the environmental conditions on the printing results [116].

Since MEW scaffolds are built of a continuous fibre, singe fibre diameter and morphology are the major readouts in most of MEW-related studies as it influences the mechanical properties, scaffold porosity and scaffold wall topography, relevant for the biomedical applications. General scaffold morphology of simple scaffolds with no overhanging structures can be assessed by optical or electronic microscopy while for scaffolds with more complex architecture and a proper assessment of the gaps between the individual fibres micro-computed tomography is preferred [114, 138].

Chapter 3: Development of MEW printers and influence of process and environmental parameters

3.1 Introduction

As a multiparametric process, MEW printing can be performed under different configurations [139]. These include the nozzle [61, 140] and collector geometry [89], processing parameters [63] and materials used [118]. The MEW processing parameters, as described in Chapter 1, control the morphology of the fibres, including fibre diameter and cross-section shape, printing pattern, and the geometrical fidelity of the scaffolds. In the vast majority of previous MEW studies, the polymer feed rate is controlled by the applied gas pressure (air, nitrogen, etc.), nozzle diameter and, indirectly, by the melt temperature that affects the flow rate though melt viscosity. The collector distance and voltage set the electric field strength, that draws the Taylor cone and thus define the balanced limits of the material flow rate. Furthermore, a dynamic electric field, which changes during printing, can result in a maximal scaffold thickness of up to 7 mm [60]. The influence of those parameters on the fibre and scaffold morphology has been thoroughly tested in multiple studies [47, 116, 141-144]. The most important readouts, relevant to the applications are the fibre diameter and scaffold fidelity. Therefore, such parameters as fibre feed pressure, temperature and collector speed are routinely investigated, whereas the influence of the collector distance and voltage polarity is less common. It is important to mention, that most of the experimental data was obtained for PCL as a printing material. It is incorrect to automatically extrapolate these results onto other materials because the same parameter changes can lead to a different outcome due to different rheological, electrical, and other physical properties. For instance, a reverse effect to the typically observed decrease of CTS [140] with the pressure growth was observed during the MEW processing of certain thermoplastic elastomers [113].

In contrast to the processing parameters mentioned above, experimental investigations of the environmental parameters, such as air temperature and humidity surrounding the jet have been usually neglected. The reason for this is that the typical laboratory microclimate conditions allow the MEW processing without a clear adverse effect on the results in the certain range of temperatures and humidity values [145]. Therefore, in contrast to solution electrospinning [146], less attention has been paid to the environmental parameter investigation and development of climate-controlled MEW printers [147]. No significant influence of the humidity was found on the fibre diameter and morphology [145] as well as the morphology of the scaffold, that could be detected by SEM and micro-computed

tomography. Nevertheless, the humidity levels as well as polymer and ambient temperatures, used in the study do not allow to claim that this absence of a visible effect can be transferred to all parameter combinations. The ambient temperature, which also defines the temperature of the collector in most of the MEW printers, might seriously affect the cooling rate of the jet. Together with the variability in the actual polymer temperature in the heater, different ambient conditions might result in the dispersion of the experimental results from different groups and even withing the same laboratory.

Next to the environmental conditions, another instrumental parameter, applied voltage polarity, was a subject of the investigation for a few numbers of studies only. In one of them [148], negative voltage and grounded collector were compared, while the total voltage difference was kept constant. In this case no conclusive difference was presented for a bioglass-filled PCL as a printing material. Another study demonstrated also the absence of the effects of the voltage configuration on the pure PCL fibre diameter [149]. However, it was shown that the application of the positive voltage to the nozzle and negative voltage to the collector improved the ordering degree in thick (up to 2 mm) PCL scaffolds with a box lattice structure.

An adverse effect of the tendency of the fibres to stack is the limitation of minimal distance at which the fibres can be placed on the collector and stacked next to each other: An attempt to position the fibres closer results in fibre stacking. Analysing the printing conditions for the scaffolds, provided in the literature, one can infer that smaller fibre spacing correlates with smaller collector distance, an accordingly lowered voltage, and thinner fibres (Table 3.1). It is, however, premature to claim that there is a direct connection between those parameters and achievable minimal scaffold pore sizes since in none of the studies it is explicitly stated. The minimal distance at which fibres can be positioned next to each other on the collector surface is termed the minimal fibre spacing (MFS). In addition to that, the ability to position fibres at a certain distance on the collector does not automatically mean that the fidelity of the scaffold will be maintained with additional deposited layers [60]. A typical scenario is when, after a certain height, the probability of fibre deposition, dislocated relative to their designed location starts rapidly growing [60, 149]. If the collector distance is kept constant and the polymer temperature is sufficiently high, melting of the fibres in the upper layers can result [149].

Depending on the specific polymer type and the nature of the collector, fibres can also be randomly located [110] or even actively repelled from each other [90]. Therefore, potentially, by controlling the conductivity of the polymer or the substrate, it might be possible to enable an accurate positioning of the fibres at a deliberate distance from each other while maintaining the ability to stack fibres vertically. In theory it is possible to adjust this effect to the point when the fibre-fibre interaction is small in comparison to the attraction of the fibre to the collector, however this is difficult to achieve due to the fact that there are multiple factors influencing the charge transmission and dissipation from the deposited fibre.

Table 3.1. MEW scaffold pore sizes and corresponding processing parameters

#	Fibre diameter [µm]	Height [layers]	Voltage [kV]	CD [mm]	Speed [mm/min]	Spacing [µm]	Reference
1	0.82 ± 0.16	50	2.9	1.5	5500	90	[150]
2	11.23 ± 0.53	5	4.5	2.5	600	125	[114]
3	10	10	4.6	3	1000	125	Chapter 4
4	20 ± 1.5	>300	7.1-12	8-18	-	1000	[60]
6	19.76 ± 1.54	30	6	4		250	[51]
7	3.59±0.62 to 22.9±0.53	5	4.7	3	1500	100	[151]
8	4.01 ± 0.06	40	10	20	1020	100*	[152]
9	10	10	3	3	1000	100	[153]
10	10	10	4	4	1000	200	[56]
11	2.6±0.2 to 2.9±0.3	10-30	4	1.4	950	40-100	[61]
12	-	-	9	8	850	200	[154]
13	10	10	9	12	2000	200	[48]
14	7	16	5.6	4.5	3500	100	[155]
15	3.89 ± 0.23	30	5	4	1800	200	[57]

Another unique feature of MEW, printing with ultrathin fibres, has a negative perspective when manufacturing productivity is considered. In case of a conventional single nozzle setup the manufacturing speed is solely defined by the collector speed. It is confined by the stage dynamic characteristics: maximal speed and acceleration. Straightforward

increase of the printing speed can cause deviations of the printed fibre position from the programmed path [52]. As discussed in detail in Chapter 6, this deviation depends on the difference between the printing speed and the CTS. Therefore, for the increase of the MEW productive capacity, a higher jet speed is beneficial. Along with that, the parameter adjustments for jet speed increases are to be made, considering that parameters that change the jet speed also influence the fibre and scaffold morphology. For example, after increasing the polymer melt temperature to increase the jet speed, it must be ensured, that no excess fibre melting occurs.

3.2 Materials and methods

MEW printer: A custom-made MEW printer (Figure 3.1) was developed and built in collaboration with FSKZ e. V. and Max Lamb GmbH & Co. KG. PSK040-NN-1 axes are responsible for collector movement in the XY plane and the movement of the printing head along the Z-axis and controlled by a IndraControl L45 system via Indra Drive Cs servomotor drivers (all from Bosch Rexroth AG, Germany). High voltage sources (HCP 140-20000, FuG Elektronik GmbH, Germany), temperature and pressure controllers are connected to the CNC controller, allowing the change of those parameters from the motion control programs.

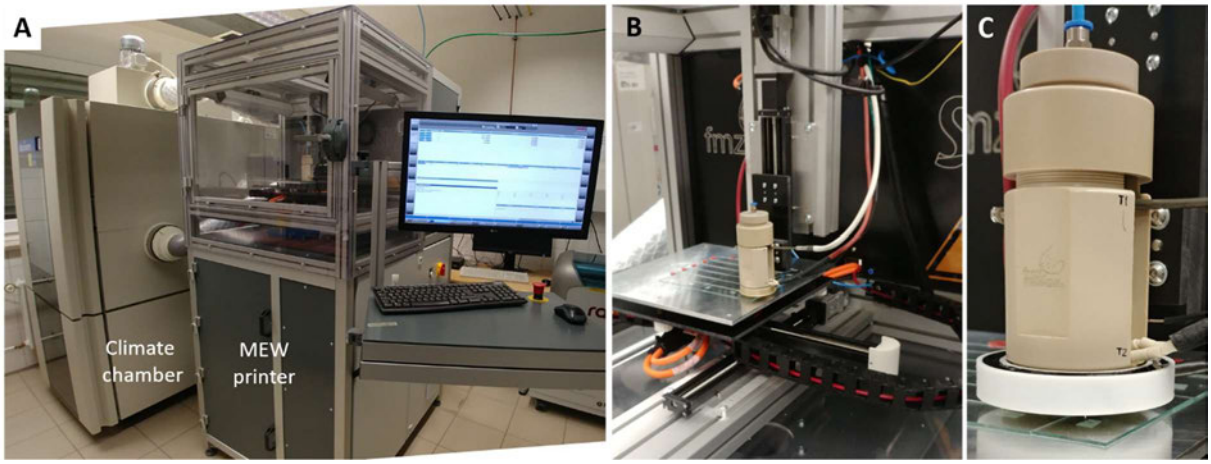

Figure 3.1. Climate-controlled MEW printer. A: General view on the MEW printer and the climate chamber. B: Printing compartment. C: Printing head with an installed discharge electrode.

The MEW printing chamber is connected to a climate control apparatus (Angelantoni Test Technologies Srl, Italy), allowing the accurate adjustment of the air temperature between 5 and 40°C and relative air humidity in the range between 20% and 80% in the whole range of the temperatures. External temperature and humidity sensors of the climate control device

(Rotronic Messgeräte GmbH, Germany) are located at the airflow inlet of the MEW printing chamber; therefore, the values indicated as the printing conditions were read from a separate portable thermo/hygrometer (TFA Dostmann GmbH & Co. KG, Germany) located inside the printing chamber. The control system allowed fluctuation of the inlet air temperature within 2°C and 5% rH respectively. All prints were collected on the 1.1 mm thick glass slides (VWR, China), which were put on an aluminium collector, connected to a voltage source. The polymer was extruded from a glass syringe (Poulten & Graf GmbH, Germany) through a 25G needle, cut to 7mm length. Full technical diagram of the heater is available in Appendix A. Scaffolds, shown in Figure 3.10 were manufactured on a different custom-made MEW printer (see Chapter 4) with a vacuum clamp for glass slides fixation of a collector (Appendix A).

Performing MEW: Three parameters, environment air temperature, air humidity and polarity of the voltage applied to the nozzle and the collector (Table 3.1), which influence on the MEW process has not been systematically studied so far, were tested in a full factorial experiment with two levels and n=3 replicas, resulting in 27 independent prints. Direct and reverse polarity stand for positive nozzle voltage and negative collector voltage and vice versa.

After initial screening experiments, both air temperature and influence of humidity were independently investigated in greater detail. Environmental parameters and stacking tests were performed under standard printing parameters #1 (Table 3.2). In the pilot stacking tests the discharge electrode was passing over the scaffold after each printing layer. Voltage alternation was done every two layers and required 5 min jet stabilization on a sham construct in between (see Chapter 4). Minimal fibre spacing and fibre stacking tests were done under the condition set #2.

Table 3.2. Parameter levels of a screening experiment. Direct and reverse polarity represent positive nozzle voltage and negative collector voltage and vice versa.

	Parameters		
Levels	Ambient temperature [°C]	Relative humidity [%]	Polarity
0	15	20	Direct
1	35	60	Reverse

CTS and MFS measurement and scaffold stacking assessment: An array of parallel lines was printed into a microscope slide with the collector speed increasing by 10 mm/min every four lines (Figure 3.2A). The lowest speed, at which all four lines were visually straight was noted as the CTS. MFS was determined by printing parallel array of fibres with a decreasing spacing (Figure 3.2B). The minimal spacing at which no fibres are stacked corresponds to the MFS for given conditions. The stacking of fibres in a scaffold was qualitatively assessed by the presence of fibres in the positions, deviating from a square grid pattern (Figure 3.2C, D).

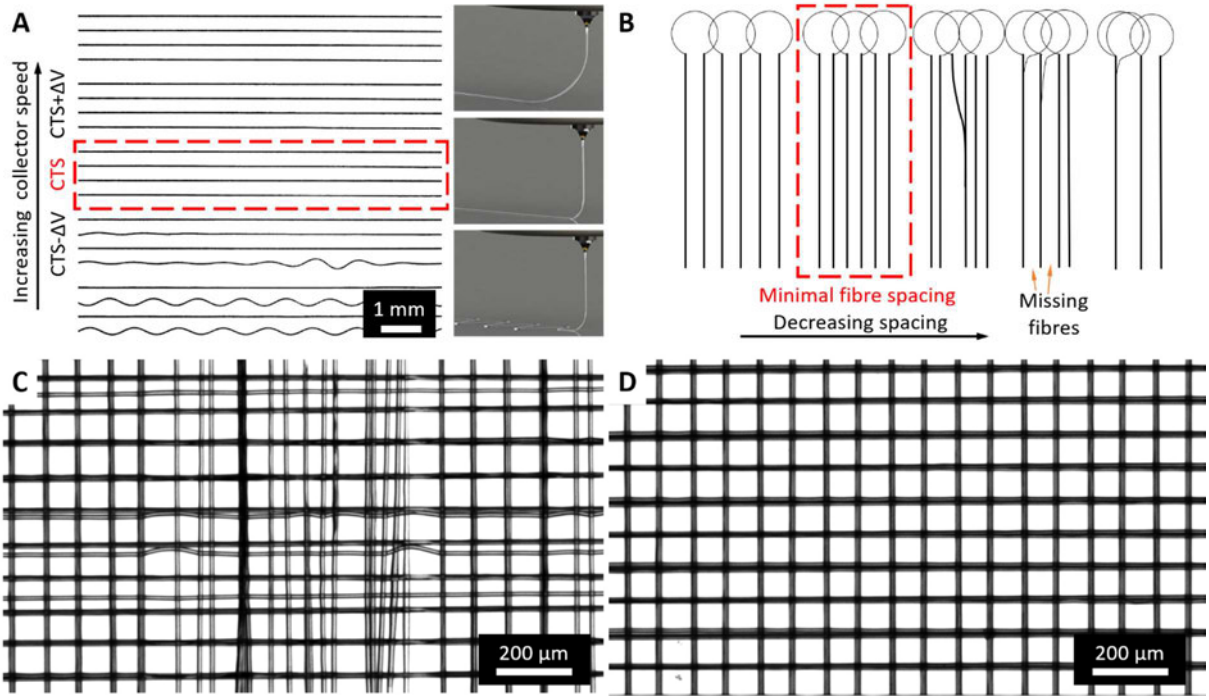

Figure 3.2. Parameter measurement schematics. A: Critical translation speed measurement, using a microscopical image of fibre arrays, printed with increasing collector speed. B: A drawing, describing minimal fibre spacing measurement. C, D: Examples of a scaffold fragment with an unsatisfactory and satisfactory stacking, respectively.

Imaging: Fibre diameter measurements and scanning electronic microscopy was done with Crossbeam 340 microscope (Carl Zeiss Microscopy GmbH, Germany). Scaffold stacking quality assessment, CTS, and MFS measurements were done with a stereomicroscope Discovery V20 (Carl Zeiss Microscopy GmbH, Germany).

Statistical analysis: For all experiments at least n=3 independent prints were made. Full factorial experiment results were analysed with three-way ANOVA using Minitab software

(Minitab Ltd. United Kingdom). For single variable experiments one-way ANOVA was applied with a Tukey post hoc test. The difference was stated as significant at $p<0.05$.

Table 3.3. Printing settings (CD – collector distance).

#	Heater temperature [°C]	CD [mm]	Collector/Nozzle Voltage [kV]	Air temp. [°C], ±2	Relative humidity [%], ±5	Collector speed [mm/min]	Pressure [bar]
1	85	2	-2/+2	20	40	1000	1
2	85	2.5	0/+4	20	40	800	0.5

3.3 Results and discussion

3.3.1 MEW printing head design

MEW printer design: A novel MEW printing head (Figure 3.1C and 3.3A) was designed and developed for this project, that comprised reduced size, cost, and customization capabilities. Technical diagrams for this printer as well as a double head printer setup (Figure 3.3B) can be found in Appendix A.

There is a number of factors that were considered for the development of this new MEW head. First, the reduced diameter of a printing head simplified the future mounting of multiple heads together. Second, the replaceable top cap together with the exchangeable heat-conductive inserts inside the coil heater make it possible to utilize syringes of different types. In addition, electrodes with various shapes (concave, etc.) can be inserted into the screwed in bottom cap e.g., for easier printing on 3D surfaces. More advanced appliances, that dynamically change the configuration of the electrical field or remove the residual charges from the surface, i.e., a discharge electrode (Figure 3.1C and Figure 3.3C, D) can also be attached. The electrical field can be either symmetrically modified by a ring electrode [156, 157] for an additional control over jet speed, or, shaped by applying a digitally controlled voltage to several electrodes (Figure 3.3D-E), thus manipulating the shape of the jet and the deposition pattern [158-160].

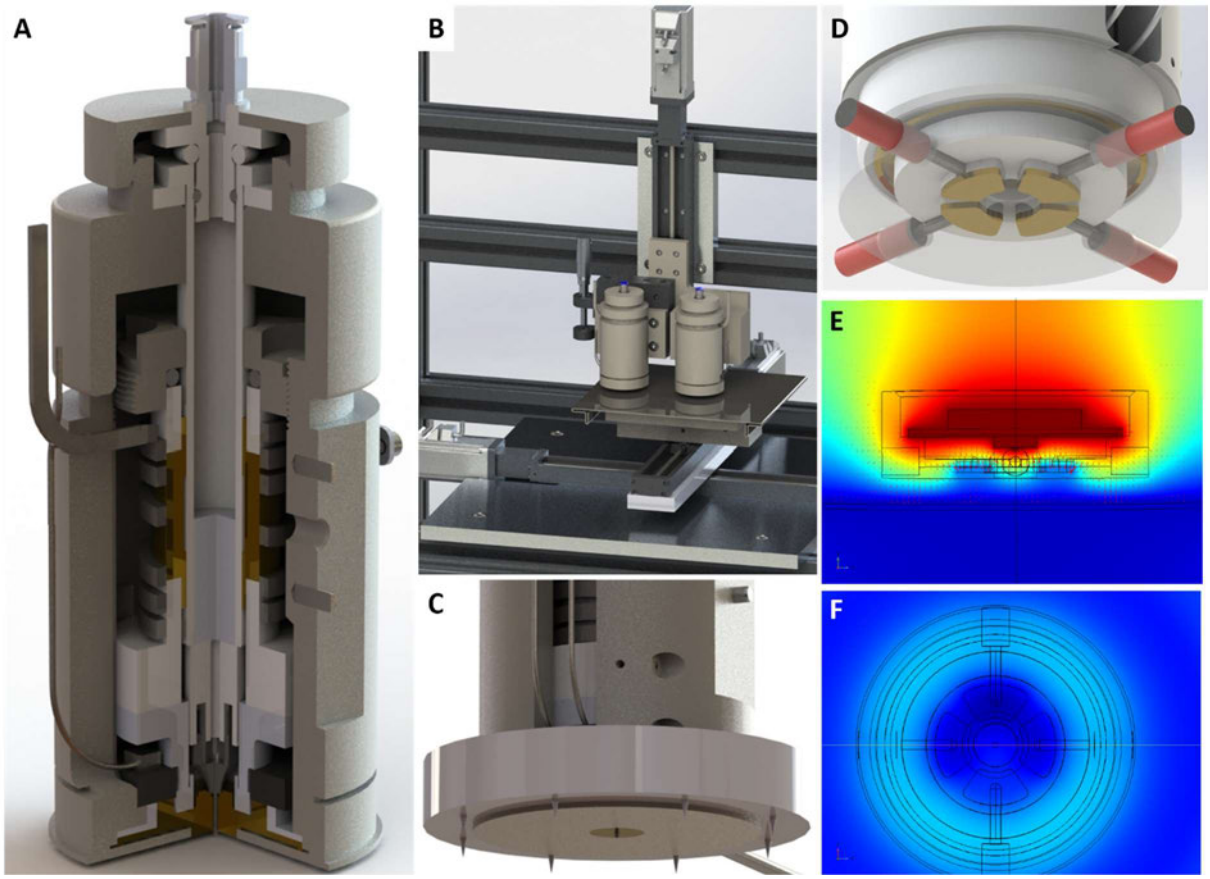

Figure 3.3. MEW head and printer design options. A: Printing head rendering with a zonal cut. B: Schematic of a double head printer setup. C: Position of discharge electrode on a printing head. D-F: Design of a headpiece (plastic body is shown semi-transparent) with four independently adjustable electrodes and a corresponding side- and bottom view of an electric field simulation.

3.3.2 CTS and diameter response to the key processing parameters

With the remodelled printing head, the typical response of the jet speed and the fibre diameter to the change in the key processing parameters was analysed and presented in the Figure 3.4.

Whereas the CTS is affected by all tested parameters, the diameter significantly changed only with pressure and polymer temperature variation. The effect of another parameter that is widely used for fibre diameter control, the collector speed, is discussed in detail in Chapter 4. The results in this Chapter generally correlate with that in literature: the greater electrostatic force leads to the higher jet speed [161] while the higher flowrate leads to the jet deceleration [72]. The increased collector distance was previously reported to decrease the jet speed due to a weaker electric field [72], contradictory to the effect, observed in this study. The difference between these results can be addressed to a much smaller range

of collector distances in the current study so that the effect of the electric field weakening is counteracted by the increased acceleration distance, causing the jet speed to increase.

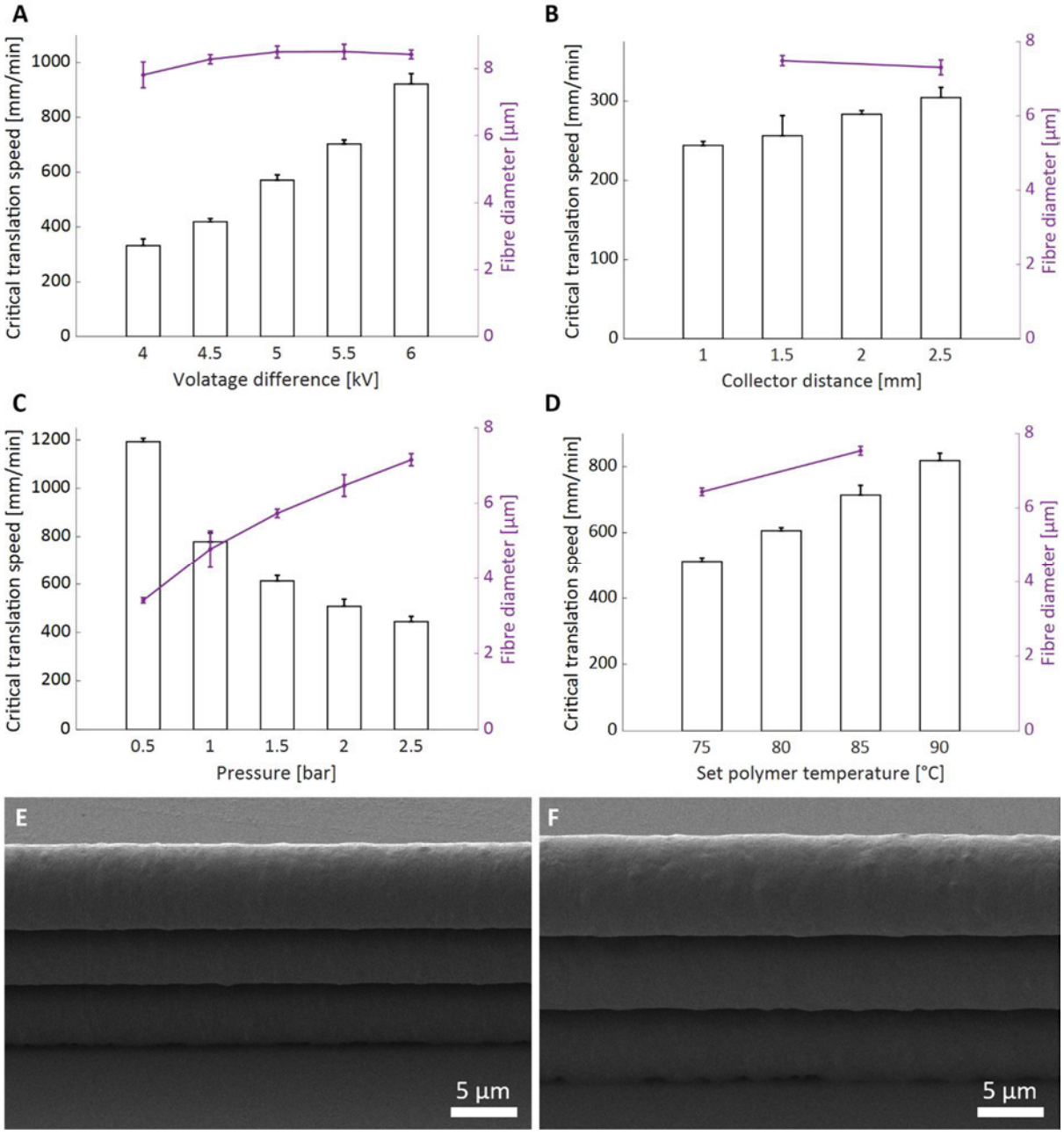

Figure 3.4. The effect of main process parameters on the CTS and the fibre diameter. A: Voltage difference between the nozzle and the collector (Positive and negative voltage of the same magnitude are applied to the nozzle and collector respectively). B, C Influence of the Collector distance and applied feed pressure, respectively. D: Influence of the polymer temperature. E, F: Tilted (45°) SEM images of three stacked fibres, printed at 75°C and 85° set temperature, respectively.

Fibre diameter was growing only through the polymer flow rate increase, caused either by the higher feed pressure or lower viscosity from higher polymer temperature. The fibre diameter growth with the higher polymer temperature (Figure 3.4E, F) needs additional analysis due to potential measurement error, caused by a change in the fibre cross-section shape (fibre flattening).

An applied voltage increase caused a rapid growth of the jet speed that was not accompanied by any significant changes in the fibre diameter and surface morphology. Since no significant flow rate change is expected due to a higher voltage (unpublished data by Mr. A. Youssef), it is possible that fibre diameter increase or decrease, demonstrated in other studies, was a result from a different degree of fibre flattening, defined by the temperature of the in the contact point with the collector. Increase in the applied voltage can cause several counteracting effects: On one hand, higher jet speed would mean that the material has less time to cool down while being transported to the collector. On the other hand, increased jet speed is accompanied by a smaller diameter and stronger effect from the electrohydrodynamic quenching from higher applied voltage [101], facilitating the jet cooling.

3.3.3 Influence of the ambient conditions and voltage polarity

The importance of the less obvious factors, such as ambient temperature, humidity and electrode polarity becomes clear from the results of the full factorial screening experiment (Table 3.4).

Quantitatively, all tested parameters had a statistically significant effect on the CTS (Figure 3.5). Fibre diameters could be measured only for specific parameter combinations when the ambient temperature was equal to 15 °C. The reason for that was the deviation of the fibre cross-section from the round shape when the fibres were visibly flattened on the collector surface or even molten together (Figure 3.6). The measurements showed no difference between the diameters of the fibres printed at various humidity and polarity levels at 15°C ambient temperature. Although the fibre diameter did not change, humid environment and direct polarity lead to a higher jet speed.

It was found that the ambient temperature strongly influences both the CTS and fibre morphology. The apparent increase in the jet temperature can reach the point when all three layers of fibres were molten together to a degree when individual fibres could not be

distinguished, and printing of stacked fibres became unattainable (Figure 3.6). This phenomenon was further aggravated at the higher relative humidity, when cylindrical fibre shape is completely lost.

Table 3.4. Environment temperature, humidity and polarity influence on CTS and fibre diameter.

#	Temperature	Humidity	Polarity	CTS [mm/min]	Fibre diameter [µm]
1	0	1	0	250	10.91±0.47
2	1	1	0	430	
3	1	0	1	250	
4	1	0	0	370	
5	1	1	1	280	
6	0	0	0	230	11.03±0.16
7	0	0	1	180	10.35±0.18
8	1	1	1	290	
9	1	0	0	350	
10	0	1	1	260	10.38±0.27
11	0	1	0	270	11.01±0.56
12	0	0	1	180	
13	1	1	1	260	
14	1	0	0	360	
15	1	1	0	410	
16	1	1	0	370	
17	0	0	0	250	
18	1	0	1	250	
19	0	0	1	160	
20	0	1	1	200	
21	0	1	0	390	
22	0	1	1	270	
23	0	0	0	230	
24	1	0	1	260	

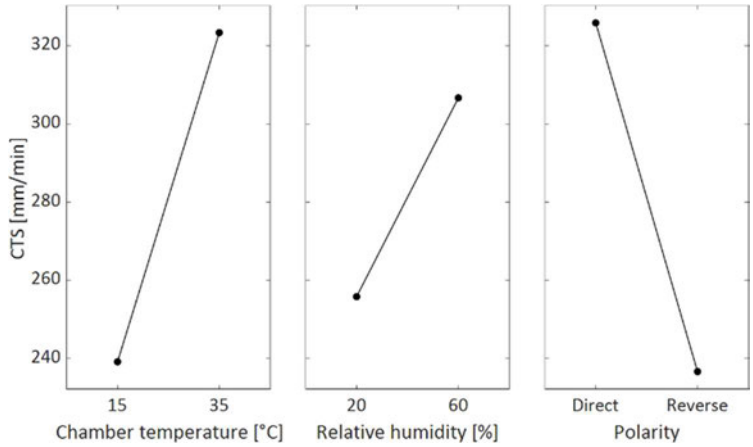

Figure 3.5. Main effects plot of the full factorial experiment, determining the influence of the ambient temperature, humidity and applied voltage polarity on the critical translation speed (CTS). Direct and reverse polarity represent the positive voltage applied to the nozzle and negative to the collector and vice versa. All parameters have significant effect on the CTS (p<0.05).

The applied voltage polarity had no distinguishable effect on the fibre shape and appearance and was limited to the jet speed influence only. The speed of the jet increased when positive voltage was applied to the spinneret, indicating either a higher charge density or lower melt viscosity. It was problematic to find exact nature of the effect though: In electrospinning, polarity effects on fibre morphology are normally addressed to the interaction of solvent molecules, charged additives or charged or highly polar groups in the polymer itself with the electrical field [162, 163]. Although the medical grade PCL does not contain any reported amounts of additives, the presence of the residual amounts of catalysts or solvents from the production process cannot be excluded.

Further experiments with smaller parameter increments indicated that the CTS was growing gradually but significantly with the increase in humidity and temperature (Figure 3.7). While changing the air temperature from 15 to 30°C with 2.5°C step it was possible to identify the onset of the critical fibre fusion and the morphology change. Starting from 25°C, the bottom fibre cross-section was losing the elliptical shape and starts wetting the collector surface. At 27.5 and 30°C higher layers also became affected.

The air humidity effect on the CTS, measured at 20°C air temperature, was weaker than the one from the temperature increase. Nevertheless, already at 20°C temperature, printing at an increased humidity (80%) caused the bottom layer fibres to spread stronger on the

collector surface. With higher air temperature, stronger fibre flattening and complete fibre fusion of the orthogonally printed fibres in the intersection point were added (Figure 3.8).

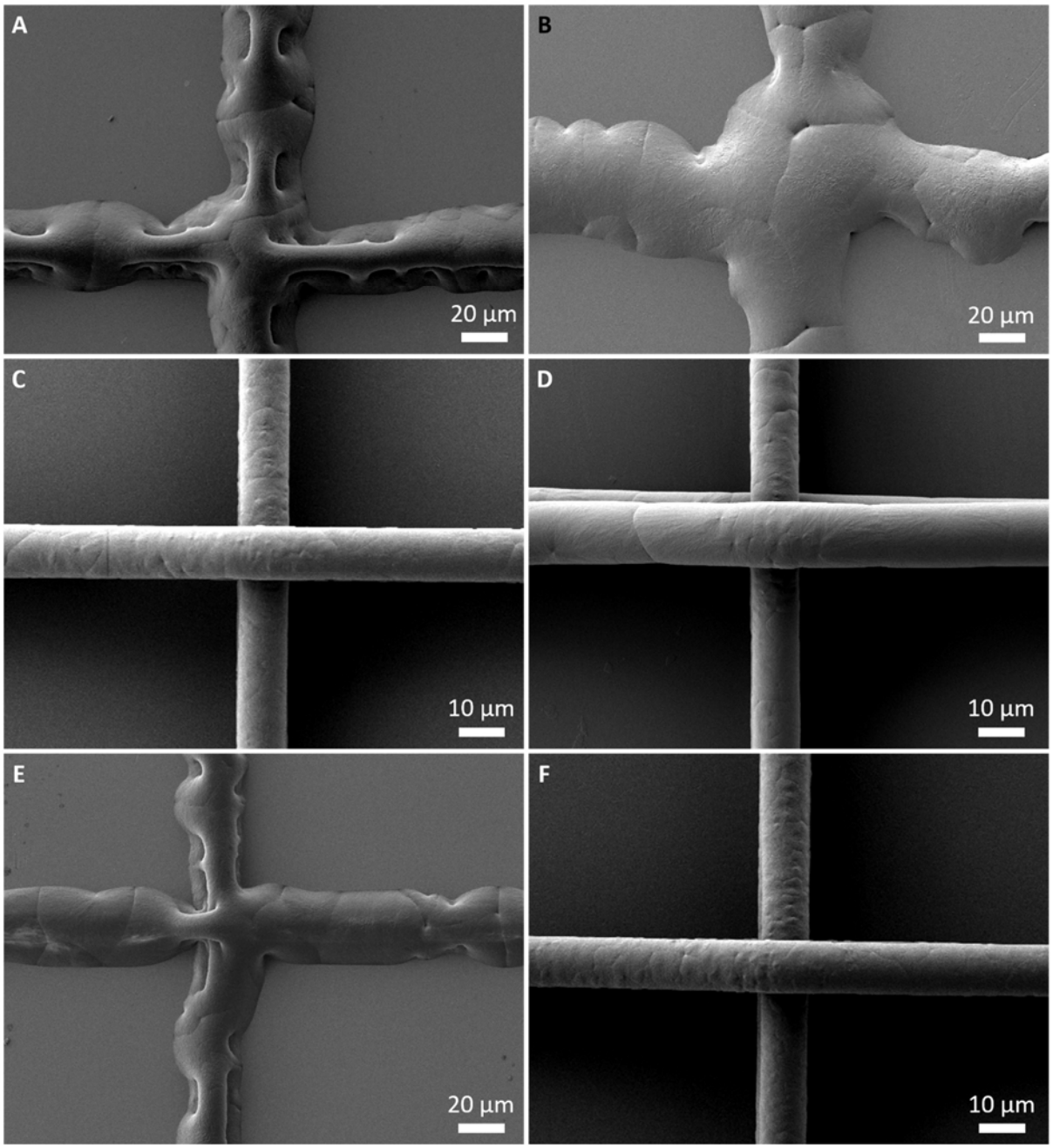

Figure 3.6. SEM images of the fibre intersection points (three fibres in each direction) for different conditions from the screening full factorial experiment (Table 3.4). A: Run 4. B: Run 2. C: Run 6. D: Run 1. E: Run18. F: Run 22.

The diameter variation between the samples, produced under the same conditions in the different experiments can be addressed to the material degradation in the heater and polymer temperature fluctuations of the heating system.

Although ambient temperature and humidity mainly affect the jet speed and do not have significant influence on the fibre diameter (Figure 3.7), their ability to change the fibre morphology, to a point when the material, landing on the collector, is too molten to keep cylindrical fibre shape, creates limitations to the MEW printing process. Thus, a set of temperature-humidity combinations exists, beyond which individual fibre printing becomes impossible. Those limiting values can be shifted by an adjustment of the polymer temperature. Another parameter, that might influence the jet temperature in the point of contact with the collector is the collector distance. A larger collector distance makes the jet longer, increasing the cooling time and weaken the heating of the collector by the heater.

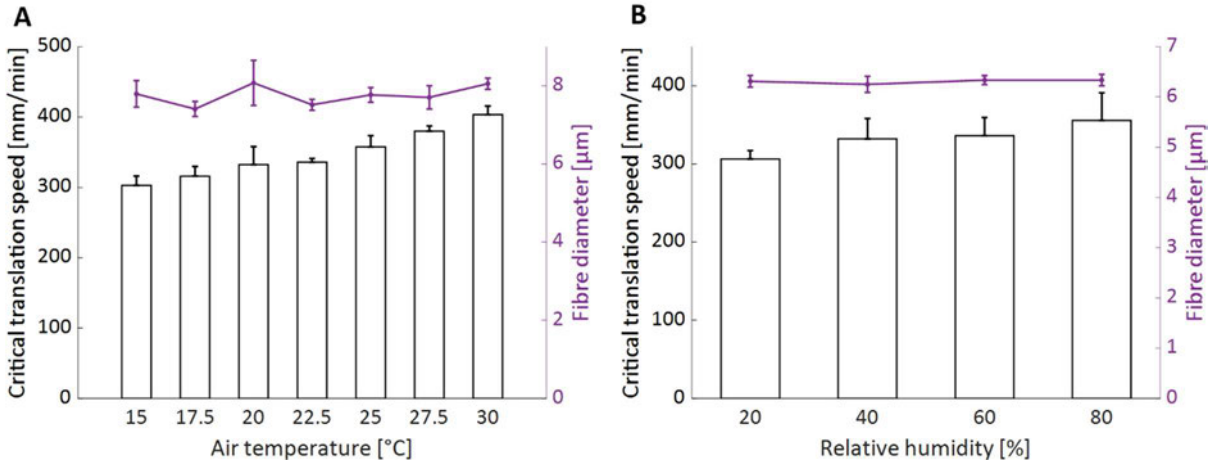

Figure 3.7. Critical translation speed and fibre diameter measurement. A: Ambient temperature variation. B: Relative humidity variation.

The effect of increased fibre fusion at a higher temperature and humidity can have a positive effect on the mechanical properties of the scaffold (see Chapter 7). In addition, increased jet speed allows shorter printing time when the print predictability is improved by printing at a speed close to the CTS (Chapter 6). A higher CTS can be readily obtained by applying higher voltage, which is limited only by the electrical breakdown threshold value (i.e., electrical discharge).

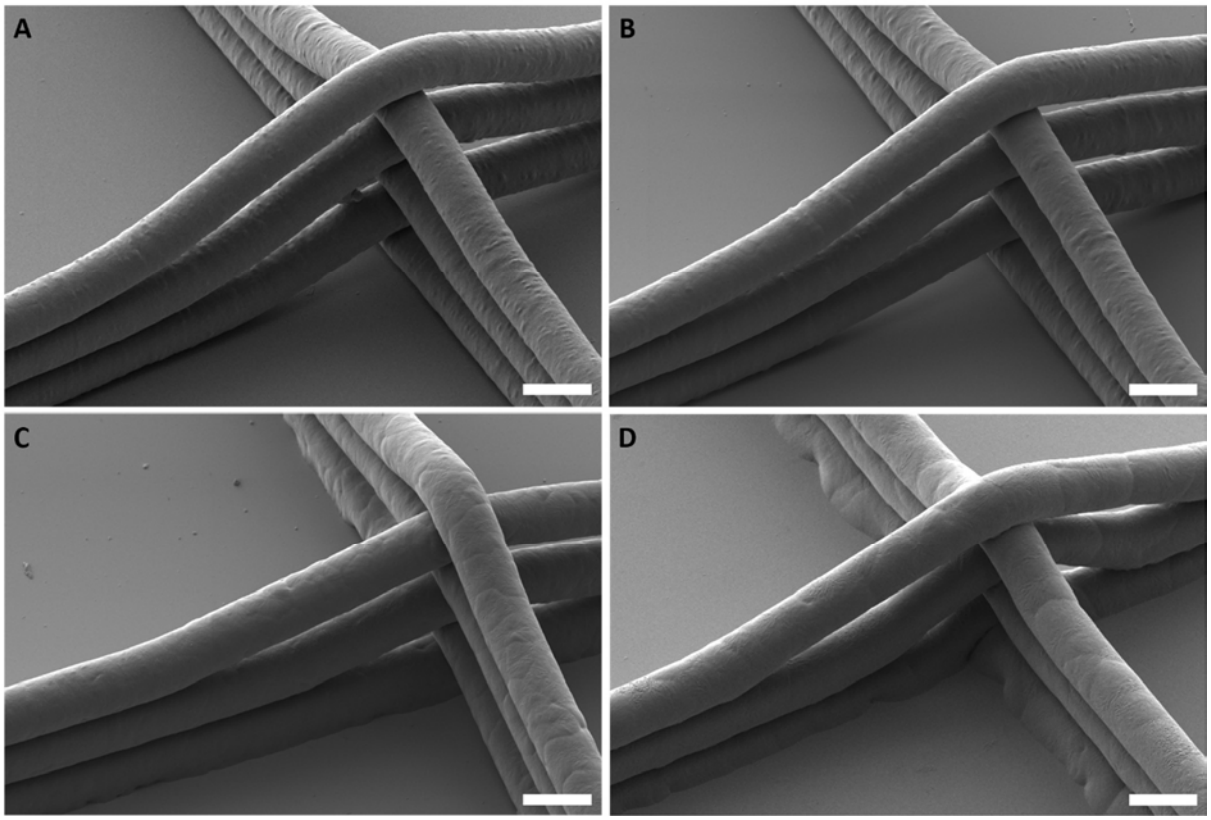

Figure 3.8. Ambient temperature influence of the stacked fibres morphology. A: Air temperature 15°C. B: 20°C. C: 25°C. D: 30°C. Air humidity was kept at 40%rH. All scale bars 10 µm.

3.3.4 Minimal fibre spacing

Although the diameter of the fibres can influence the minimal fibre spacing (MFS), at which parallel MEW fibres can be deposited next to each other without stacking (unpublished data by Ms. J. Kim), fibre diameter in a scaffold is often predefined by the required mechanical properties, degradation speed of immunological properties of the whole scaffold. When the diameter has to be kept constant, the only parameters that can be readily and independently varied and don't affect the fibre diameter are parameters that are related to the electrical field strength, applied voltage and collector distance. The general outcome (Figure 3.10) does correspond to the observed trend from the literature, reviewed in the introduction to this Chapter, where combinations of smaller collector distance and applied voltage allowed the printing of scaffolds with smaller pores; however, no individual parameter influence has been detected.

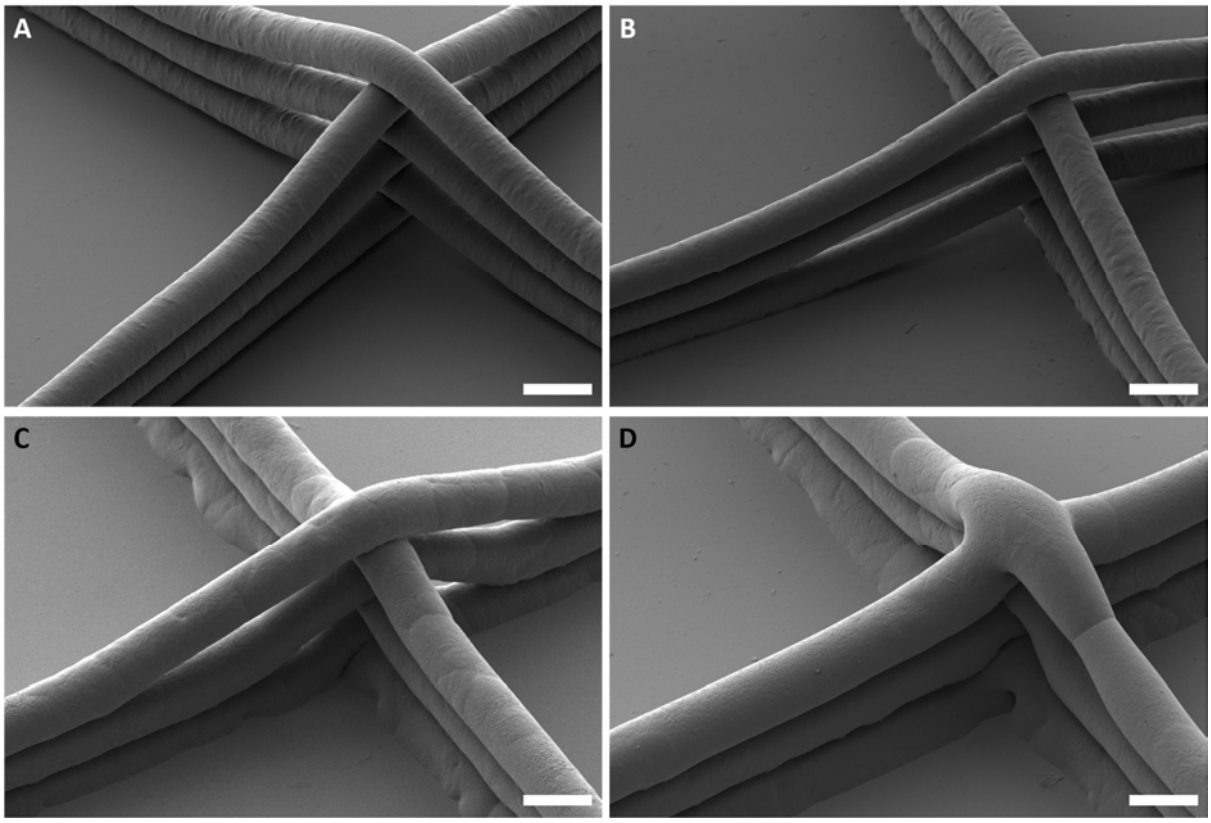

Figure 3.9. Environment air relative humidity influence of the stacked fibres morphology at 20°C (A, B) and 30°C (C, D) temperature levels. A: 20% rH. B: 80% rH. C:40% rH. D: 80% rH. All scale bars 10 µm.

No significant difference between the MFS values for different for polarity configurations and voltage magnitude was found (Figure 3.10A-C). Voltage, as well as a simultaneous voltage and collector distance change, significantly affected the MFS, however no clear trend was found (Figure 3.10D-E and G-I respectively). Additional complexity is brought by the fact that at different parameters the jet lag is also different, affecting the fibre placement when the same collector speed is applied (see Chapter 6 for detailed explanation of the relationship between the jet lag, CTS and printing accuracy). This effect is mostly visible at the ends of the linear movement segments and circular transition paths between them. Several conclusions can be made from the presented results though. First, the changed loop shape of a sample, printed with the reverse polarity indirectly confirms the results of the screening test that the CTS decreases, thus increasing the lag at the same collector speed and therefore making the loop shape less round.

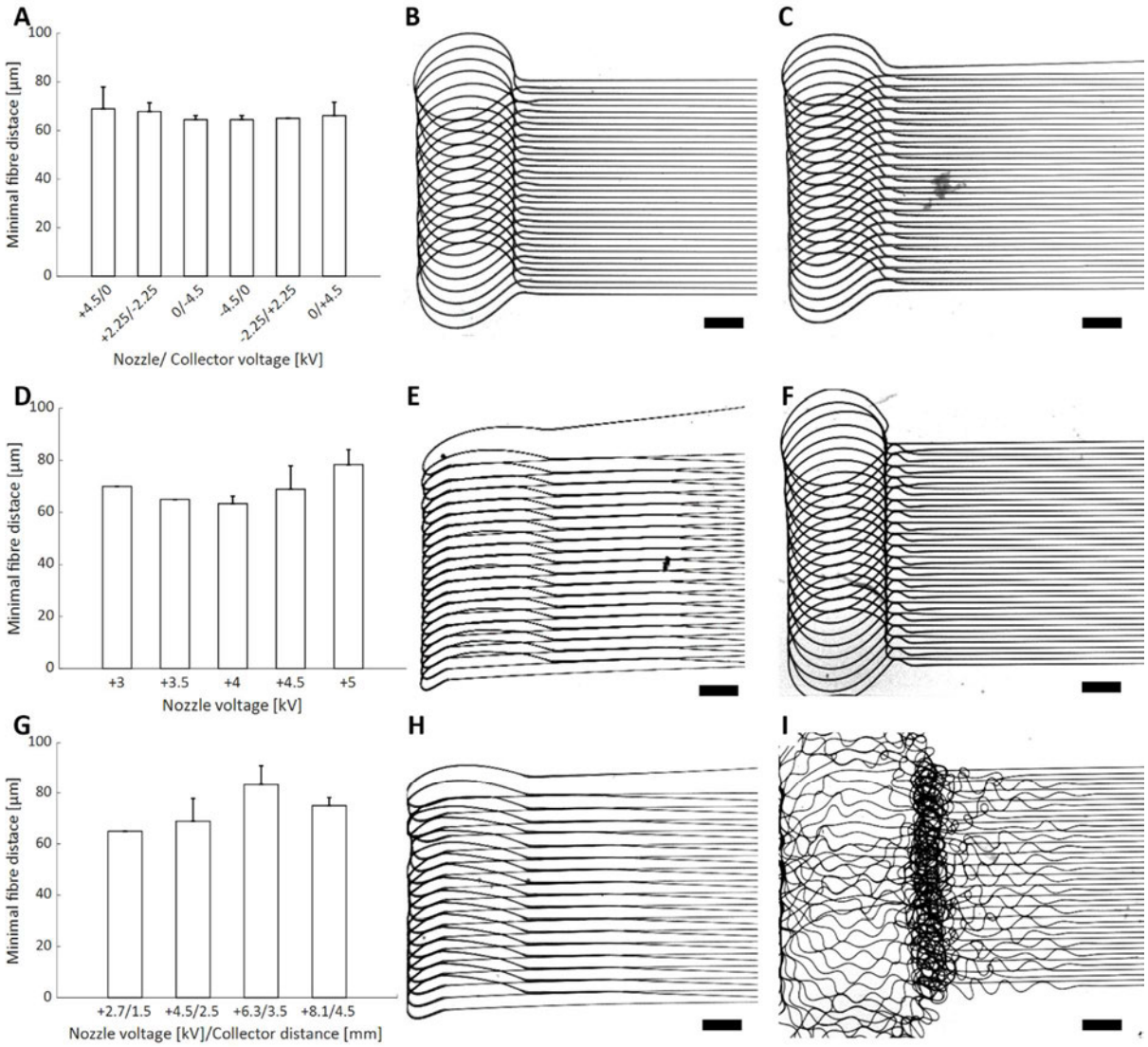

Figure 3.10. Influence of the voltage and the collector distance on the minimal fibre spacing. A: Nozzle and collector polarity influence. B, C: Microscopic images of the edge of the fibre array when the positive 4.5 kV is applied to the nozzle and the collector, respectively. D: Nozzle voltage magnitude influence. E, F: Images of the edge of the fibre array at the minimal and maximal tested voltage, respectively. G: Simultaneous voltage and collector distance influence. H, I: Images of the edge of the fibre array at the minimal and maximal tested voltage and collector distance combination, respectively. All scalebars 500µm.

With a lower voltage and shorter collector distance, the difference in the jet lag is causing a considerable deformation of the printed path near the edge of the array (Figure 3.10E and H). Despite the maintained programmed fibre spacing in the middle of the array, in a scaffold, build of stacked and intersecting arrays with such fibre deposition a large share of

a scaffold area will not have a desired pore size. It means that scaffold printing under these conditions is not efficient. Reduction of this effect can be achieved by using a lower collector speed [52] or introduction of pauses at the ends of the line segments, which however, increases the printing time. Thus, higher voltage and direct polarity allows printing of the same pore size scaffolds at faster collector speeds.

The applied voltage is usually limited by the breakdown voltage of the air gap between the nozzle and the collector. In case of a non-conductive collector, such a glass plate, the breakdown voltage can go up to dozens of kV, allowing printing at faster collector speeds without the accuracy loss. Further increase of the collector speed can be achieved by increasing the collector distance, temperature and applying direct polarity. With the increased collector speed, more attention has to be paid to the programming of the collector path in order to avoid the points (e.g., sharp corners), where the collector speed inevitably falls due to a limited axes acceleration. Once the collector speed in the vicinity of those points keeps lower that the CTS for enough time, the jet starts to buckle, leading to a coiled fibre accumulation (Figure 3.10I).

Further decrease in MFS and consequent scaffold pore size can be achieved by a further decrease of collector distance and voltage as well as alternative scaffolds designs. Smaller pores sizes can be achieved in stacked fibre layers by printing non-linear patterns [61], as a result of fibre crossing at different angles (Chapter 4, Ref. [114]) or using the effect of fibre suspension (see Chapter 7). With the suspended fibre approach inter fibre distances of 20 µm could be achieved but the architecture limitation as well as manufacturing challenges are hampering a wider usage of dense suspended fibre arrays in the MEW scaffolds.

3.3.5 Stacking behaviour observations

The most important factor influencing scaffold fidelity is the fibre spacing. For scaffolds printed at minimal fibre spacing (60µm) misplaced fibres could be observed starting at four stacked layers, while scaffolds with 140 µm fibre spacing could be printed up to 12 layers thick before the first defects start to appear. The mechanism behind the incorrect positioning of the fibres for scaffolds with the small thickness may differ from the mechanism described by the study of Wunner et. al. [60], where several stacking defect types are discussed. It should be considered that at a high density of the fibres, the attraction of the fibre directly

underneath the desired location is comparable to the attraction of the adjacent fibre in the layer that is currently being printed. It is possible that a combined effect of the mechanical stretching and electrostatic attraction induces the change of the fibre path from the initial misplaced position to the programmed location or vice versa in the middle of a scaffold (Figure 3.11 A, B)), thus changing the visible pore size in the scaffold.

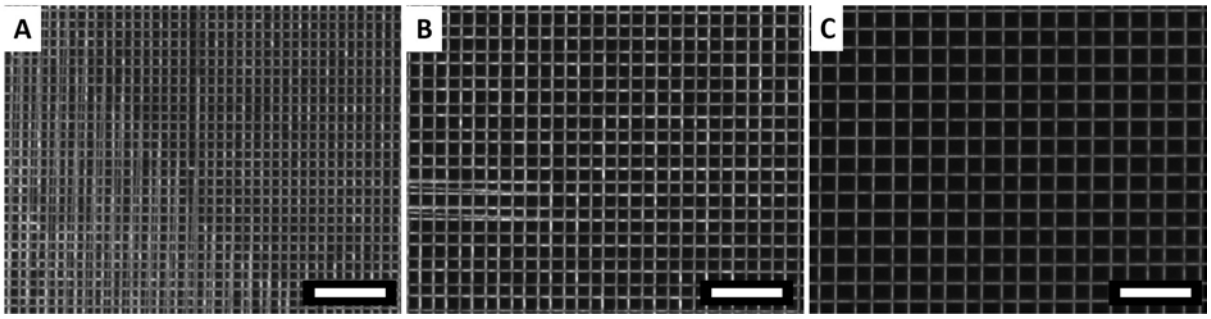

Figure 3.11. Stereomicroscope image of MEW scaffolds with eight stacked layers in each both orthogonal directions and a varying fibre spacing. A: 60 µm. B: 100 µm. C: 140 µm. All scale bars 500 µm.

If the fibre misplacement were caused by a slower rate of charge elimination from the upper layers in the scaffold, it is more likely that the fibres would take a random position rather than attach to a different fibre. Furthermore, in the experiments, where an attempt was made to improve the fidelity of the scaffolds by removing the accumulated charges from the uppers scaffold layers with a discharge electrode or negating their influence by changing the applied voltage polarity every two printed layers (Figure 3.12), no improvement could be registered. As a side effect, the printing time was increased due to the necessity of additional collector movements and jet stabilization for the discharge electrode and polarity change, making those approaches undesirable, at least for small (below 20 layers) scaffold thicknesses. This observation, however, neither negates the existence of the charge accumulation mechanism nor discredits the presented charge elimination methods for MEW as it is necessary to investigate their applicability on thicker scaffolds or other polymers with different electric properties. The experiments performed here only work within fibres made of Corbion PC12 PCL and stacked up to maximal 20 layers. The effects of the previously deposited structures on the newly direct written fibre shape and position are further described in Chapters 5 and 6. According to the results presented in these Chapters, fidelity improvement can be brought by a lower collector speed or printing path adjustment.

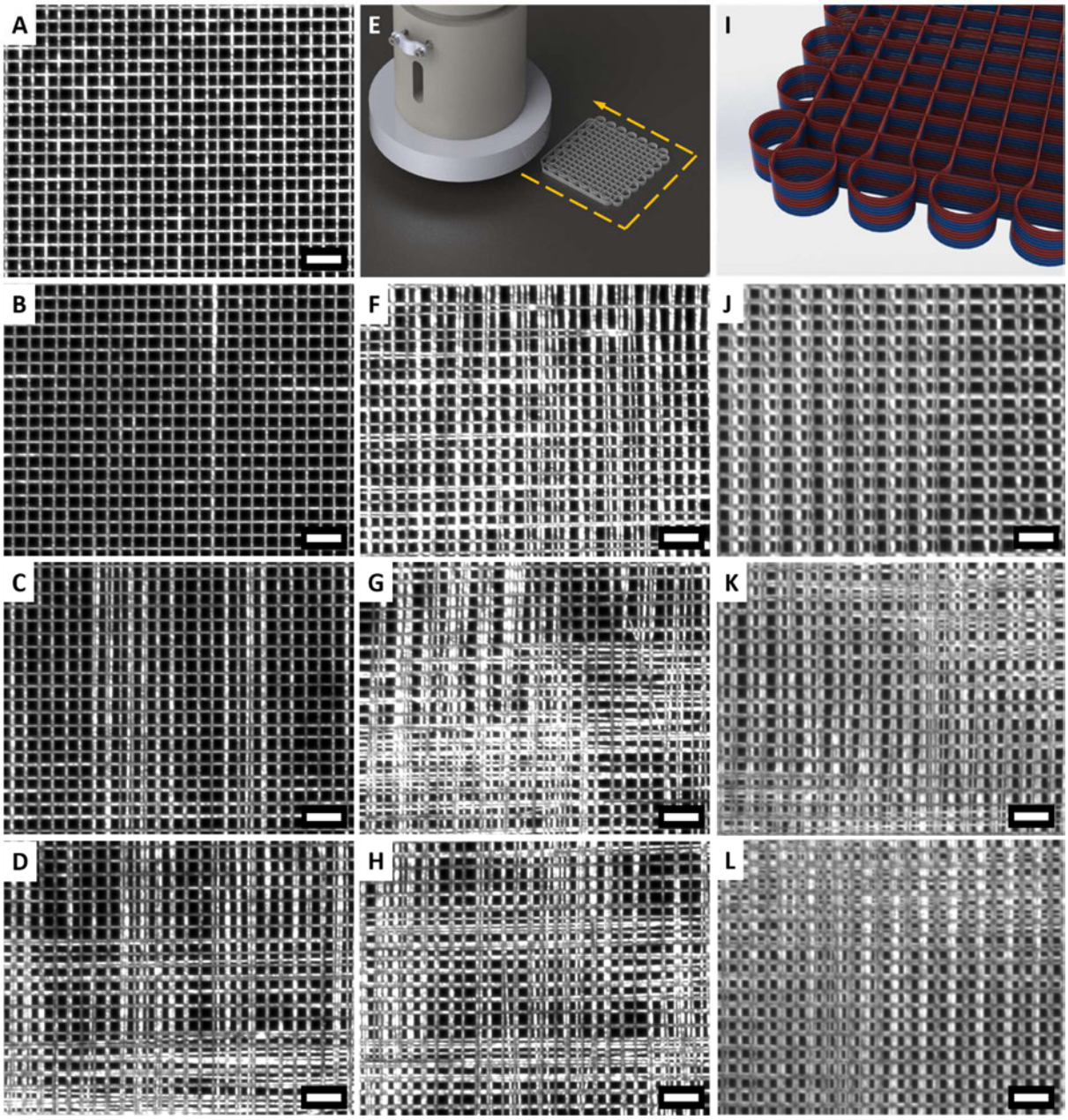

Figure 3.12. Investigation of fibre stacking improvement techniques. A: Microscope image of a single layer of orthogonal fibre arrays with 80 µm fibre spacing. B-D: Scaffolds with 4, 10 and 16 layers, respectively. E: Scheme of a relative head movement with the activated discharge electrode. F- H, J-L: Scaffolds with 4, 10 and 16 layers printed with discharge electrode treatment after each layer. I: Schematic principle of a scaffold, printed with polarity change (layers in blue and red are printed with direct and reverse polarity respectively). All scalebars 250 µm.

Chapter 4: Diameter variation and multimodal scaffolds

4.1 Introduction

Additive manufacturing principles have been applied to the fabrication of 3D scaffolds for TE [36, 164, 165], including for bone [166], cartilage [167] and skin [168] regeneration. additive manufacturing can provide not only implant shape freedom, indispensable for the personalized medicine but also allow to incorporate different materials, micro and nanostructures within one implant or construct [169, 170]. Scaffolds that are comprised of distinct regions are termed multiphasic [171], while differing dimensions within a morphology is termed multimodal [169, 172]. One TE paradigm argues that the complexity of tissues and organs requires multimodal and multiphasic structuring for scaffolds [55, 173]. With this approach interfacial areas within a tissue with a zonal organization or between different tissues can be reconstructed [50].

Within one scaffold microstructure there is a way to expand its biological properties by the addition of features with different sizes. Multimodal [174, 175] scaffolds allow better cell adhesion and guidance with smaller fibres while larger ones maintain the scaffold mechanical properties, necessary for handling, implantation and integration. One of the simplest and widespread approaches to incorporate small diameter fibres (down to nanometre size) is solution electrospinning. Larger feature sizes have been provided using melt plotting [176, 177], melt spinning [178] or a different electrospinning configuration [174]. Furthermore, structures with small features have been direct-written with strongly shear-thinning fluids such as colloidal inks and hydrogel precursors [179, 180]. In contrast to the above-mentioned methods, MEW, can produce a broad range of fibre diameters within one print in a single setup. Additionally the stability of the fibre diameter is considered as one of the benefits of MEW [181]. Furthermore, the ability to combine fibres with different diameters is attractive for many TE applications and greatly expands the design perspective for TE scaffold.

4.2 Materials and methods

MEW printer, materials, and processing parameters: All scaffolds were fabricated from a medical-grade poly(ε-caprolactone) (PCL) (Corbion Inc, Netherlands, PURASORB PC 12, Lot# 1412000249, 03/2015), used as received. The storage and handling of the polymer is described elsewhere [182]. A custom-built printer [182] was used for all MEW printing experiments (Figure 4.1A). The polymer melt, heated up to 73±1°C, was extruded by pressurized air through

a 12.5 mm long, 22G stainless steel nozzle (Nordson Deutschland GmbH, Germany) and deposited on a stainless-steel collector. Positive 7kV voltage was applied to the nozzle, whereas the collector had a negative 1.5 kV potential. The collector distance, defined as the gap between the nozzle tip and the collector surface, was set to 6 mm while the nozzle itself protruded by 0.5 mm out of the brass electrode. The environmental conditions during the experiments were an ambient temperature of 21±2°C and a relative humidity of 40±10 %.

Direct writing of fibres: The CTS of the jet was measured for the 0.5, 2.0 and 4.0 bar pressures as described in Chapter 3. The fibre diameter measurements were conducted after 15 min stabilization for all combinations of the three abovementioned pressures and five collector speed values (100, respective CTS, 1000, 3000 and 10,000 mm/min). The diameter measurement scheme is shown in Figure 4.1B. Additional diameter measurements with an increased number of factor levels were done for validation of a proposed mathematical model. The speed effect was investigated at a constant pressure of 2 bar in the range between 1×CTS (430 mm/min) and 13×CTS (5640 mm/min) with 2×CTS steps, whereas the pressure was varied from 0.5 and 4.0 bar with 0.5 bar steps with the collector speed fixed at 1000 mm/min.

To evaluate how the fibre diameter changes during jet stabilization, six pressure transitions between 0.5, 2.0 and 4.0 bar air were tested. The measurement schematic is shown in Figure 4.1C. Every 20 s the pressure was changed, and a 2 mm long straight fibre was printed at 1.15×CTS, corresponding to the current pressure. In the middle of those segments the fibre diameter was measured and meanwhile an off-sample printing of a sham construct was done (Figure 4.1D). The collector speed during the sham constant printing was set to 4×CTS and 1.15×CTS to determine the influence of the collector speed during stabilization on the time, required for jet stabilization. For one pressure pair (0.5 to 4 bar transition) the measurements were performed at a higher sampling frequency (every 2 s) to reveal the presence of diameter oscillations with higher frequencies. A further experiment, demonstrating the speed of diameter change after stage acceleration and deceleration was performed under the following printing conditions: 75°C set polymer temperature, 1.2 bar air pressure, 3.5 mm collector distance, -1.5 kV collector voltage and +5.75 kV nozzle voltage. Fibres were collected on 1.1 mm thick glass slides (VWR Inc., China). The stage accelerated and decelerated between stationary and 1150 mm/min (5×CTS) or 460 mm/min (2×CTS).

Multiphasic scaffolds printing: For the scaffold printing the parameters had to be changed to obtain the required inter-fibre spacing. For that the collector distance was reduced to 3 mm, while decreasing the nozzle voltage to +3.1 kV. Multiphasic scaffolds, with different pore shapes on the different layers were printed at a constant pressure of 1 bar and the fibre diameter in the suspended membrane (marked green, Figure 4.1E) was achiever by increasing the collector speed from 500 to 6000 mm/min. Incorporation of suspended fibres into the scaffold is described in greater detail in Chapter 7. Scaffolds with varying size of square pore and fibre diameter were manufactured with the applied pressure set to 0.3, 0.2 and 1 bar for scaffolds 1-3 respectively (Figure 4.6). G-codes for the MEW printing of the scaffolds, demonstrated in Figures 4.5-4.8 are provided in Appendix B.

Visualization of fibres and statistical analysis: CTS measurements and a three-layer scaffold image were made with a stereomicroscope (Discovery V20, Carl Zeiss Microscopy GmbH, Germany). Fibre diameter measurements and scaffold imaging were performed with a SEM (Crossbeam 340, Carl Zeiss Microscopy GmbH, Germany). Prior to the SEM imaging all samples were sputter-coated (EM ACE600, Leica Microsystems, Germany) with 2 nm of platinum. Part of the SEM imaging (Figure 4.2D-F) was performed by Ms. J.N. Haigh. All results are displayed as mean ± standard deviation; n=9 samples were used for all measurements except for the high sampling rate diameter measurements and diameter change during acceleration/deceleration (n=5). A t-test was performed to determine statistical significance of the results (p=0.05). All cell culture experiments were done with n=3 samples per scaffold type and imaging timepoint.

In Vitro culture and analytics: L929 murine fibroblasts were seeded onto the scaffolds, preliminary sterilized for 30 min in 70% ethanol and etched for 1 h in 2M NaOH solution at 37°C. After washing the scaffolds three times in phosphate buffer saline (PBS) a droplet of medium with 1×10^5 cells was applied on each scaffold from the side with square pores and positioned in a 'sandwich' [57] between two polystyrene rings, keeping the scaffold from touching the well bottom of a 12-well plate (Nunc, Germany) and preventing it from floating (Figure 4.1F). The scaffolds were cultured in the Dulbecco's modified eagle medium (DMEM) (Gibco, Germany) with 10% foetal calf serum (FCS) (Gibco, Germany) and 1% penicillin/streptomycin (Gibco, Germany) up to 21 days.

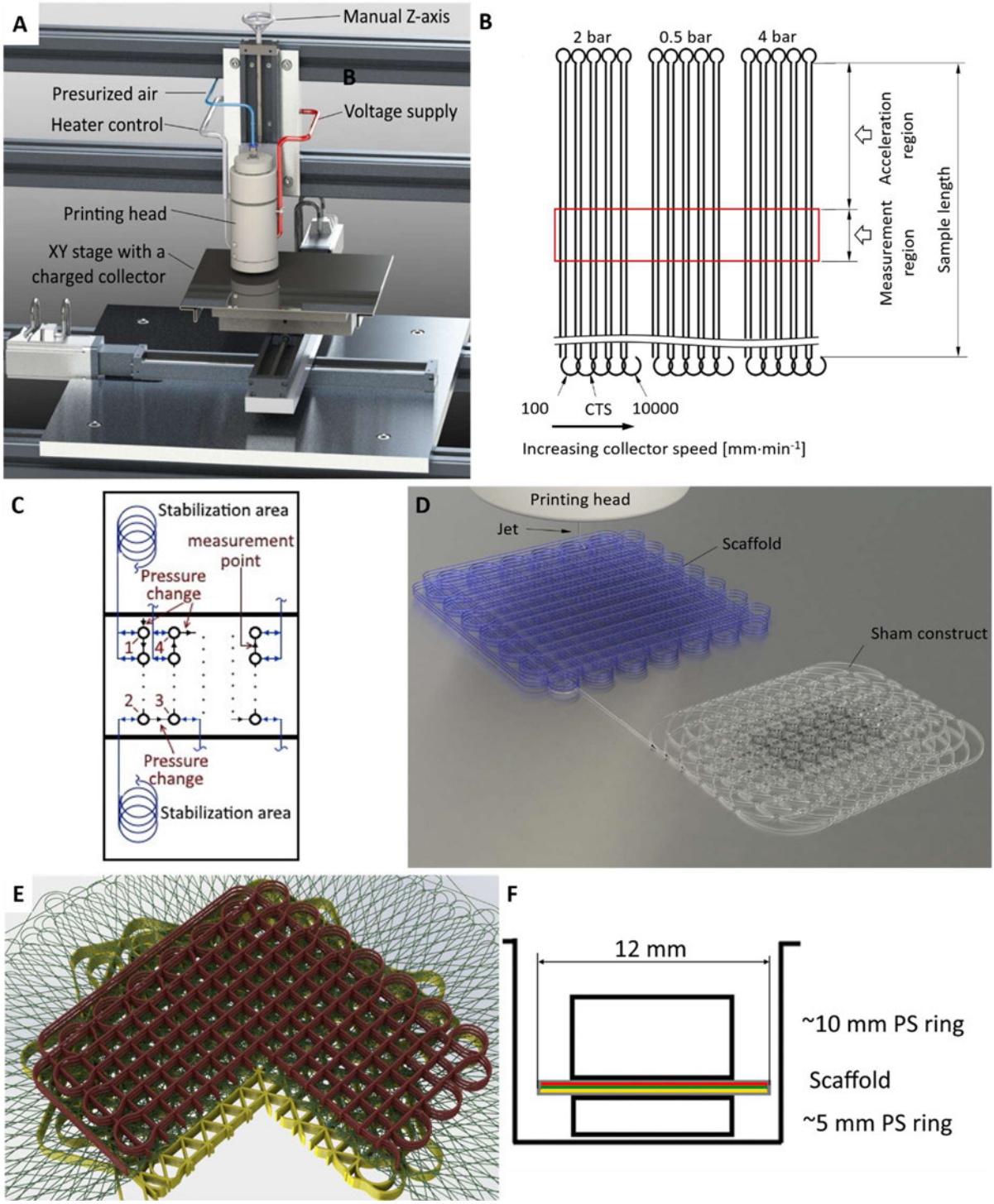

Figure 4.1. A: Schematic of a MEW printer. B, C: Schematics of the fibre diameter measurements of a stabilized jet and during stabilization, respectively. D Rendered scheme of a MEW printing procedure, when a scaffold is printed after jet stabilization, occurring during a sham construct printing. E, F: A schematic rendering of a multiphasic scaffolds combined of scaffolds with square (red), pseudo random (green) and triangular (yellow) pores and the scheme of scaffold positioning in a cell culture well between two polystyrene (PS) rings. A, C and D: Copyright Wiley. Figures adapted from Ref. [140].

Human mesenchymal stromal cells (hMSCs) were obtained from a patient undergoing total hip replacement surgery. Cells were expanded and 1.5×10^5 hMSCs in passage 4 were seeded on top of three-layer multiphasic scaffolds with the dimensions of 12×12 mm. The constructs were cultured for up to 21 days in DMEM/F12 GlutaMAX medium, described above with 50 mg/ml ascorbic acid (Sigma-Aldrich, Germany). The medium was changed twice per week.

Cells on scaffolds were sputter coated with platinum and visualized using SEM. Prior to the SEM imaging the scaffolds with the cells were washed thrice in PBS and fixated with 6% glutaraldehyde (Sigma-Aldrich, Germany) for 15 min. After fixation, the samples were washed thrice with PBS and dehydrated by applying ethanol solutions in water with concentrations of 50, 70, 90, and 100% twice, each for 10 min. Dehydrated scaffolds were treated by hexamethyldisilazane (Sigma-Aldrich, Germany) for 15 min and left to dry overnight. MSCs and L929 cell culture was assisted and supervised by Mr. A. Youssef and Dr. C. Blum. All human adipose stem cell (hASC) spheroids related cell culture experiments were performed by Ms. R. McMaster and Dr. C. Blum. For details, please see the corresponding publications [140, 183].

4.3 Results and discussion

While maintaining the applied voltage, collector distance and temperature, fibres with diameters from 2.0±0.6 µm to 49.9±2.6 µm (Table 4.1, Figure 4.2A) were printed in a single run using only changes in the applied air pressure and collector speed. Notably, these diameters were achieved and incorporated into a single construct, using the single 22G nozzle. The highest air pressure and the slowest collector speed led to the formation of fibres with large fibre diameters, approaching the lowest attainable fibre size of the extrusion polymer melt printing [184]. For the manufacturing of smaller diameter fibres, decreased air pressure and faster collector speed was applied, respectively.

The effect of the collector speed and pressure on the fibre diameter can be used for a controlled diameter adjustment during printing, using the following equations:

$$D_2 = D_1 \cdot \sqrt{\frac{P_2}{P_1}} \qquad (4.1) \text{ and } D_2 = D_1 \cdot \sqrt{\frac{V_1}{V_2}}, \qquad (4.2)$$

where D_2 is the predicted diameter after the parameters change, while D_1 is the known diameter under the initial pressure and speed, P_1, V_1. P_2 and V_2 are the new pressure and

speed values. It is convenient to substitute the D_1 with the fibre diameter at CTS and use CTS for V_1. (Table 4.1, Figure 4.2B, C), while the fibre diameter prediction is only valid above the CTS. Although these equations are strictly correct for a non-compressible fluid only, their predictions were sufficiently accurate (error less than 10%), at least within the tested parameter ranges. Fibres of different diameters produced with various pressure/collector speed combinations can be used to create various patterns and be stacked upon each other (Figure 4.2D-F).

When the collector speed is lower than the CTS, a fibre is deposited as a periodic curved pattern, [47, 182, 185]. This behaviour was previously described for free falling viscous liquids [71, 186] and elastic rods [187] without the applied electrical field. The fibre diameter of the coiling segments does not change significantly in the range from 100 mm/min to CTS (Figure 4.2A).

Table 4.1. Critical translation speed (CTS) and fibre diameter ranges, obtained at different feed air pressure values

		Collector speed			
		CTS		10000 mm/min	
Air Pressure, [bar]	CTS, [mm/min]	Fibre Diameter, [µm]	Coefficient of Variation, [%]	Fibre Diameter, [µm]	Coefficient of Variation, [%]
0.5	750±20	11.03±0.43	3.9	2.02±0.57	28.1
2.0	420±22	29.02±2.53	8.7	4.29±0.54	12.6
4.0	300±7	47.38±1.33	2.8	6.77±0.93	13.7

Diameter control with air pressure: At a constant collector speed of 1000 mm min^{-1}, a three-fold diameter increase was observed when the pressure changed from 0.5 to 4 bar. Expansion of the stable diameter range under the set process parameters (i.e. fixed voltage, nozzle gauge and collector distance) was not possible: in both cases, below 0.5 bar and 4 bar fibre pulsing [182] occurred. The diameter range can be shifted together with the pressure window by choosing a different parameter combination: e.g. at higher voltages higher pressure values can result in a stable jet [182]. Using the Equation 4.1, P_1 =0.5 bar and separately measured D_1 = 8.94 mm value, a formula $D = 8.94 \cdot \sqrt{P/0.5}$ adequately predicted (R^2=0.990) the experimental data (Figure 4.2B).

The transition between different diameters, characteristic for certain pressure values requires a stabilization period, during which the diameter tends to undergo damped oscillations. Stabilization time is defined here as a period when oscillation amplitude is below 10% of the new characteristic diameter. For higher pressures, the stabilization time was longer than for the transition to 0.5 bar and exceeded 4 minutes (Figure 4.3A). In the first minute, the diameters measurement values of transitions to 4 bar pressure are prone to noticeably high variation coefficient (up to 61%). Largely, this effect can be explained by the shift in the oscillation patterns, that is clearly visible when the measurements are done with a higher sampling rate (every 2 s instead of 20 s, Figure 4.3B). From those graphs the oscillating character of the stabilization process is clearly visible and individual harmonics can be distinguished as well as the differences is the frequencies and amplitudes, corresponding to different pressure transition pairs (Figure 4.3B).

The stabilization time might significantly increase the overall printing time for the structures, where multiple pressure changes are necessary. Similarly, the stabilization might be necessary when e.g., voltage or collector distance are varied during the print. In order to reduce the stabilization time at constant processing parameters – except for the pressure and collector speed – the most straightforward way is by increasing the collector speed during sham construct printing (Figure 4.3C). The possibility to decrease the stabilization time by applying specific pressure transition functions (e.g., linear, exponential, or oscillating) requires further investigation and lies beyond the scope of this study.

Diameter control with collector speed: Extrusion printing technologies (e.g., FDM), can utilize rapid collector movement for a moderate reduction of the fibre diameter [188, 189]. MEW, as demonstrated here, takes a significantly greater advantage of this effect. A MEW fibre is mechanically stretched by the collector only when the collector speed is higher than the jet speed or CTS. Having the upper speed limit fixed at 10000 mm·min^{-1}, the degree of the diameter reduction depended on the CTS and varied between 5- and 8-fold for all applied pressures (Table 4.1, Figure 4.2A). For 2 bar pressure a good agreement (R^2= 0.974) could be demonstrated (Figure 4.2C) of the calculated and the measured diameter values. For the calculation respective D_1 and V_1 values were substituted from Table 1 into the Equation 4.2: $D = 26.67 \cdot \sqrt{420/V}$.

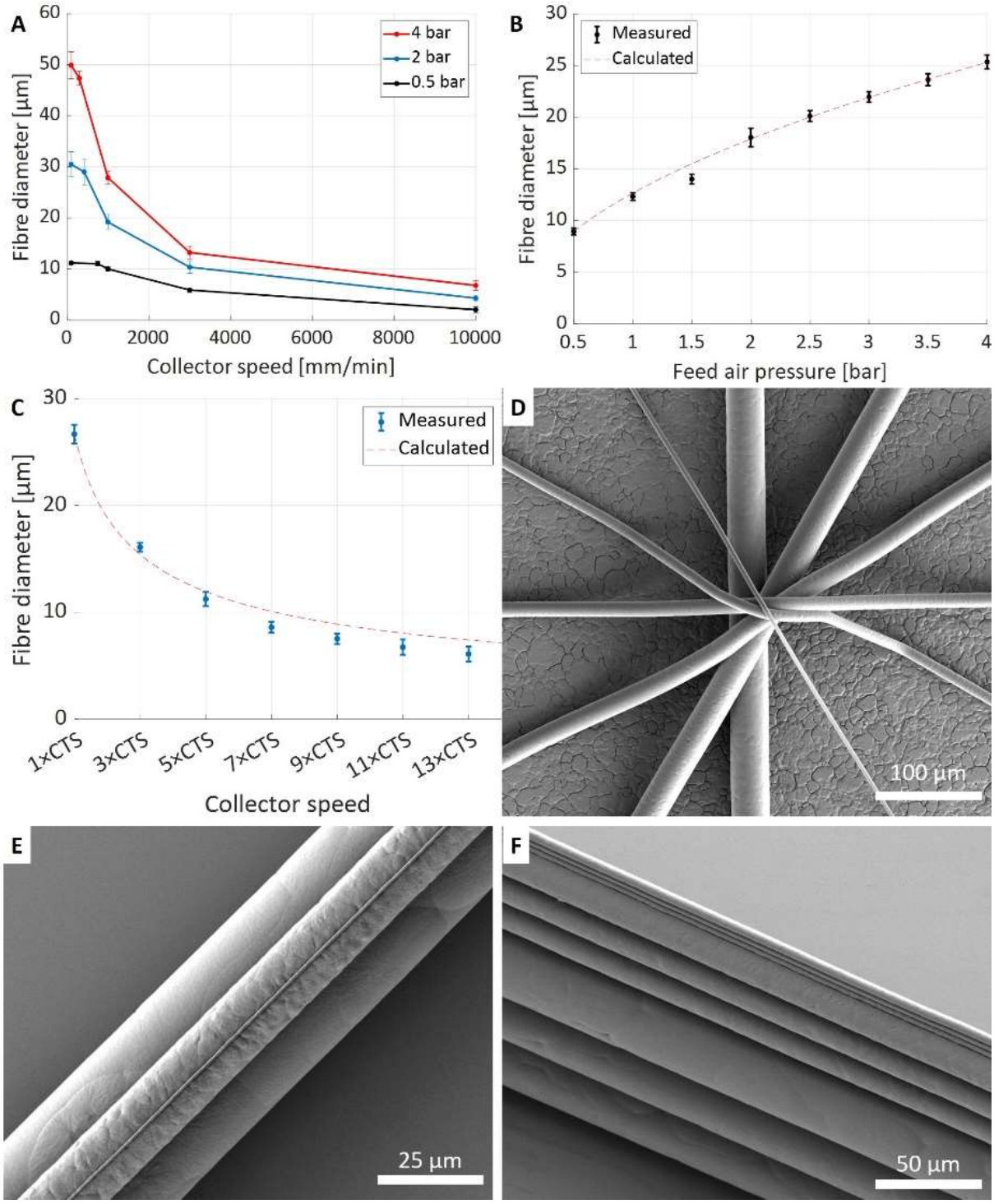

Figure 4.2. A: Fibre diameters measured for the tested three pressures and five collector speed values. No statistical difference was found in the corresponding diameter values for the fibres printed at 100 mm/min and the corresponding CTS (two leftmost points on the graphs). B, C) Calculated curve (red line) of the Equations 4.1 and 4.2 and the measured diameters during pressure and collector speed change respectively D) Scanning electron microscope (SEM) image of PCL fibres with diameters from 5 to 30 µm with 5 µm increment, rotated 30° relative to each other. E, F) SEM images of stacked single fibres and fibre triplets with different diameters.

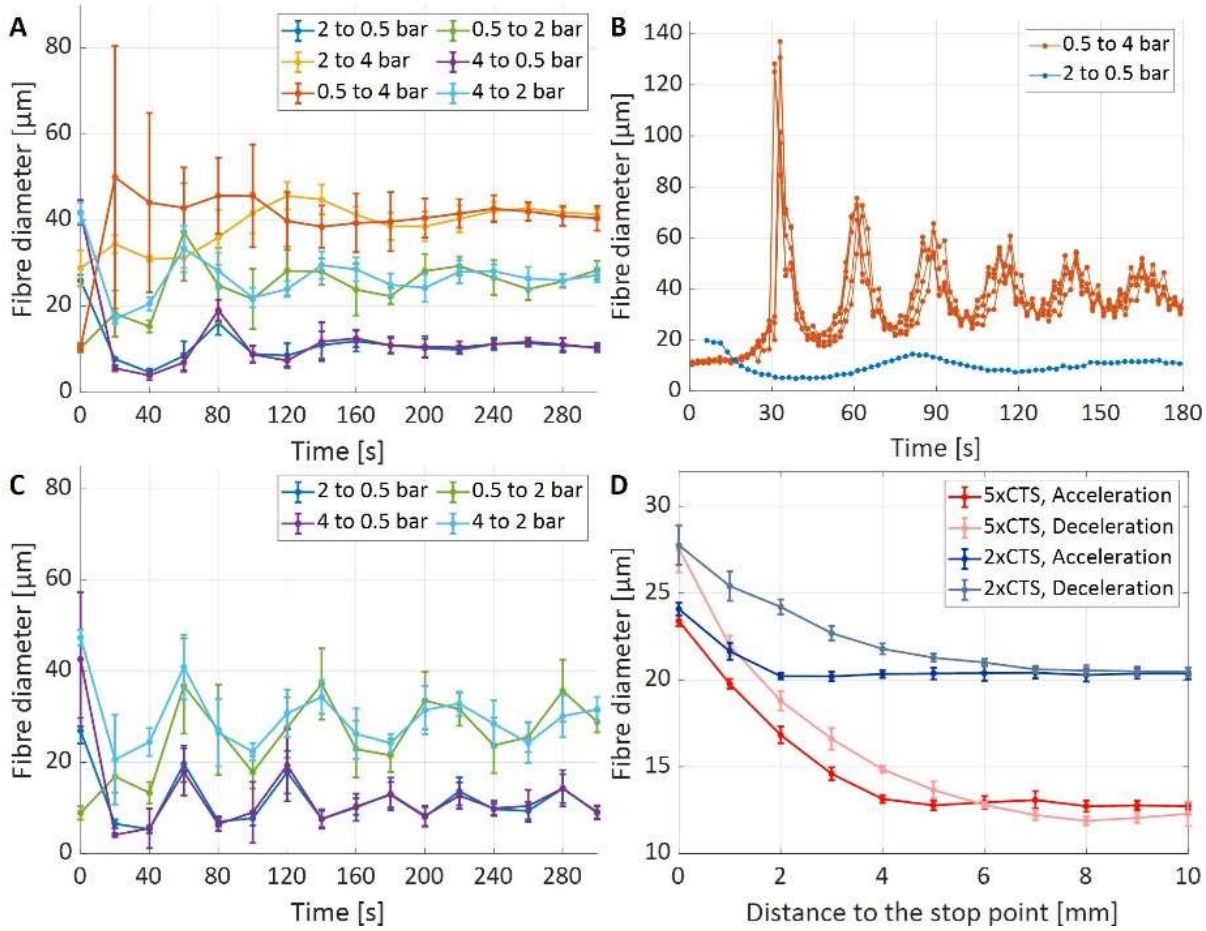

Figure 4.3. A: Fibre diameter measurements during the stabilization conducted at 4×CTS collector speed. Time = 0s point represents the air pressure change moment. B: Individual graphs of fibre diameters, changing after pressure change (five overlay graphs for 0.5 to 4 bar transition and one for 2 to 0.5 bar transition). C: Diameter change graphs obtained while the collector speed during stabilization was equal to 1.15×CTS. D: Fibre diameter change during collector acceleration and deceleration.

The major advantage of collector speed-driven diameter control is that it can be performed almost immediately during a print. However, the length, over which the diameter is changing (Figure 4.3D) can still exceed ten millimetres. For certain applications, this length can be comparable to the whole scaffold dimensions [190]. It is naturally defined by the given speed difference but, in addition, can depend on multiple other factors (stage acceleration or deceleration, viscoelastic properties of the jet).

Change in collector speed additionally affects fibre morphology in terms of surface structure and fibre fusion, which might be associated with jet cooling and flow induced crystallization processes (Figure 4.4, unpublished data by Mr. A. Youssef).

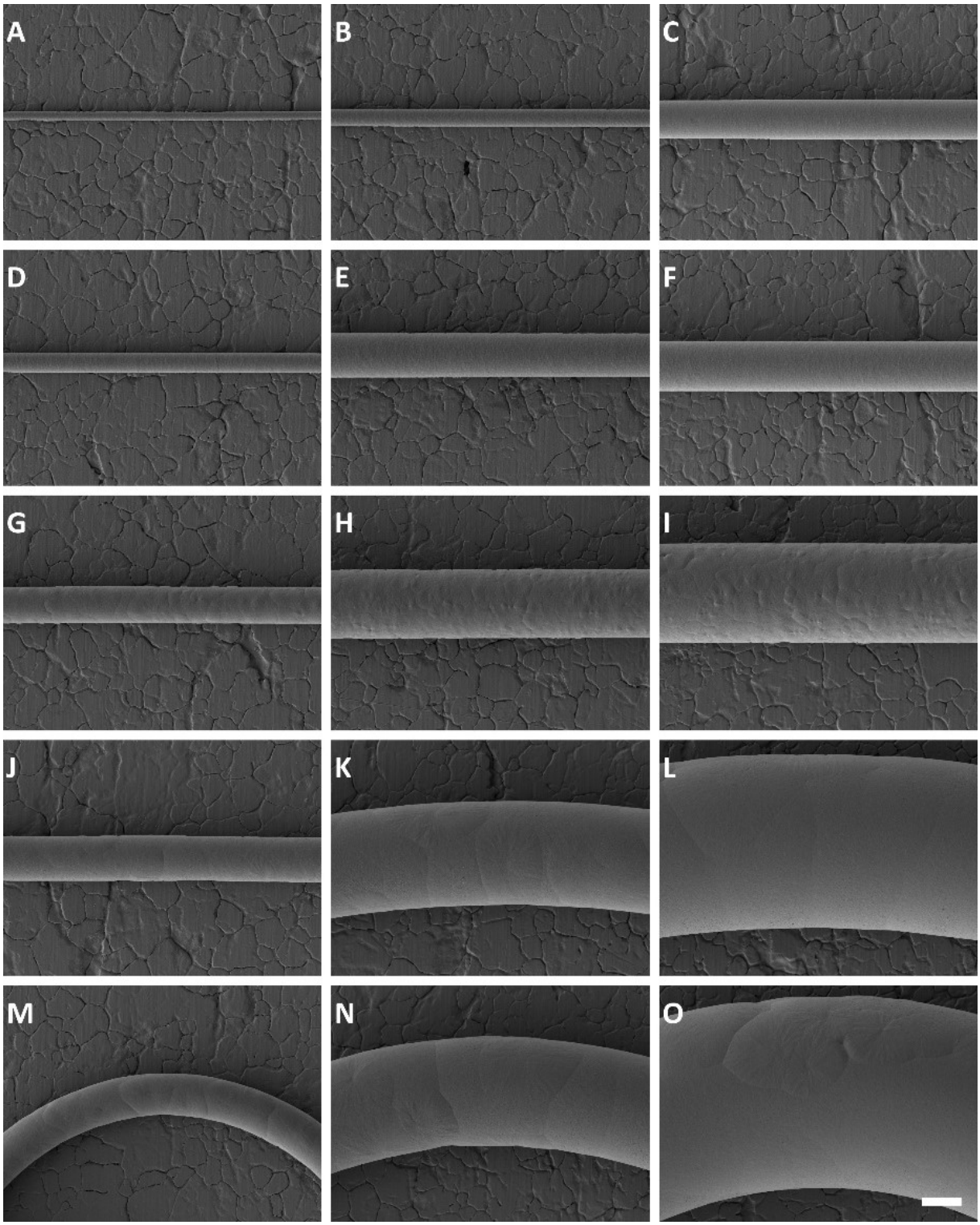

Figure 4.4. Comparison of fibre morphologies for the conditions from the Figure 4.2A. Images are grouped in columns by the applied pressure (0.5, 2 and 4 bar, left to right) and in rows by the collector speed (decreasing from 10000 to 100 mm/min, top to bottom). K-O: Printing speed was below the current critical translation speed. Scale bar 10 µm for all images. Copyright Wiley. Adapted from Ref. [140].

Used simultaneously, pressure and speed variation allow to combine straight fibres with up to 23.45-fold diameter ratio (Figure 4.4). Diameter prediction, while the Equations 4.1 and 4.2 were combined together, $D_2 = D_1 \cdot \sqrt{P_2 V_1 / P_1 V_2}$, is generally less accurate, due to the error summation. Nevertheless, it ensured the accurate printing of fibres with 5±1 µm diameter increment (Figure 4.2D).

Multiphasic and multimodal scaffolds using single nozzles: The ability to print stacked fibres with accurately defined diameters and orientation makes it possible for a variety of multimodal and multiphasic scaffolds to be designed and printed.

The ability to combine various scaffold architectures in a one multiphasic MEW scaffold is first demonstrated with a construct, that combines different pore shapes (Figure 4.5), where eight-layer thick triangular pore scaffold with ~20 µm fibres is separated by a membrane, consisting of ~5 µm suspended fibres was from a scaffold with square pores formed by five layers of ~20 µm fibres square grid. The arrangement of the fibres in the membrane (visibly nearly random) is different from the designed rotated array of straight fibres due to the suspended fibre printing on top of the scaffold with a non-uniform height (intersection peaks) and fibre relaxation effect, observed during high-speed printing (Figure 4.5F). Apart from that, the diameters of the fibres in the membrane are visibly different, consistent with the increased coefficient of variation for printing at a high collector speed. During the seeding of L929 murine fibroblasts, the cells were predominantly attaching to the mesh, yet could be located on the thicker fibre walls after six days in culture. The pore size of 500 µm was too big for the L929 cells to populate the pores within the observed timeframe.

Adding the diameter control by the applied pressure, a MEW construct, consisting of three scaffolds with different pore sizes and fibre diameters was produced (Figure 4.6). Scaffold 1 (10 µm diameter fibres; 125 µm spacing) was printed together with a large pore MEW scaffold (Scaffold 3; 10 µm diameter fibres; 250 µm spacing) on top of it and a membrane between them (Scaffold 2; 4 µm fibres with pseudo-random orientation, pore size <50 µm) were fabricated with a single nozzle, as a single print. The rendering of the scaffold design (Figure 4.6A) shows how the scaffolds were supposed to be layered together. The whole printed construct (Figure 4.6B) has a circular area in the middle, that is designed for cell-seeding. SEM images of the microstructure (Figure 4.6C, D) proves the precise layering of

the scaffolds as well as the individual fibres inside the layers of the Scaffolds 1 and 3. The small diameter fibres of the scaffold 2 are incorporated into the construct in order to increase the cell seeding efficiency. For their manufacturing, the pressure was kept the same as for the scaffold one, but the printing speed was increased.

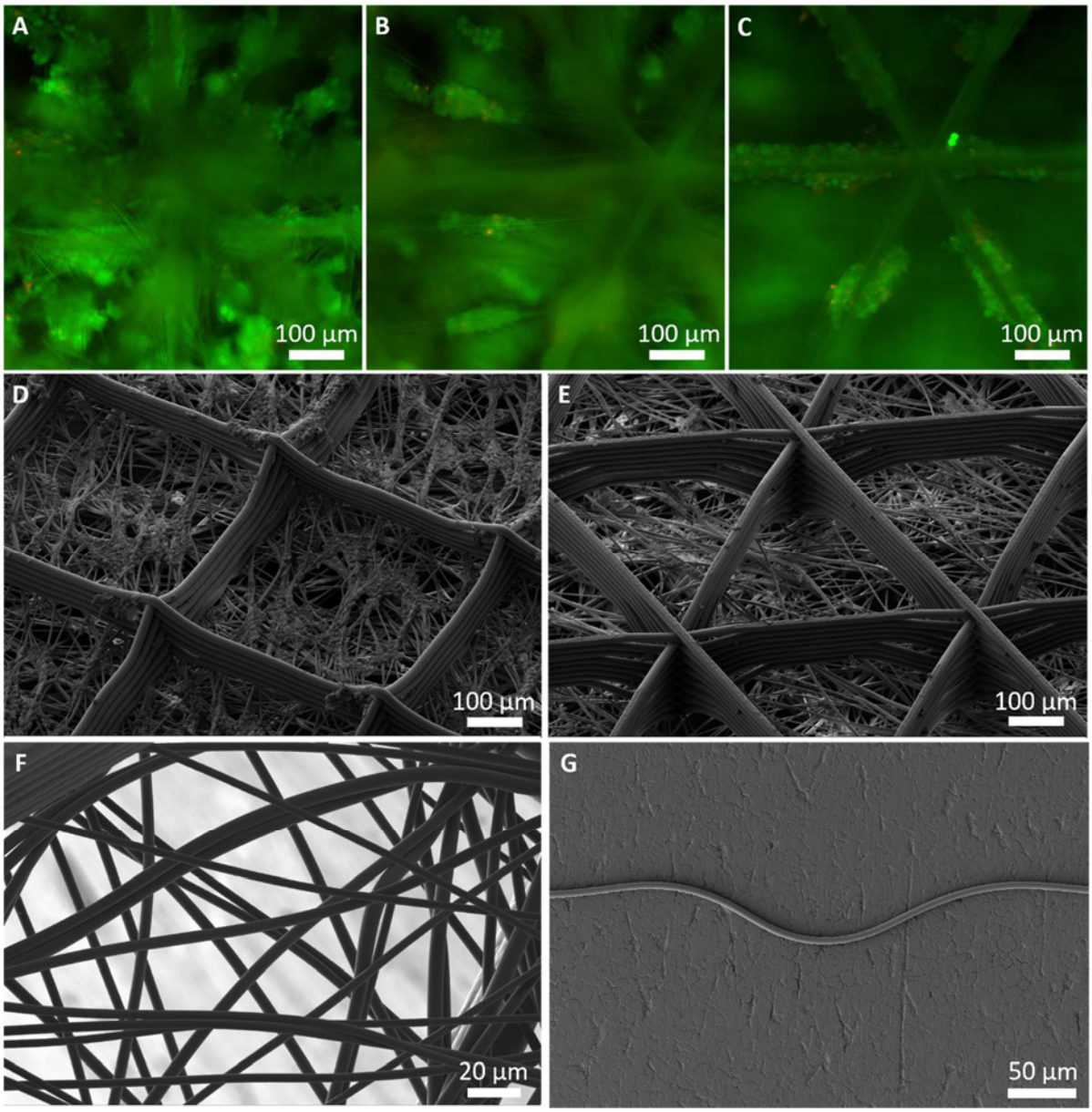

Figure 4.5. L929 murine fibroblasts on the scaffold with square and triangular pores. A-C: Live/dead staining of L929 murine fibroblasts on the scaffold with square and triangular pores, showing viable (green) and dead cells (red), Day 6. Focal plane on the level with the square pore scaffold (A) and the random pore membrane on the top side of the scaffold, bottom side of the with random pore membrane (B) and triangular pore scaffold (C). D-F: Scanning electron microscope (SEM) images of the same type of scaffold from both sides and the membrane, respectively. G: SEM image of a non-linear MEW fibre segment printed while the collector was moving along a straight line at 10000 mm/min.

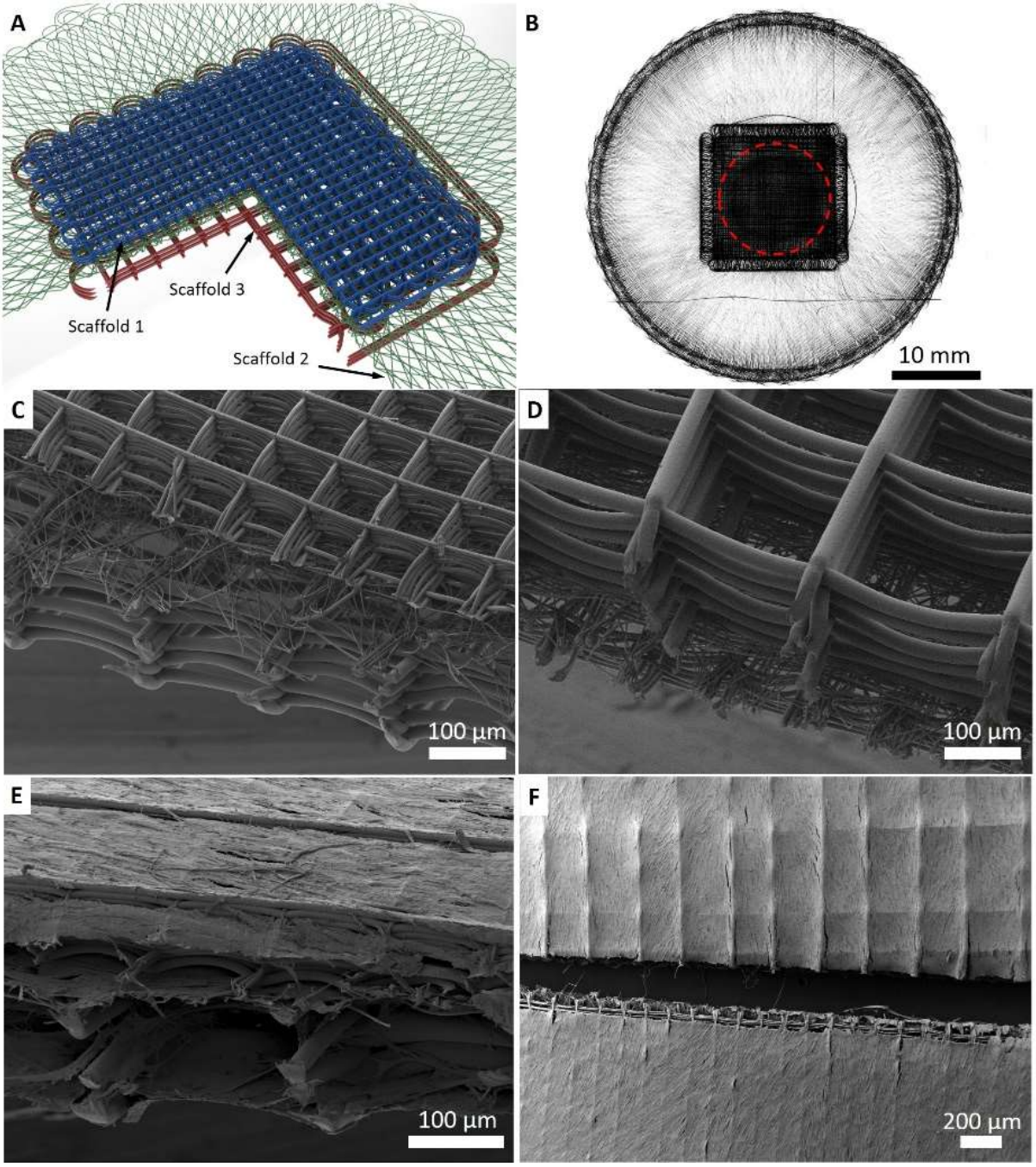

Figure 4.6. Example of a multiphasic scaffold. A) A rendering of a construct illustrating the design, containing three scaffolds B) A stereomicroscopic image of a printed construct with Scaffolds 1 and 3 in the centre. The excess part of the scaffold 2 around them was required for the sufficient jet stretching at high collector speed. Area, apt for cell seeding is inside the red dashed circle. C, D) Close-up SEM images of the construct cross-section from both sides. E) The cross-section SEM image (Scaffold 1 on top) with hMSCs after 21 days *in vitro*. F) Top view of both sides of the construct after 21 days *in vitro*. B-F: Copyright Wiley. Adapted from Ref. [140].

The circular area around the square scaffolds 1 and 3 serves to provide sufficient length for the axis acceleration and corresponding diameter reduction. This approach eliminates one stabilization cycle but leads to extended printing path and, thus material waste. The excessive material could be readily removed by laser cutting prior to cell culture experiments. In the current case the high printing speed was also indispensable because it additionally provides improved fibre suspension (see Chapter 7).

HMSCs, seeded on the scaffolds, were actively proliferating, and penetrated through the construct, forming cell sheets on the outer surfaces of the Scaffolds 1 and 3 as well as on both sides of the fibre membrane in between (Figure 4.6E) by the day 21. Gradually the whole upper and bottom surfaces of the construct were covered by the cells (Figure 4.6F and 4.7).

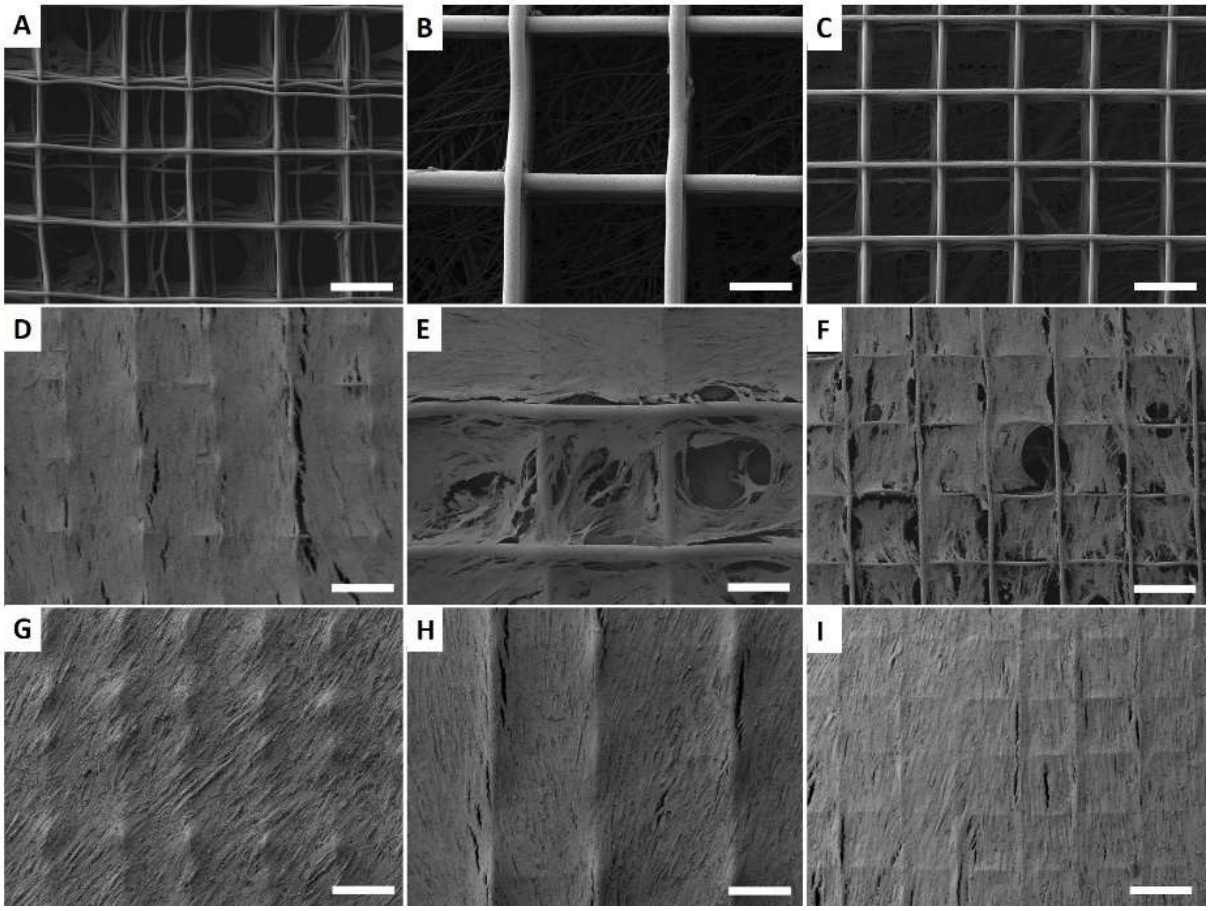

Figure 4.7. Comparison of MSCs morphologies. Images are grouped in columns by the scaffold type from left to right: A box scaffold with the fibre diameter and spacing, equivalent to the scaffold 1 and three-layer construct with the view on the scaffold 3 and scaffold 1 respectively. The images are grouped from top to bottom by the day count. A-C represent Day 1, D-F - Day 7 and G-I - Day 21 *in vitro* respectively. All scale bars 250 µm. Copyright Wiley. Figure adapted from Ref. [140].

An expected improvement of the cell seeding efficiency by the Scaffold 2 could not, however, be demonstrated (Figure 4.7) due to the sufficient fibre surface area of the negative control sample (125µm spacing, total thickness comparable to the multiphasic construct) as well as irregular fibre placement on top of this scaffold, which could have a similar cell-catching effect.

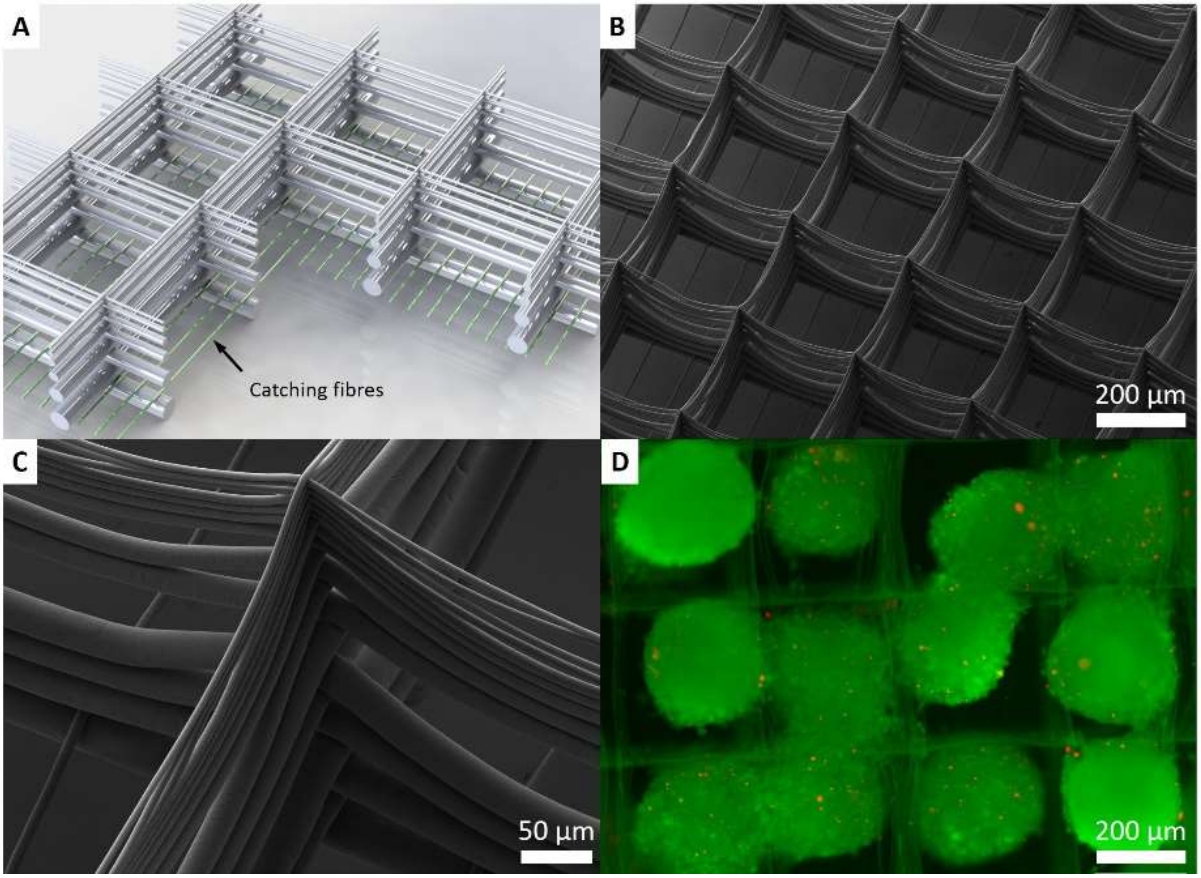

Figure 4.8. Multimodal scaffold for tissue spheroid seeding. A: A schematic illustration of a multimodal scaffold with decreasing pore wall thickness. B, C: Scanning electron microscope images of the printed scaffold with 14 fibre layers in two orthogonal directions with diameters decreasing from 40 to 4 µm, stacked on top of each other. Small diameter (7.5 µm) catching fibres are incorporated between the first two bottom fibre layers in order to keep human adipose stem cell spheroids (E) from falling through the scaffold (live/dead staining 24 h after seeding showing viable (green) and dead cells (red). Copyright Wiley. Adapted from Ref. [140].

A specialized scaffold for tissue spheroids is another example of multimodal scaffold design (Figure 4.8). The layer-by-layer fibre diameter adjustment created a pore size gradient and gradually decreases the stiffness of the pore walls from the bottom to the top of the scaffold, while thick fibres of the bottom layers provide a structural support that facilitates

scaffold handling. Incorporation of two thin catching fibres per square pore into the first layer prevented the spheroids from falling through the scaffold during the seeding. Including thinner fibres (7.5 µm) for this purpose into the same layer with the thick fibres helped to maximize the useful pore volume of the scaffold.

The diameter of the fibres inside the pore walls gradually decreased from 40 µm at the bottom of the scaffold to 4µm in the topmost fibre layer. During printing the fibres were divided into three groups. Within each group the pressure stayed constant and the collector speed linearly increased, proportional to the layer count.

Chapter 5: Fibre stacking and placement control

5.1 Introduction

During MEW, a fibre can be deposited directly on the collector surface, on top of the other fibres, get attached to their side or even be suspended in the air (Figure 5.1A). As mentioned in previous Chapters, ideal vertical stacking of the fibres is an intrinsic feature of MEW, while appropriate materials are used and, in many cases, a desired result. It also simplifies the collector movement programming, because for printing of multiple layers, it is sufficient to repeat the same trajectory for each layer. An exception has to be made in case of thick structures only [60], when a proportional increase of collector distance is required. At the same time, the affinity of the fibres to the uppermost objects on the collector, be it already deposited fibres or an element of the designed collector shape, can prevent fibre deposition in the designed locations (Figure 5.1B) and cause defects in the printed constructs. The undesired side of this effect prevents the manufacturing of MEW scaffolds with deliberately small regular-shaped pores [61]. While the 'autofocusing' effect, can assist the accurate layer by layer patten reproduction, it also limits the design of the MEW scaffolds to structures with vertical walls and constant pore geometry along the scaffold thickness. Partially it can be overcome by the introduction of suspended structures (see Chapter 7, Ref. [191]). It is, however, applicable for straight fibres only. Another controlled deviation from that behaviour was demonstrated by de Ruijter et. al., when 'off-plane' fibres were positioned at a controlled angle to a fibre wall or even on its side [192].

The finite element analysis of the electrical field between the nozzle and the collector demonstrates the electrical field lines going from the nozzle to the collector (Figure 5.1C) and can indicate a probable fibre landing area. At the moment, however, it can be useful only for a qualitative evaluation of the printing setup and suggest only the possible jet trajectory since it does not take into account the mechanical properties of the jet and its inertia. Another factor, which is necessary for accurate quantitative predictions is the charge density in the jet and residual charge of the deposited fibres. Although it was claimed that the jet charge density can be derived from the current, flowing through it [193], this assumption ignores the charge dissipation mechanisms, discussed in Chapter 2. A study by Ding et. al. [90] developed a mathematical model for the prediction of fibre position relative to deposited one, distinguishing two scenarios – for a conductive and a non-conductive substrate. Since the

same result could not be reproduced under similar conditions (data not shown), additional factors can be influencing the charge elimination from the deposited fibres.

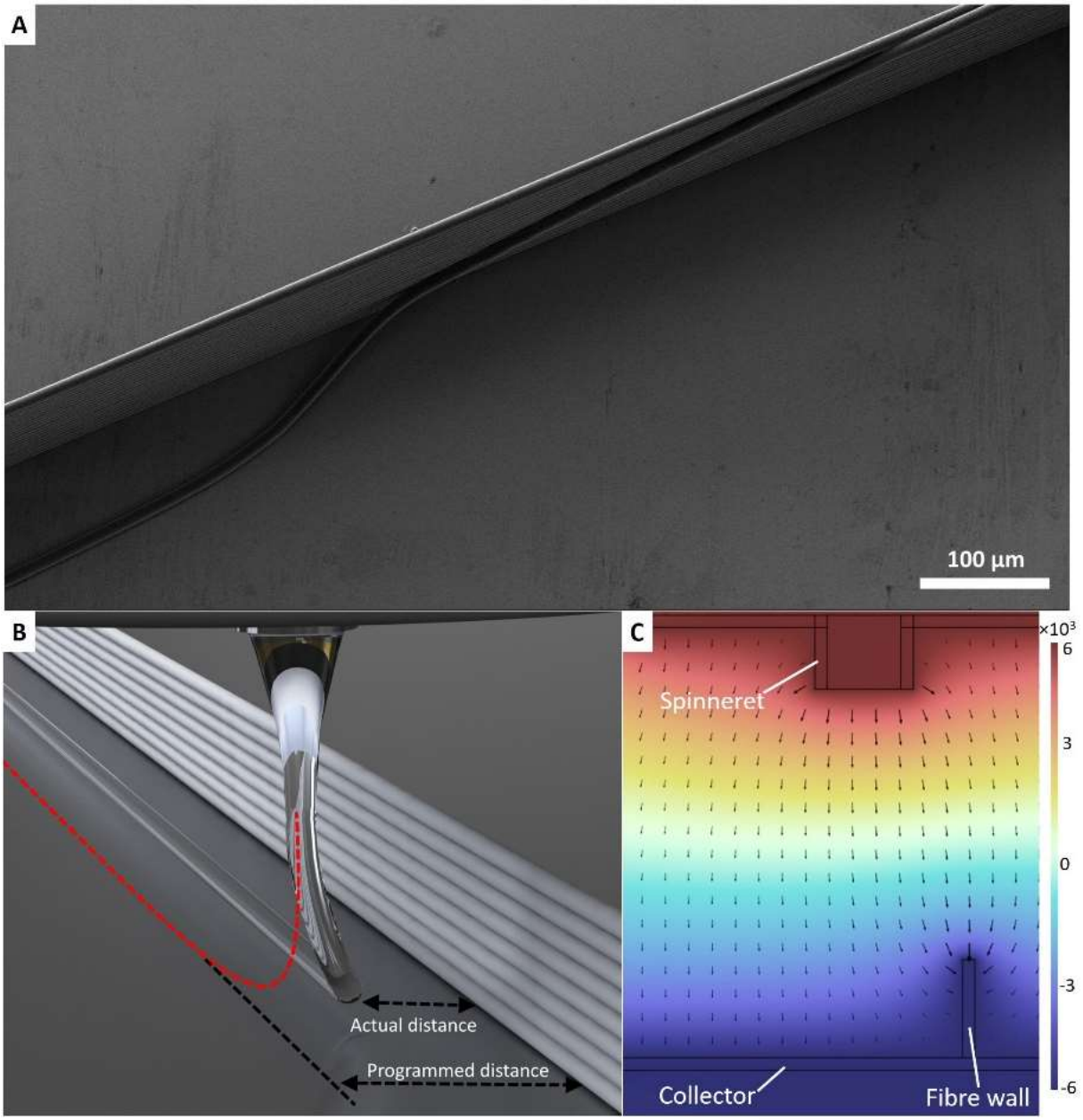

Figure 5.1. A: SEM image of a melt electrowritten (MEW) fibre, nominally printed next to the fibre wall and attracted to it. B: Schematic rendering of a MEW jet. C: Finite element analysis simulation of a n electrical field between the nozzle and collector.

The situation changes profoundly when a scaffold printing pattern contains curved elements, e.g., circles or sinusoidal lines. The morphology of the curved fibre walls tends to change slightly with each layer [194]. This phenomenon suggested a printing approach, when the collector movement path is changing for each stacked fibre layer. As demonstrated below

it does not just eliminate the unwanted fibre path changes but provides a tool for creation of and virtually unbounded spectrum of geometrical elements within MEW scaffolds.

5.2 Materials and methods

The electric field simulation was performed with Comsol Multiphysics 5.3A (Comsol Inc., USA). The experiments, investigating the effect of the previously deposited structures on the on the newly deposited fibre, printed next to them were performed with PURAC PC-12 PCL (Corbion, Netherlands) as a printing material. Air pressure of 0,5 bar was applied to the syringe, heated up to 73±1°C. Glass slides (1.1 mm thick) were placed on a stainless-steel collector. Unless specified otherwise, the distance between the glass surface and the tip of a 22G nozzle (Nordson EFD, USA) was set to 3.5 mm. 850 mm/min collector speed was chosen in order to exceed the CTS for all voltage/collector distance combinations. For various fibre wall heights, minimal distance, at which a fibre could be printed on the collector, was determined in the range between 50 and 500 µm with a 10 µm step (Figure 5.2). For each tested condition measurements were made on *n*=5 samples.

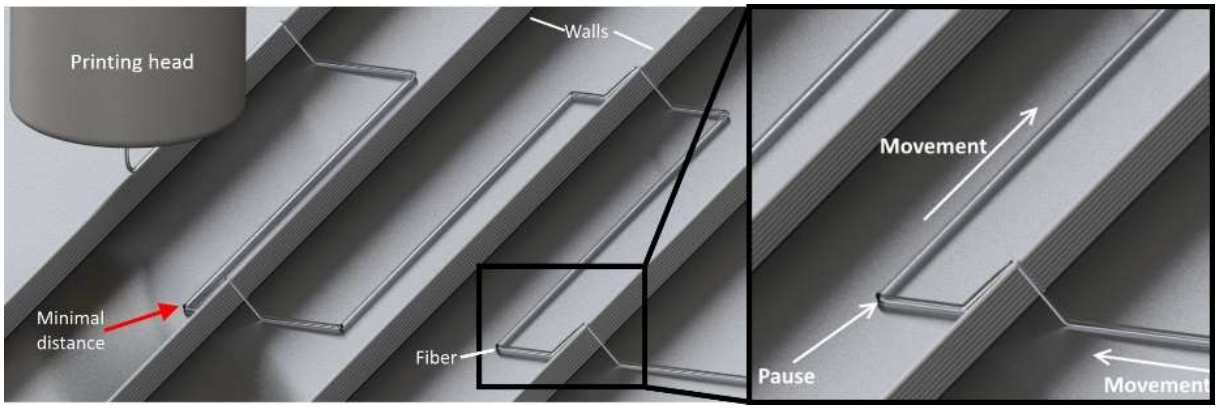

Figure 5.2. Schematic of the experimental setup for the measurement of the distance between the deposited fibre and a previously printed fibre wall.

During micro shifting experiments the polymer temperature and the air pressure were increased to 75±1°C and 1.2 bar, respectively. The applied voltage was changed to -1.5 kV for the collector voltage and +5.75 kV for the nozzle. The printing speed was set to 1.25×CTS, which varied between 180 and 230 $mm \cdot min^{-1}$, depending on the polymer state and environmental conditions (19–22°C air temperature and 35–42% rH). All structures are printed with 20 fibre layers.

Distance measurements and sample imaging were performed on a Crossbeam340 electron microscope (Carl Zeiss Microscopy, Germany). The samples were preliminary sputtered with 4 nm of platinum using a Leica EM ACE600 sputter coater (Leica Microsystems, Germany). Measurement results are presented as mean ± standard deviation. One-way ANOVA was performed to define the statistical significance with a Tukey post-hot test ($p<0.05$). The design and manufacturing of the scaffolds, demonstrated in Figure 5.7, was done by Dr. I. Liashenko.

5.3 Results and discussion

The height of the deposited structure has the most significant impact on the attraction of the deposited fibre under given experimental conditions. Thus, the minimal placement distance is growing nearly 8-fold while the preliminary printed wall height grows from 10 to 200 µm (Figure 5.3A). The SEM images of a fibre crossing the wall and moving parallel to it, corresponding to those border cases, are presented in the Figure 5.3B and C. As a countermeasure, similar to the positioning of single fibres next to each other (Chapter 3) a setup with a smaller collector distance and applied voltage can be useful. Such setups, however are not always applicable : Previously Wunner et al. [60] discovered that it is possible to increase the thickness of the scaffolds, avoiding stacking and pulsing defects by a simultaneous increase of collector distance and the voltage. As shown in Figure 5.3D, this strategy might be a challenging if such a scaffold by design contains regions with different heights, located close to each other, increasing the risk of attraction of the deposited fibre to the scaffold's elements with an increased height. For the case of lower voltage and smaller collector distance the CTS was much lower than for the high voltage and greater collector distance, causing a difference in the diameter of the fibre segments (Figure 5.3E, F) where the collector stops for a pause (Figure 5.2). This difference in the fibre diameter could affect the measurement results. Nevertheless, the pause point in the collector path was necessary to prevent the collector movement parallel to the wall before the jet has crossed it. In those instances, the original attachment of the fibre to the wall would prevent it from falling on the collector at the characteristic distance (Figure 5.4).

When a fibre is deposited on the collector surface next to the wall, the previously printed structure influences its position. Analogous to the minimal deposition distance, the higher the fibre wall, the stronger it is pulled from its programmed position (Figure 5.5): For a

20-fibre high wall this difference reaches 100 µm. Higher structures also keep the attracting effect at a much greater distance. This effect can have a profound influence on the resulting construct accuracy and has therefore to be considered during the path programming. It is not typically observed in conventional MEW scaffolds since the difference in structure height is normally close to one fibre thickness.

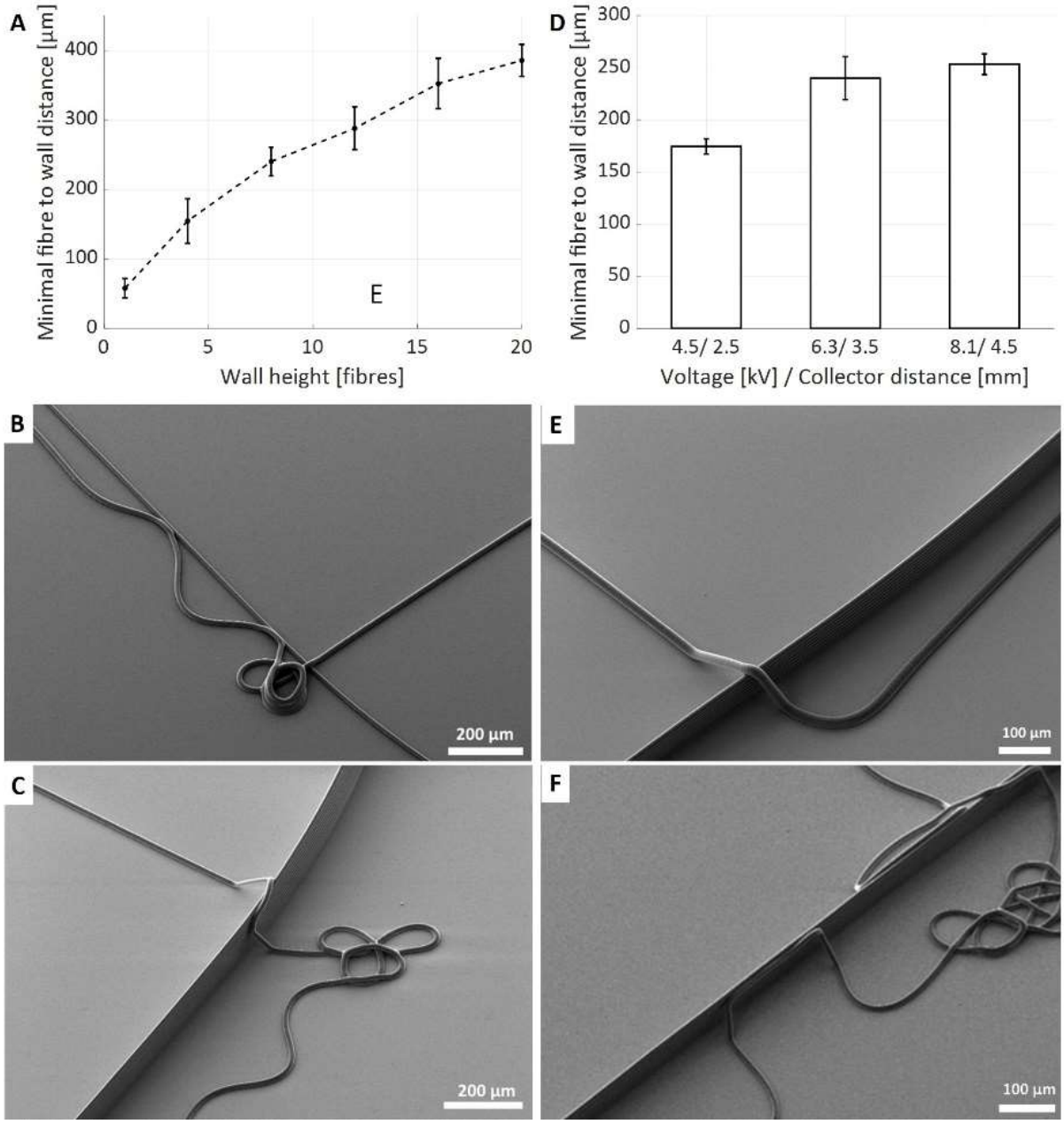

Figure 5.3. A-C: The effect of a wall height on a minimal distance of fibre placement next to it and SEM images of the areas where the fibre crosses the wall for one and 20 fibres in the wall. D-F: The effect of a simultaneous voltage and collector distance increase on the minimal placement distance.

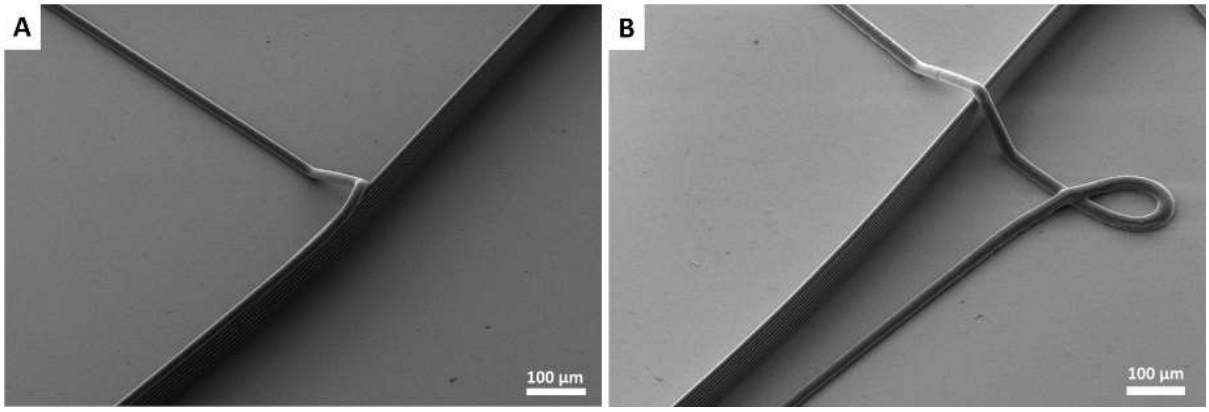

Figure 5.4. The effect of collector movement pauses in the points after the fibre crossed the wall and before the movement parallel to it starts. A: 0.05 s pause, fibre says on the wall. B: 0.45 s pause, fibre is deposited on the collector surface.

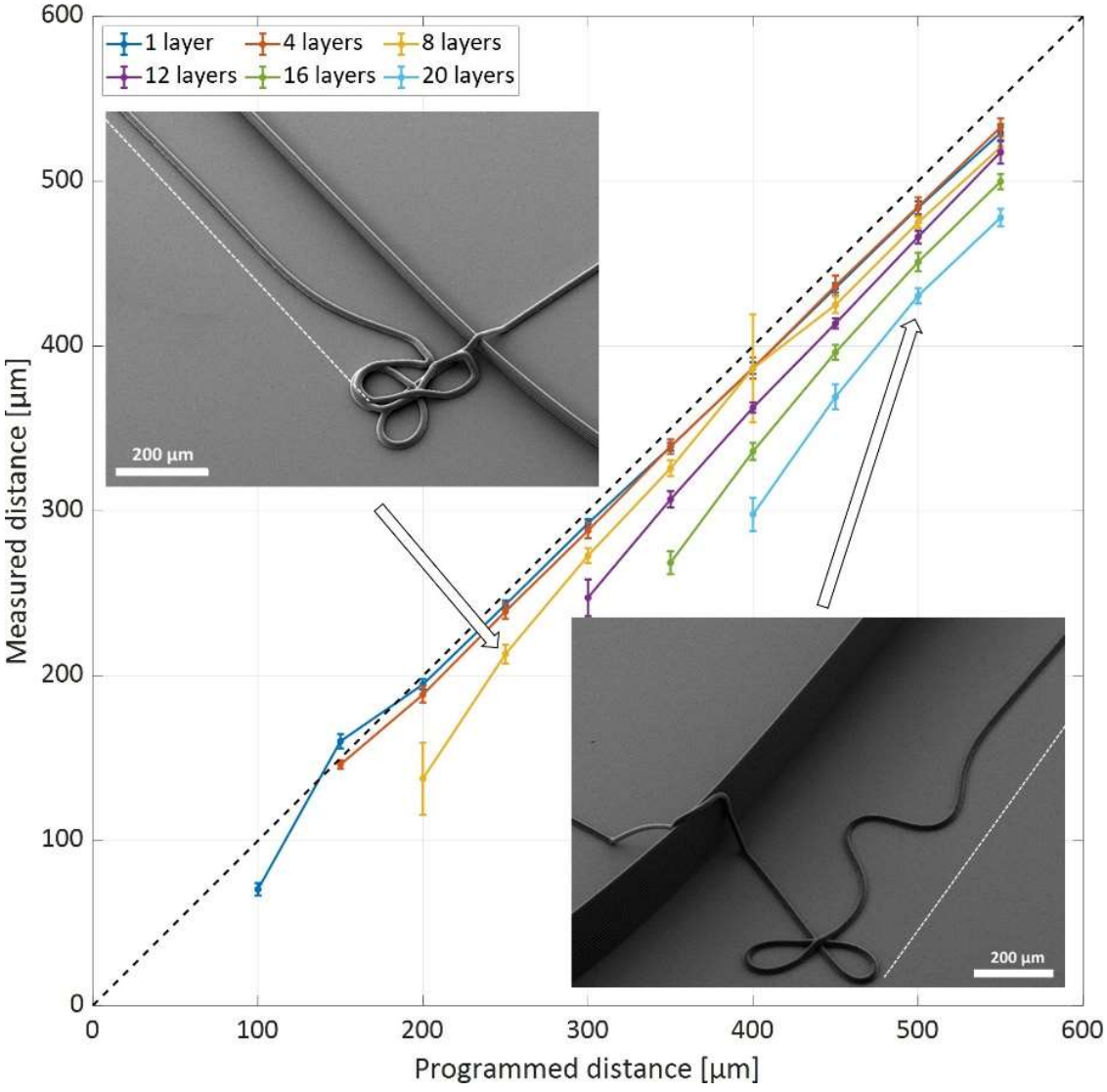

Figure 5.5. A comparison of a programmed distance from a fibre to the wall with the measured distance.

With the increase of scaffold complexity and corresponding height irregularities the programmed fibre placement trajectory recalculation might be necessary. A layer-by-layer programmed collector path adjustment can already be used for elimination of printing errors and creation of novel structures. A fibre wall, made of stacked fibres, printed while a collector is moving along a sine line with a given amplitude and wavelength is a good demonstration example. When the same collector movement in the XY plane is repeated for all fibre layers, the amplitude of the lines is decreasing each layer (Figure 5.6A). Possible reasons of this layer-by-layer printed path change are discussed in Chapter 7.

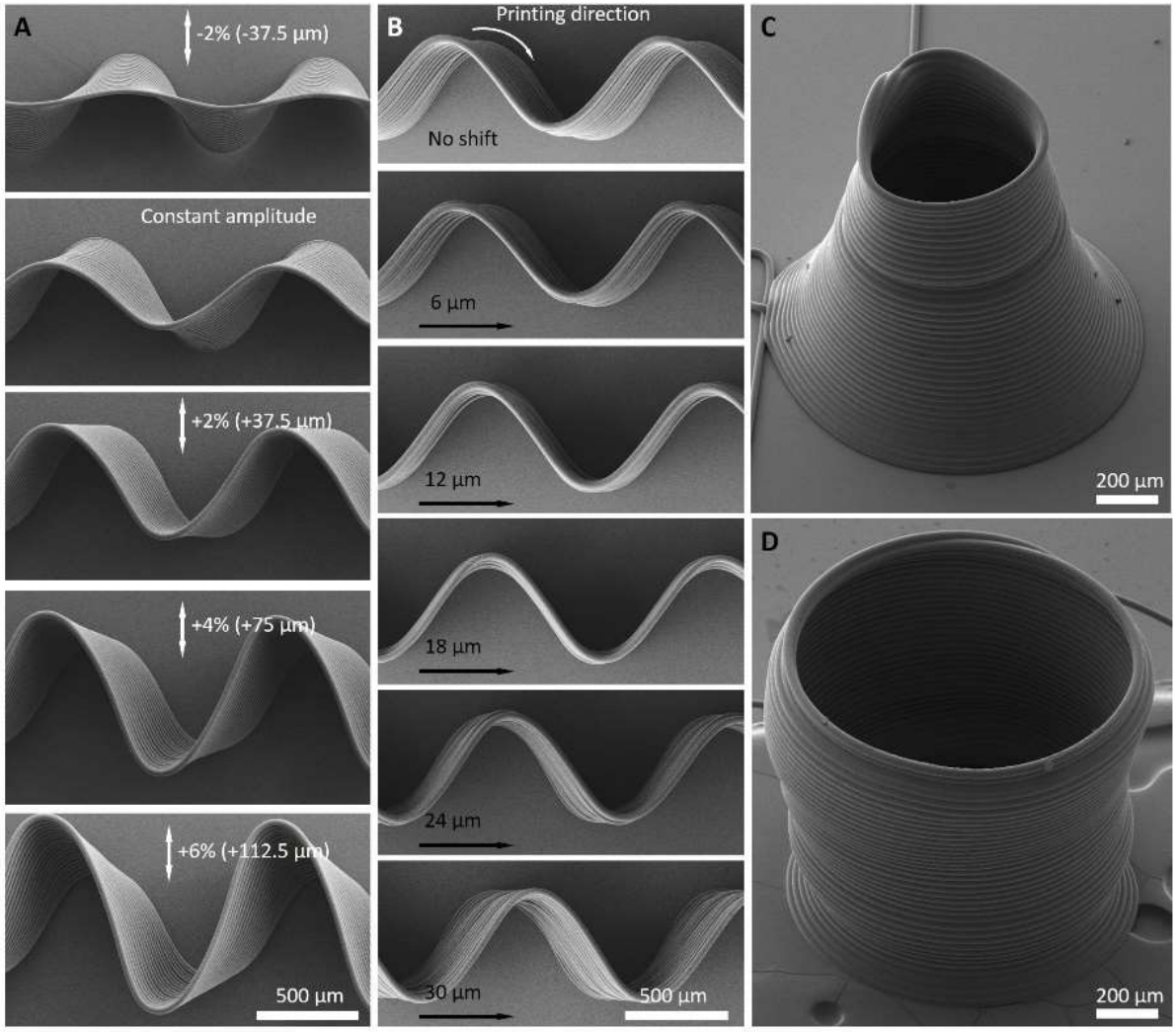

Figure 5.6. A, B: SEM images of a 20-layer fibre walls melt-electrowritten with a constant amplitude and with an amplitude, changing for each layer (A) and changing 'phase' shift against the main printing direction (B), C: SEM images of 40 layers thick nominally cylindrical structures, printed without path correction (C) and with a constant (25µm) radius increase per layer. Adapted from Ref. [194].

By changing the programmed sine trajectory amplitude, it was possible to accelerate the amplitude decrease, compensate it and even gradually increase the printed path amplitude, thus demonstrating the ability of a controlled manufacturing of overhanging structures in MEW.

In addition to the amplitude change, each new layer was undergoing a displacement in the direction, parallel to the X-axis and opposite to the printing direction (Figure 5.6B). This error could also be corrected by introduction of a corresponding shift in a programmed path for each layer. The necessary correction that compensated the printing error and resulted in perfectly vertical fibre walls was different for the amplitude increase (37.4 µm) and the phase shift (18 µm), which means that those correction values are not universal and depend on the trajectory. It is remarkable that in both cases the necessary correction linearly depended on the layer count. For other shapes, e.g., for cylinders it was not the case: The radius of nominally cylindrical structures was decreasing non-linearly (Figure 5.6C) and a correction with a constant radius increment per layer lead to quasi-cylindrical structure with an irregular wall radius (Figure 5.6D). While the 25µm per layer radius increase, investigated here, was not sufficient for the elimination of the rapid narrowing bottom layers, it could balance the tilt for the middle region and cause the 'well' diameter to increase on the top of the structure. Nevertheless, linear correction alone is sufficient for a significant expansion of MEW scaffold designs by adding tilted and overhanging wall segments (Figure 5.7).

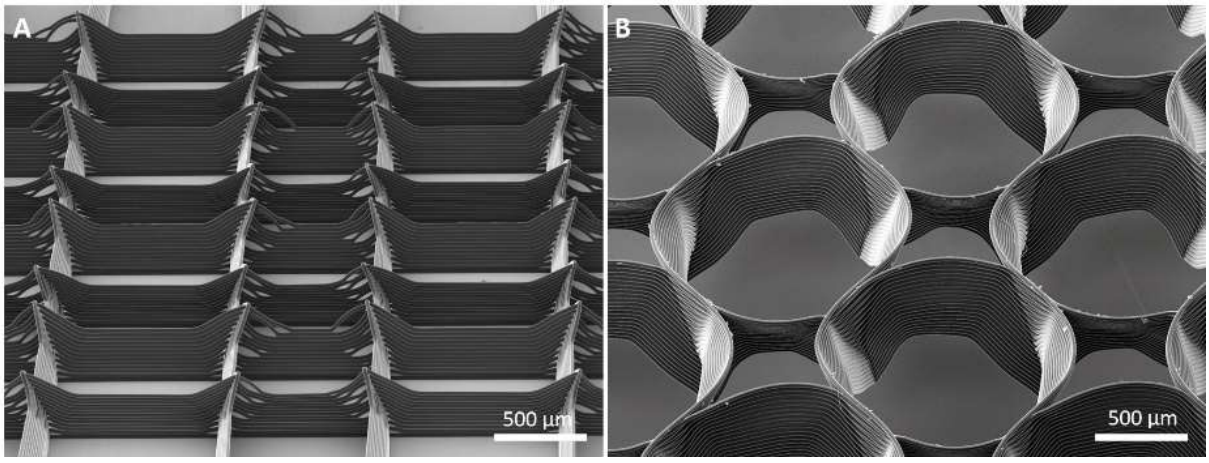

Figure 5.7. Scanning electron microscopy images of melt-electrowritten scaffolds, manufactured with a layer-by-layer path shifting. A: A scaffold with tilted linear walls. B: A scaffold with converging circular pores, formed by converging sinusoidal walls. Copyright Wiley. Adapted from Ref. [194].

Chapter 6: Prediction of fibre placement

6.1 Introduction

Additive manufacturing has played a major role in changing the manufacturing paradigms over the recent decades and expanded the boundaries of complexity, resolution, and production speed of multiple products. Nevertheless, every additive manufacturing technology has its limits in terms of realizable feature sizes and shapes, restricting its application. There are multiple guidelines, which take those limitations into consideration and assist in design of an object, that can be readily produced by an additive manufacturing technology of a choice [195]. Even following those guidelines, shape and dimension deviations from the original design are still inevitable. A difference between the design and the actual produced part varies from method to method but can be quite noticeable [40, 196]. Whereas for most additive manufacturing technologies the design is represented by a 3D CAD model (typically an *.stl file), for MEW at the current stage of development it is necessary to specify the printing path in the form of a G-code. On one hand this process is tedious and error-prone but on the other hand it is often necessary to make fine adjustments into the printing path, changing the speed or trajectory to achieve the desired result. Another important aspect here is that the jet cannot be interrupted and started again in an arbitrary location which puts additional limitations on the design of MEW structures.

While in Chapter 4 it was shown that the fibre diameter adjustment can be made with high resolution and stability of results, compared to other extrusion-based additive manufacturing technologies [140], the challenge remains in the precise prediction of fibre placement. In addition to the printing errors, causes by the attraction of a newly printed fibre by already deposited structures (see Chapters 3 and 5), already the first deposited layer can differ already from the programmed printing path. When the positions of the fibres in the very first layer are already compromised, they automatically affect the whole structure. Elimination of those errors at the moment requires manual parameter or printing path adjustment [194]. The difference between the programmed path and the printed fibre layout is especially noticeable when curved path segments are printed. To avoid this effect, the vast majority of MEW scaffolds in the literature are built of linear fibre arrays. Since non-linear structures are crucial for recreation of morphology and mechanical properties of living tissues [115], it is of utter importance to increase the predictability MEW printing.

A clear discrepancy between the programmed stage movement path and the deposited fibre trajectory, is present not only for curves but also near the junctions of straight segments (Figure 6.1A). The main reason behind this discrepancy is the presence of a jet lag, which is represented here by a line, connecting the projection of the nozzle position (NP) on the collector and the point where the jet touches the collector surface (jet contact point, JCP) (Figure 6.1B). The movement of the NP in the collector plane corresponds to the actual collector movement while the JCP movement trajectory can deviate from it (Figure 6.1C) [136, 140].

On the straight path segments with sufficient length NP velocity ($\boldsymbol{V}_{NP}$) and JCP velocity ($\boldsymbol{V}_{JCP}$) coincide, however, when the movement direction changes, they start to differ both in direction and magnitude. The variation of the jet lag due to changes in processing [137, 143] and environmental (i.e., air temperature and humidity) parameters makes the fibre placement prediction more complicated. When the jet is unstable, the lag is also changing over time which makes the appropriate selection of parameters, that do not allow fibre pulsing [182] a must. Similarly, a sufficient stabilization time is required to remove temporary pulsing from jets (Chapter 4).

It is possible to reduce the influence of the lag on the printing quality by making it smaller [51]. Matching the collector speed and the speed of the material in the jet near the JCP makes the laydown pattern nearly correspond the programmed path. The jet speed in MEW is usually represented by the CTS [47]. Since the CTS depends on the printing conditions, it needs to be accurately measured before each print to avoid the lag appearance or coiling. However, making the collector speed equal to the CTS does not eliminate the jet lag completely (Figure 6.1D): In this case it is a result of the resistance of the jet to bending depends on the mechanical properties of the jet. This bending radius can range from the values, comparable to the radius of the jet (low viscosity liquid) [197] to the magnitudes, significantly exceeding it (elastic rod) [198], depending on the jet geometry, temperature and material properties.

The main disadvantages of using CTS as a set collector speed in MEW is the inability to rapidly increase the fibre diameter during a print by the collector deceleration (Chapter 4 and Ref. [140]) and increased printing time since the CTS is the slowest collector speed allowing straight fibre printing at the given printing parameter values.

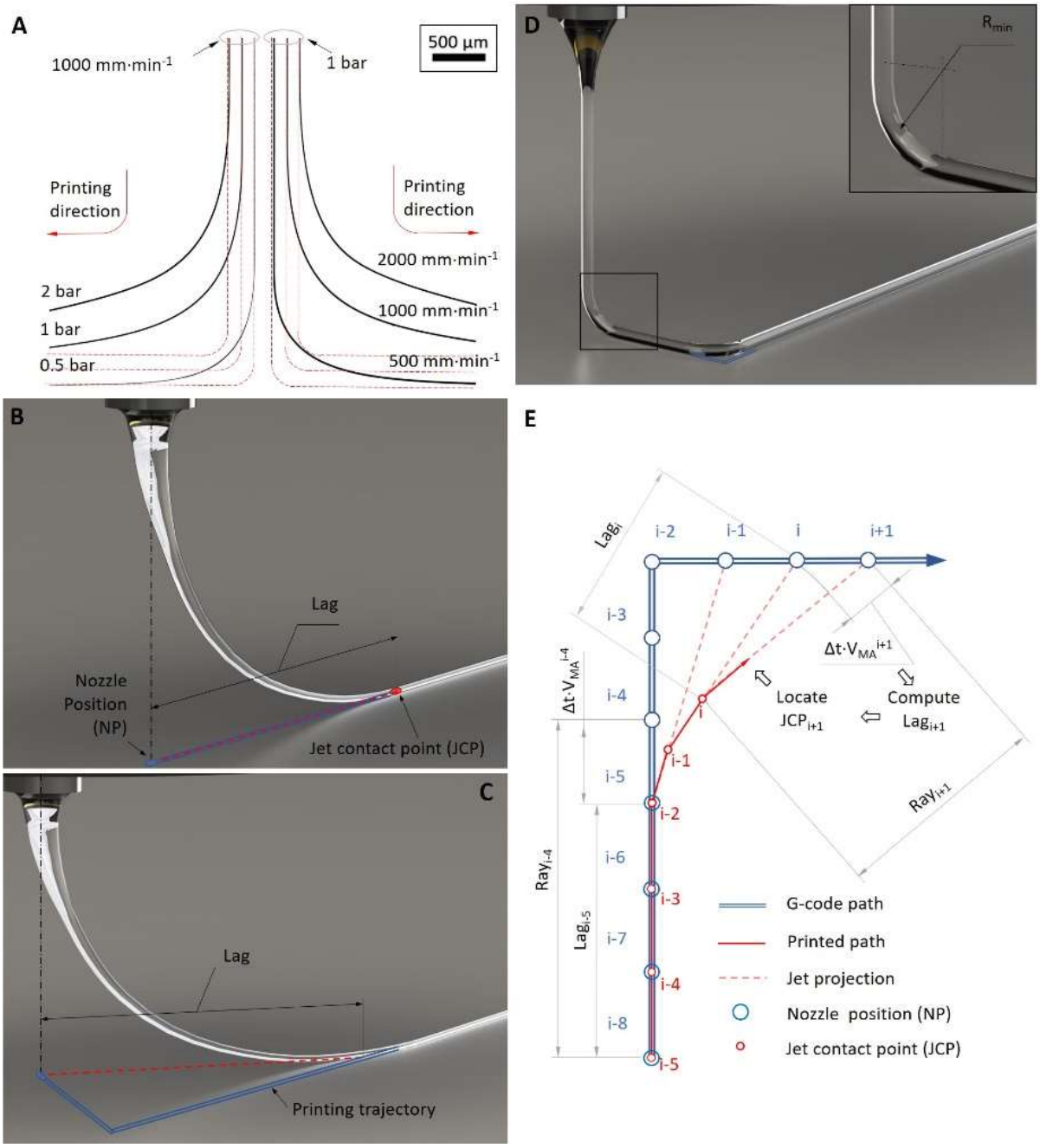

Figure 6.1. A: A microscopic image, illustrating the difference between the printed fibre and collector movement trajectory for varying collector speed and pressure. B: Schematic of a melt electrowriting (MEW) jet, printed along a straight line above the critical translation speed (CTS). C, D: Schematic of a MEW jet near a path turning point while the collector is moving faster than CTS (C) and at the CTS (D). E: A principle of point-to-point fibre path computation. Copyright Wiley. Adapted from Ref. [199].

The jet lag control becomes even more complicated when multiple layers are printed. In the curved regions and corners, the fibre path changes from layer to layer [200], even when the jet lag is minimized by having collector speed close to the CTS [115]. In thick constructs

this effect can completely change the laydown pattern of the upper layers and therefore needs to be investigated and eliminated. At least partially, it might occur due to the difference between the jet speed and lag when it falls on the previously deposited fibres and is printed directly on the collector.

A potential way for calculation of a jet lag is a mathematical model. The jet lag of a viscous liquid, falling on a moving belt [108] has been successfully predicted by Ribe et. al. This governing model was extended to include the influence of the electrical field and applied for solution electrohydrodynamic printing [193]. Unfortunately, this model cannot be directly applied for MEW, due to profound differences in the jet geometry and mechanical properties of the material: The jet is much thicker and more viscous do that the resistance to bending cannot be neglected. The fact that mechanical properties and charge distribution along the length of the jet are changing through cross-section decrease, heat and charge dissipation through the air and collector surface must be taken into account, while creating a physics-based model of a MEW printing process. Whereas much work has been performed on modelling melt electrospinning [96, 98] and other types of electrohydrodynamic printing [201-206], those studies have been concentrating on the initiation and stability of a diameter change in the non-coiling region of the electrified jet, jet buckling and motionless printing. A recent study on modelling of the jet, falling on a moving collector, with differential equations [207], that is based on a previous research of the fluid mechanical sewing machine [109] could be a starting point in development of a consistent physical model, however, at this stage it is limited to the jet shape prediction at a constant collector speed. Therefore, up to now, none of the mathematical models of the MEW-related technologies were able to predict the result of a 3D scaffold or even a 2D pattern. Instead, in this Chapter a simple geometrical model (Figure 6.1E) is proposed that uses empirical equations for jet length calculation [199].

6.2 Materials and methods

MEW setup: Printing was performed on a MEW printer, described in the literature [182]. The standard printing parameters for the model validation were 87°C set polymer temperature, 1.2 bar air pressure, 22G nozzle, 3.5±0.1 mm collector distance, -1.5 kV collector voltage and +5.75 kV nozzle voltage. The samples were printed on 1.1 mm thick glass slides (VWR Inc., China), put on a stainless-steel collector. Polycaprolactone (Purac PCL PC12, Corbion, The Netherlands) was used as a polymer for printing. Due to the observation that jet

speed can vary, depending on the environmental conditions and the position on the collector, CTS was measured, as previously described (Chapter 3) before each print and this measured value was used to calculate the actual speed ratio. Prints for Figures 6.1A and 6.7C were made under the conditions, specified in Chapter 4.

Jet imaging and lag measurement: The jet was imaged by a Sony Alpha 7 digital camera with a Nikon ED 200 mm lens. Videos of the jet with 1080p resolution were taken at 50 frames/s. Stills were captured in Blackmagic Resolve 16 (Blackmagic Design, USA) and then analysed in ImageJ [208] to measure the distance between the JCP and the NP on the collector. Stable lag values were measured in the middle of a 50 mm path at collector speed equal to 1.125, 1.25, 1.5, 2, 5, 9, and 17×CTS. For the measurement of the JCP speed (V_{JCP}), the falling jet was filmed during both collector speed drop from 17×CTS to zero and collector speed transitions between 1.125 and 2, 2 and 5, 5 and 17×CTS. Lag values were measured starting from the movie frame, preceding the one, where the maximal lag decrease was observed. V_{JCP} values were calculated by adding the collector displacement relative to the nozzle to the difference between the current and the following lag (Figure 6.2) and dividing the result by the frame time (0.02 s). It must be noted that it was not possible to accurately determine the corresponding collector speed for each lag measurement point and the assumption was made that the speed decreases linearly over the deceleration time. Based on the measurement results, fit functions were chosen, and their coefficients were found in Matlab 2018R Curve fitting toolbox (MathWorks Inc., USA). To determine out how stable lag and V_{JCP} depend on the changes in selected processing parameters, pressure, nozzle voltage and collector distance were independently changed to 2.4 bar, 5.75 kV and 4 mm, respectively.

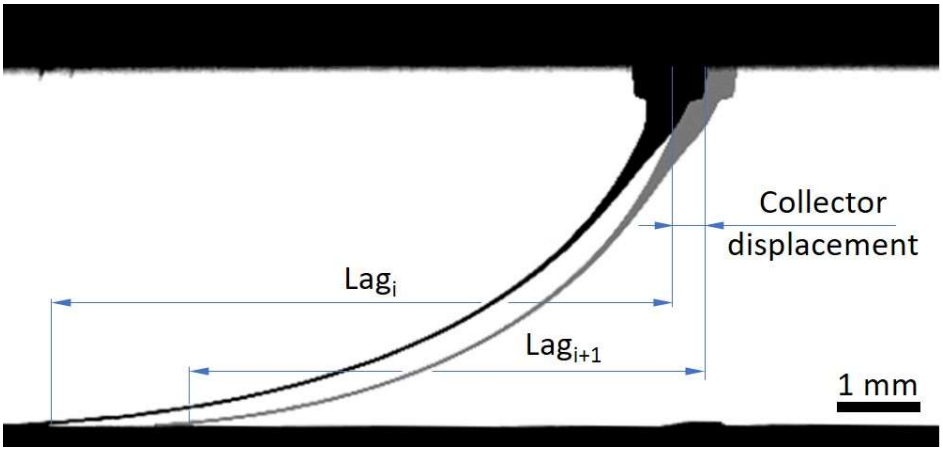

Figure 6.2. Jet lag measurement scheme. Copyright Wiley. Adapted from Ref. [199].

Model implementation and validation: The path prediction model was developed in collaboration with Dr. I. Liashenko and implemented, utilizing Matlab 2018R and "curvspace" function [209]. The validation of the model under the standard printing settings was done with a set of primitives (squares and circles with three different sizes: 2, 4, 6 mm and two sinusoidal lines with the same wavelength (1 mm) and two different amplitudes (0.75 and 1.5 mm) (Figure 6.5B), using five collector speed values: 1,125, 1.25, 1.5, 2 and 3×CTS. The predictive ability for multiple layer structures was assessed for the same pattern at the 1.5×CTS collector speed for samples with eight fibre layers. The imaging of the printed fibre patterns was made with a stereomicroscope (Discovery V20, Carl Zeiss Microscopy GmbH, Germany) in a polarized light, processed by an ImageJ Skeletonize plugin [210] and analysed in MATLAB 2018R.

The ability of the model to predict fibre diameters was examined with single layer samples printed at 2×CTS. A series of SEM images in selected points of a 2 mm loop and sinusoidal lines (Figure 6.8D) were taken with a Crossbeam 340 SEM (Carl Zeiss Microscopy GmbH, Germany) and analysed in ImageJ.

Statistical analysis. For all experiments n=7 independent prints were analysed. Data is presented as mean ± standard deviation. A t-test and one-way ANOVA with Tukey post-hoc correction was done to prove the significant difference of the results ($p<0.05$).

6.3 Results and discussion

6.3.1 Geometrical model development

The developed ready-to-use geometrical model utilizes a programmed path, collector speed and CTS, i.e., either pre-set or easily measurable process characteristics as input parameters.

For the computation of a printed laydown pattern, the given G-coded path is divided into a sequence of nozzle positions in the collector plane (represented by NPs). Those points are connected by unit movement vectors (Figure 6.1E). The distance between the points is proportional to the collector speed. Currently, the model neglects the stage acceleration limits and can either distribute them equally (movement with a constant speed) or stack the point coordinates in order to simulate a full stop of a certain duration. The transition between two adjacent points takes the same unit movement time (Δt). The resolution of the points on the

collector path can be set and should be picked considering the expected model accuracy and the smallest pattern feature size.

The calculation of the location of the next point, where a fibre lands, JCP_{i+1} requires the knowledge of previous positions on the nozzle (NP_i) and the fibre (JCP_i). The vector between those point is the current lag ($\boldsymbol{L}_i$). For a sufficiently small unit collector movement, it is justified to assume that JCP_{i+1} will be positioned on a vector pointing from the JCP_i towards the NP_{i+1}, termed as ray. It is equal to the vector sum of the $\boldsymbol{L}_i$ and unit collector movement vector (Figure 6.1E). When all four mentioned points are collinear (constant linear motion of the collector), the length of a ray (Ray_{i-4} in Figure 6.1E) is maximal for the given collector speed. Any collector movement direction change decreases the length of the ray. In other words, the collector is moving away from the jet contact point slower. To quantify this decrease, a moving away speed (V_{MA}) is introduced, a parameter that shows the instant speed of the nozzle relative to the JCP_i and, thus, affects the tension in the jet and thereby the lag length L_{i+1}.:

$$V_{MA}^{i+1} = \frac{Ray_{i+1} - Lag_i}{\Delta t}. \quad (6.1)$$

The new lag length L_{i+1} is then predicted from the V_{MA} value and the previous length L_i according to the algorithm, presented in Figure 6.3. First, V_{MA} is divided by the CTS to obtain the speed ratio (*SR*) to find if the collector is sufficiently stretching the jet for a lag to appear. For each SR>1 exists a lag, which is reached when the collector is moving linearly at a constant speed for enough time for a jet to stabilize. This characteristic value is called a stable lag (L_{stable}). An empirical function $L_{stable} = f(V_{MA})$ can be found, which is, however, unique for each set of printing parameters. A situation when SR≤1 means that the jet approaches the vertical state ($L_{stable} = 0$).

In both abovementioned cases ($L_{stable} = 0$ and $L_{stable} \geq 0$), there is a possibility that the jet cannot reach those values instantaneously within one iteration. This happens because the jet contact point speed (V_{JCP}) cannot be indefinitely high to reach the JCP_{i+1} when $Ray_{i+1} >> L_{stable}^{i+1}$. To enable jet lag calculation in those cases the V_{JCP} must be calculated with a function, connecting V_{JCP} and the L_{i+1}. With this speed the JCP_{i+1} is moving away from the JCP_i Several geometrical limitations, are to be additionally applied: The new jet length cannot not exceed the ray length, i.e., JCP_{i+1} cannot move away from the NCP_{i+1}. In general, once the lag is above

zero, JCP must be approaching the nozzle since the viscoelastic jet is constantly being elongated under the tension and falls on the collector. Thus, the new lag value L_{i+1} can either take the L_{stable} value, be calculated through V_{JCP} or be equal to zero.

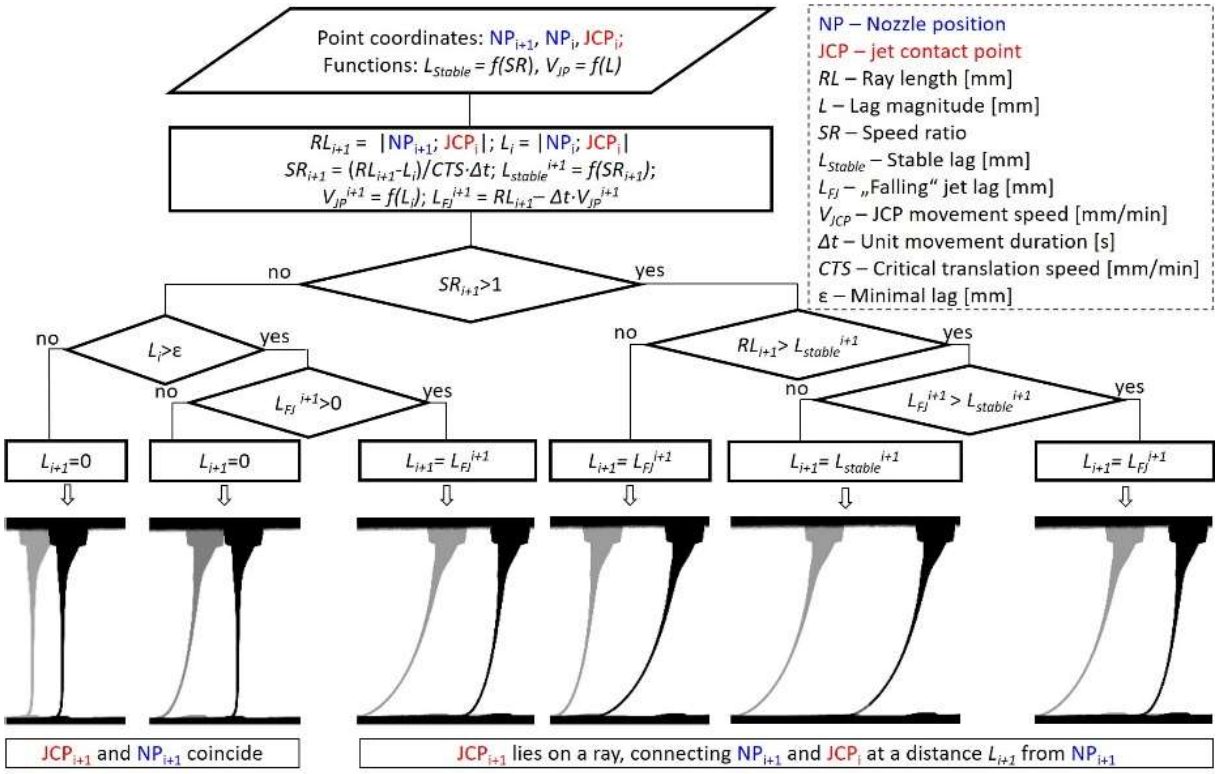

Figure 6.3. Algorithm of a lag computation with schematic illustrations of the jet shape transition based on jet photo images. The jet images corresponding to L_i and L_{i+1}, are shown in grey and black, respectively. For the illustrative purposes, the nozzle is shown to be moving instead of the collector. Copyright Wiley. Adapted from Ref. [199].

6.3.2 Jet lag and contact point speed measurement

In agreement with the literature [143], a faster collector speed resulted in increased L_{stable} values. This dependence is not linear, and the growth is very steep up 6×CTS but slows down with the speed ratio increase. This observation supports the claim that using CTS as a printing speed isn't optimal: Even a small CTS measurement error or a change in processing parameters, which affects the jet speed might either increase the lag, causing a significant error or bring the jet into the coiling mode (Figure 6.4A, B). On some of the lag measurement videos a jet that was exceeding its characteristic stable lag values was detected while accelerating from steady state to a speed, higher or equal to 6×CTS. This observation was neglected in the model, since the scenario was not covered by the validation prints, but, in

theory, this effect can cause worse prediction quality of patterns, printed at faster collector speeds.

Based on the datapoint distribution, a power function of the type $a - a \cdot x^b$ was selected for calculation. It requires the variation of just two coefficients and provides a sufficient quality of fit in the tested speed ratio range (adjusted R^2 = 0.9811) but implies the existence of a maximal possible lag value, equal to *a* coefficient, which is not necessarily true. For the standard printing conditions the fit equation was:

$$L_{stable} = 10.02 \cdot (1 - SR^{-0.304}), \quad (6.2)$$

where *SR* stands for speed ratio.

The reverse statement, that for every lag magnitude *L* exists a corresponding speed ratio can be used for V_{JCP} calculation:

$$V_{JCP} = CTS \cdot (1 - L/10.02)^{\frac{1}{-0,304}}. \quad (6.3)$$

The V_{JCP} values, calculated with the Equation 6.3 are called derived V_{JCP}. Thus, distinction to the directly measured V_{JCP} values is made, obtained during the collector deceleration (Figure 6.4C). Initially the measured V_{JCP} are collected during the collector full stop from 17xCTS. They were adequately represented by the derived V_{JCP} only for small lag values (Figure 6.4C). When the lag was longer, the measured V_{JCP} was higher than the derived up to 5.5 mm. The V_{JCP}, measured when the speed was decreasing to a non-zero value (from 17 to 5, 5 to 2 and 2 to 1.25×CTS), were different from the full stop ones and better fit by the derived V_{JCP} curve (Figure 6.4D). This situation should better represent the jet behaviour during printing and, therefore, the derived V_{JCP} Equation 6.3 was implemented into the model. The utilization of this equation additionally minimizes the amount of the input data. It is possible however that an empirical fit to the full stop V_{JCP} data would be more applicable for certain patterns, consisting of straight lines and pauses between them. The difference the V_{JCP} measurements is likely related to the transition speed values and the acceleration of the stage. Potentially, an equation needs to be found for a better V_{JCP} prediction, considering all possible V_{JCP} instant collector speed and acceleration values.

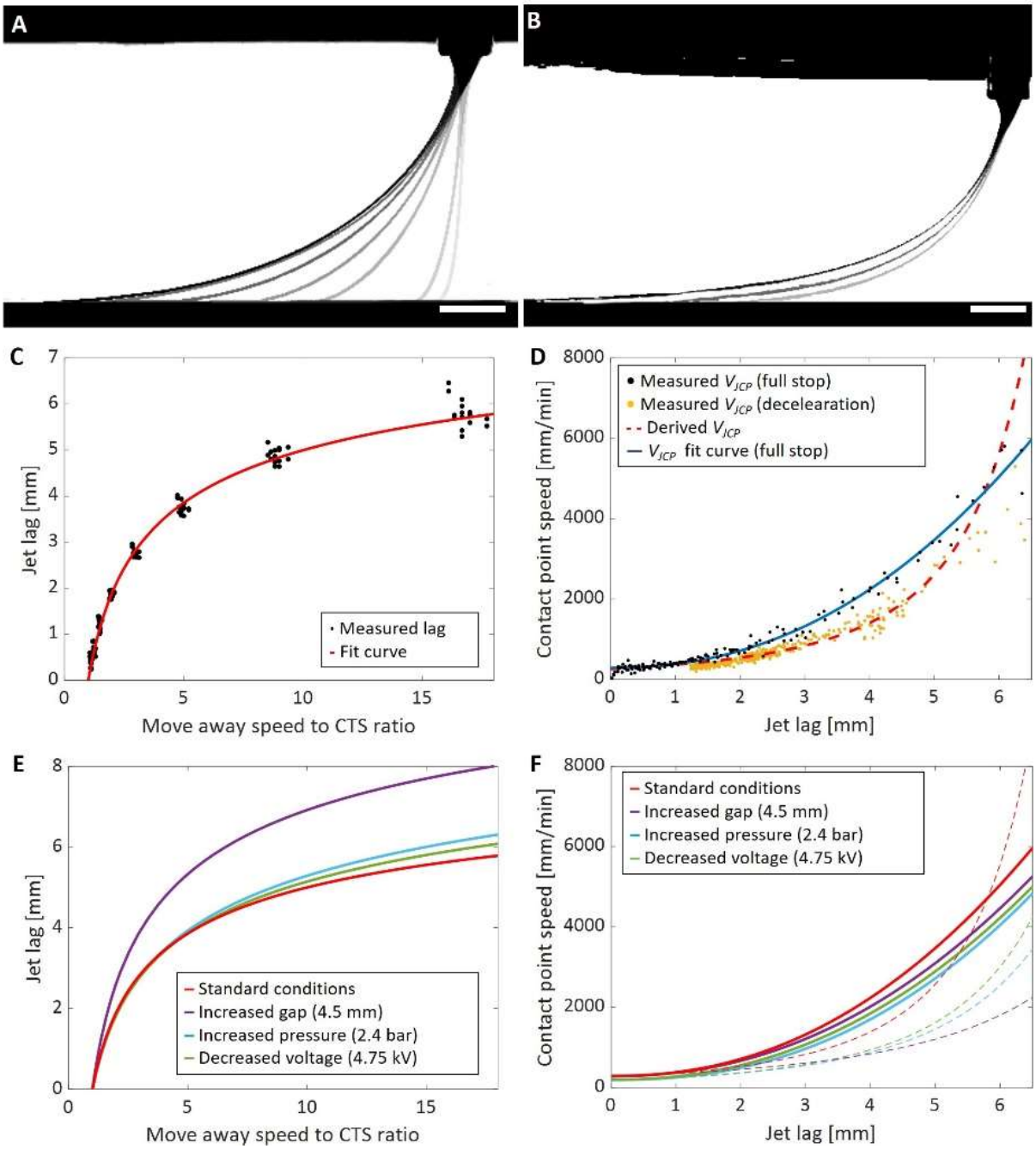

Figure 6.4. A: Stacked images of a stable jet at the collector speed varying from 17×CTS (leftmost) to 1.125×CTS (rightmost). Applied pressure – 2 bar. B: Stacked images of a jet undergoing a shape transition while collector speed is decreasing from 17×CTS (black) to 5×CTS (light grey), taken at 0.04 s intervals. Standard printing settings. C: Measured stable lag at standard conditions with a fit curve. D: Comparison of a V_{JCP} calculated from the stable lag fit function (Derived V_{JCP}) and experimentally measured values. E: Influence of the process parameters on the fit curves of the stable lag. F: Comparison of the fit curves (solid lines), built for the measured V_{JCP} (collector undergoing full stop) and derived V_{JCP} (dashed lines) for varying processing conditions. Scale bars 1 mm. A, C and E: Copyright Wiley. Adapted from Ref. [199].

For different equipment configurations and scaffold morphologies optimal parameter sets must be found by trial and error. Due to this variation in the printing conditions, it is necessary to check if Equations 6.2 and 6.3 are universally applicable. As shown in Figure 6.4E, only the increased collector distance caused significant lag increase along the tested speed ratio range.

Although the V_{JCP} fit curves, calculated for the full stop data look like each other (Figure 6.4F), the derived V_{JCP} curves have a larger deviation from the corresponding fit curves and between each other. The differences in the V_{JCP} although are partially caused by the difference in corresponding CTS values (Table 6.1). Nevertheless, the same type of function could be fit to the data by changing the numerical coefficients. Thus, despite the inability of original equations 2 and 3 to be directly utilized in a prediction model for arbitrary MEW setup, the model can be used after the appropriate coefficient adjustment.

Table 6.1. Influence of process parameters on the critical translation speed (CTS).

	Printing settings			
	Standard	2.4 bar	4.5 mm	4.75 kV
CTS [mm/min]	257.1±14.7	170.0±5.8	273.6±5.6	175.7±3.4

6.3.3 Model validation

For its mathematical simplicity, the proposed geometrical model provides a remarkable quality of fibre layout prediction. Regardless of the printed shape and the collector speed the mean deviation of the predicted pattern from the printed fibre lies below 0.071 mm, which is more than 5 times more precise than the programmed path provides. A similar same ratio is valid for the maximal error, while less than 0.2 mm maximal deviation from the predicted path is compared to more than 1.5 mm distance between the programmed and printed fibres (Figure 6.5A-D). Those maxima correspond to the corners of the square. The mean error calculated for the whole test pattern does not change with the increase of the collector speed despite of a slight, but statistically significant growth of the maximal error. The mean distance between the programmed and printed patterns on the contrary is nearly linearly growing with the collector speed and exceeds the maximal error of the model already

at 1.5×CTS. The maximal error of the G-coded path is always higher than the corresponding prediction error.

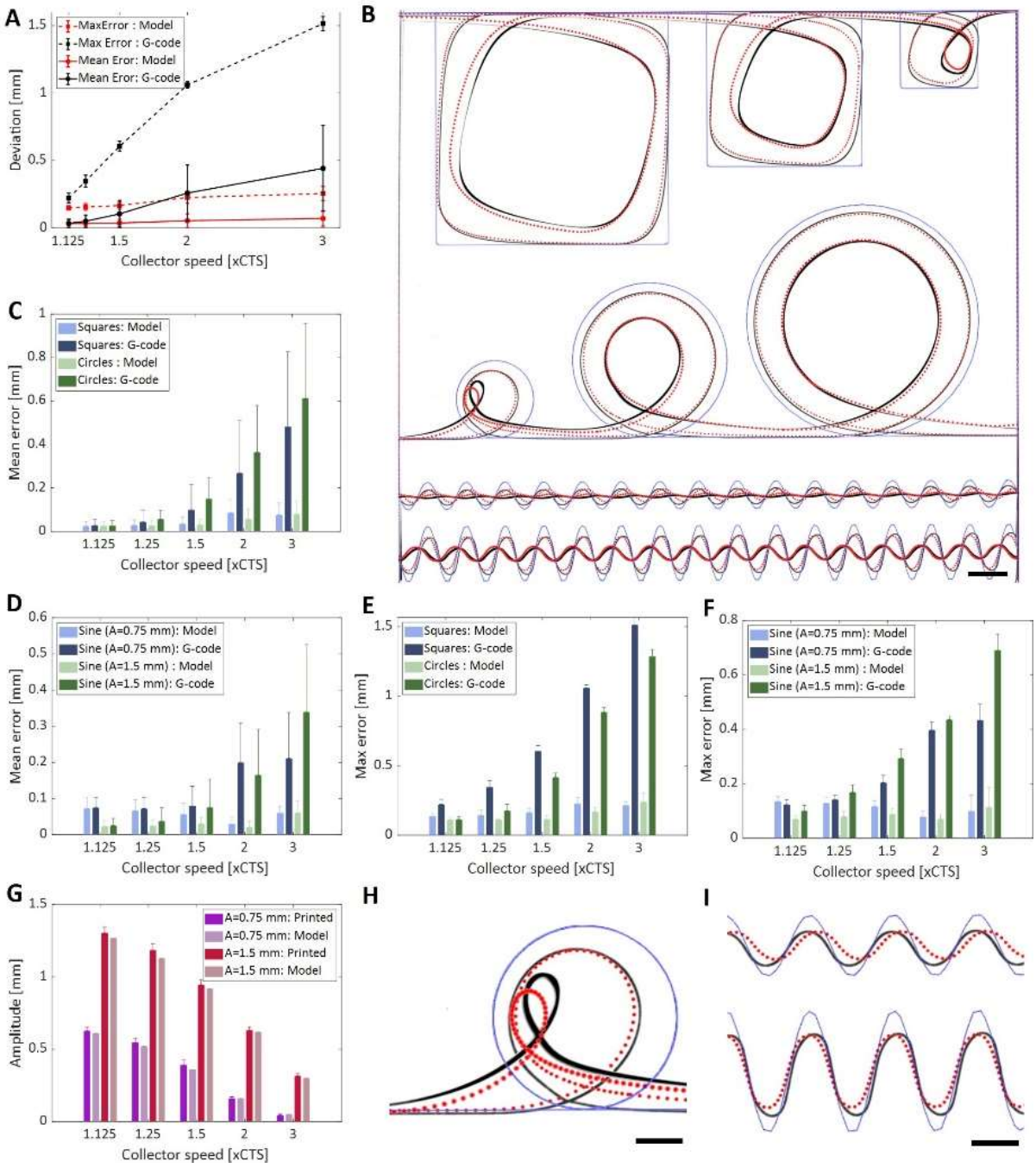

Figure 6.5. A: Mean and maximal deviation of the predicted pattern (red) and programmed path (black) from the actual printed fibre for all tested shapes. B: Image overlay of the predicted path (red dots), programmed path (blue line) and printed pattern (black lines) at 1.5×CTS and 3×CTS. C-F: Comparison of the mean and maximal errors, sorted by printed shape. G: Comparison of the printed and predicted sine line amplitudes. H, I: Magnified fragments of B with a 2 mm loop and sine lines (1.5×CTS only). Scale bar 1 mm for B and 0.5 mm for H and I. Copyright Wiley. Adapted from Ref. [199].

The predicted path, generated by the model was beneficial for all tested shapes, although for the sinusoidal lines the calculation error was higher, compared to the circles and squares. At a collector speed below or equal to 1.5×CTS, the average error between the predicted and printed sinusoidal lines was comparable to the error between the printed path and the G-code. When the maximal error is considered important, the model result can be helpful already at 1.25×CTS. Despite this result, the fact that the amplitude and the wavelength of the sinusoidal lines were calculated correctly (no significant difference between the calculated and measured values, Figure 6.5G) makes the model particularly useful for such periodical curves.

As with several other test pattern fragments, the error here was mostly caused by a position shift (Figure 6.5H, I), partially resulting from image aberrations from microscopy. Prediction quality demonstrated here, however, is representative only for the first layer and while using a flat collector. As shown in previous Chapters, printing on top of previously deposited structures or a non-planar collector [89] will affect the laydown pattern. This layer-by-layer pattern change depends on the printing parameters and the pattern shape [194].

The pattern shape changes described in Chapter 5, occurring with the growth of the build height (e.g., decrease of the sine line amplitude) can be, among other factors, caused by an increased jet lag. This could be confirmed by the jet lag measurements when the fibre is printed on top of eight vertically stacked fibres (178.15±2.78 µm total height) (Figure 6.6A) where these lag values cannot be represented by the Equation 6.2: The lag was growing steeper in the low *SR* values range but after the *SR*>2 the lag was smaller than it would have been, during printing directly on the collector surface. Simultaneously, the CTS is decreasing with the build height (Figure 6.6B). When the updated CTS values are substituted into the Equation 6.2, the lag curve can be used to represent its values only for low *SR* (<2).

Although the results of the Chapter 5 indirectly suggest that the application of the uniform linear printing parameter correction might not work for all printing patterns, initially it was considered possible to adjust the input parameters of the model (CTS and coefficients of the Equations 6.2 and 6.3 with each printed layer in order to achieve a prediction quality comparable to the first layer results. While the updated CTS can be readily obtained, coefficient correction is a procedure that requires a collection of large amounts of data.

Therefore, it was decided to use the original fitted function for lag computation (Equation 6.2) and limit the printing speed by *SR*=1.5.

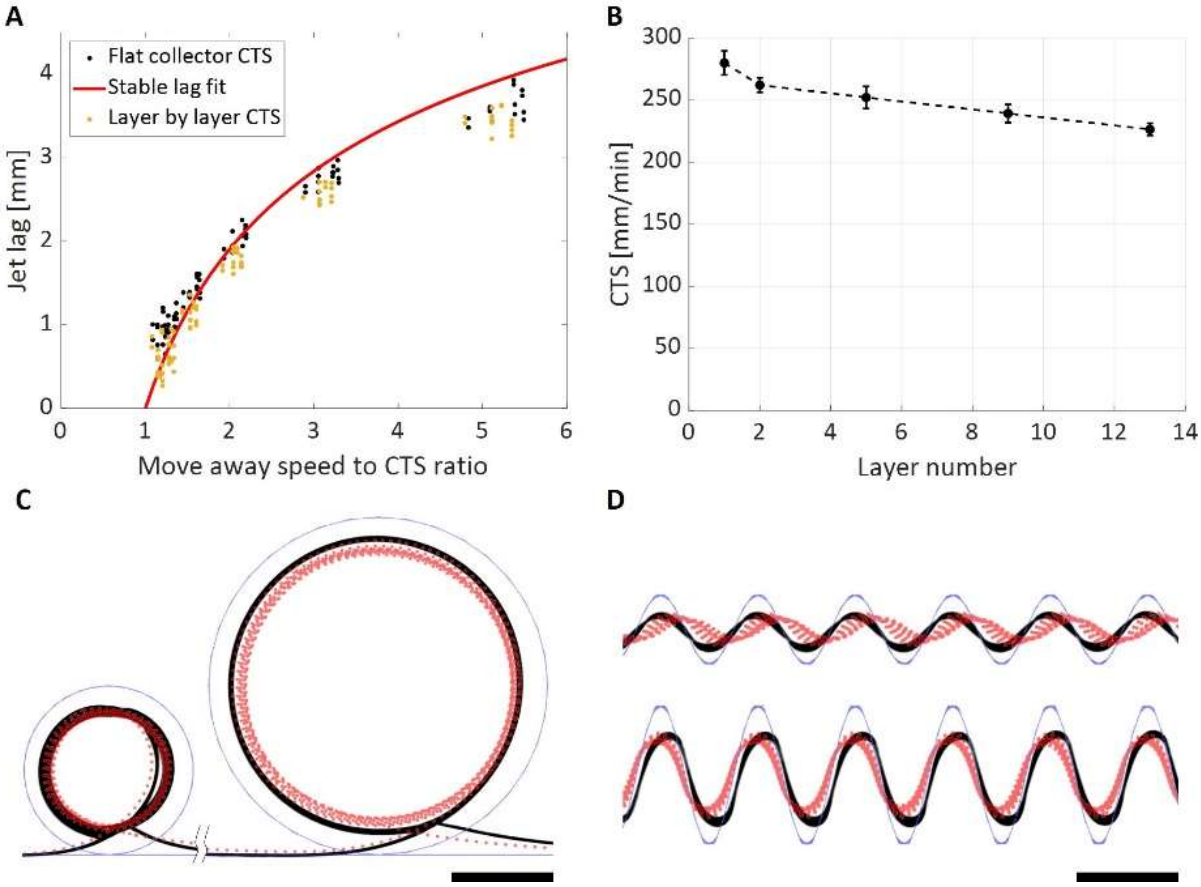

Figure 6.6. A, B: Influence of the construct height on the lag and critical translation speed, respectively. C, D: Image overlay of printed (black line) circular and sinusoidal test patterns with eight stacked fibre layers and predicted fibre position (red). Scale bars 1 mm. Copyright Wiley. Adapted from Ref. [199].

A power function was fit to the points on the graph in Figure 6.6B and the calculated CTS values for each layer were used in the model. Comparing the calculated path with the printed fibres for eight layers pattern (Figure 6.6C, D), a clear difference can be seen on most of the test shapes. Although the shape of the fibre walls cannot be precisely predicted by this approach, in the path segments with the furthest deviation of the predicted fibres of the upper layers from the programmed path a greater tilt can be expected and even the detachment of the fibre from the wall (Chapter 5). Since the model does not consider the electrostatic attraction and the mechanical properties of the fibres, it was not expected that the prediction of the multiple layers pattern would be accurate.

The complexity of the multilayer pattern prediction task can be further emphasized by several phenomena (Figure 6.7). When a fibre was deposited on top of the wall and the collector speed was approaching CTS a 'negative' lag (Figure 6.7A, left panel) was appearing. The transition below the CTS is not manifested by a typical meandering pattern but rather by a periodical increase of a negative lag, up to a certain value after which a formation of a sidekick was following (Figure 6.7A, B). Furthermore, when the sizes if the fibres in the wall and the newly deposited fibres differ, more complicated shapes can appear (Figure 6.7C). While those effects can be potentially utilized to place fibres in a virtually arbitrary way [194], the mathematical description of the deposition process is highly complex and lies beyond the scope of this study.

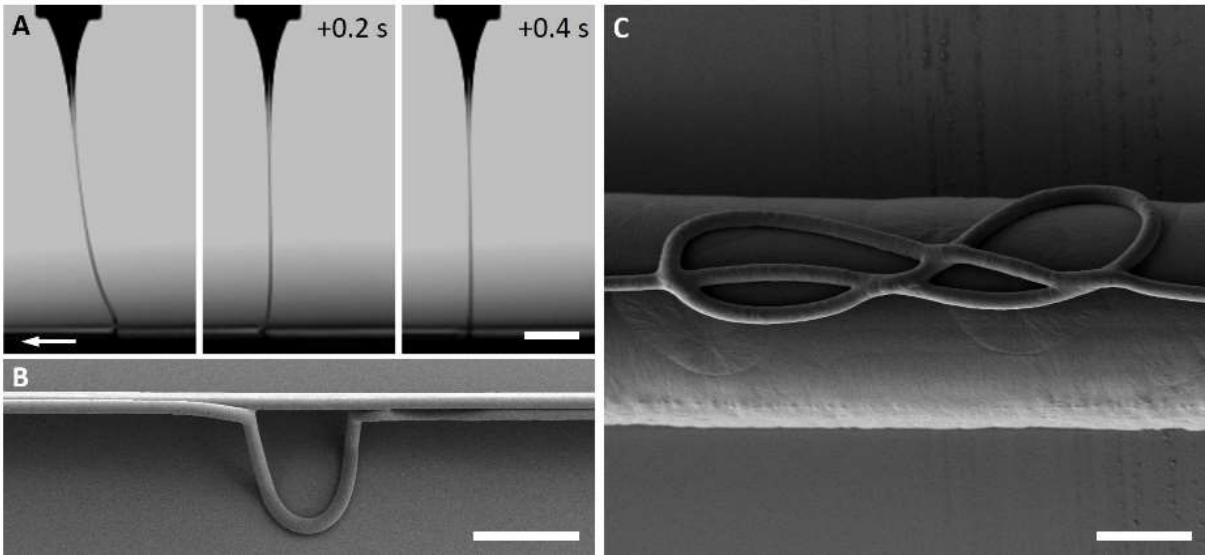

Figure 6.7. A: Video screenshots of a jet with a negative lag in the heel region. The accumulated jet length is periodically released in the form of sidekicks. B: A corresponding SEM image of the print, shown above. C: Deposition of a thinner fibre, printed below CTS on a top of a thicker fibre. Scale bars 500, 200 and 20 µm for A, B and C, respectively.

As it was described in Chapter 4, collector speed is a process parameter, that allows quick adjustment of fibre diameter. This transition, however, cannot be considered instant (Figure 6.4B). When the speed is increasing, the tension along the whole jet catenary length is increased. The decrease in the diameter along the length of the jet is deemed to be uneven due diameter and temperature gradient and viscoelasticity of the jet. In case of a rapid deceleration, a segment of a catenary is likely to 'fall' on the collector, maintaining its

gradually decreasing diameter. In both cases, the diameter changing rate distinctly depends on the start and the end speed (Figure 6.8A).

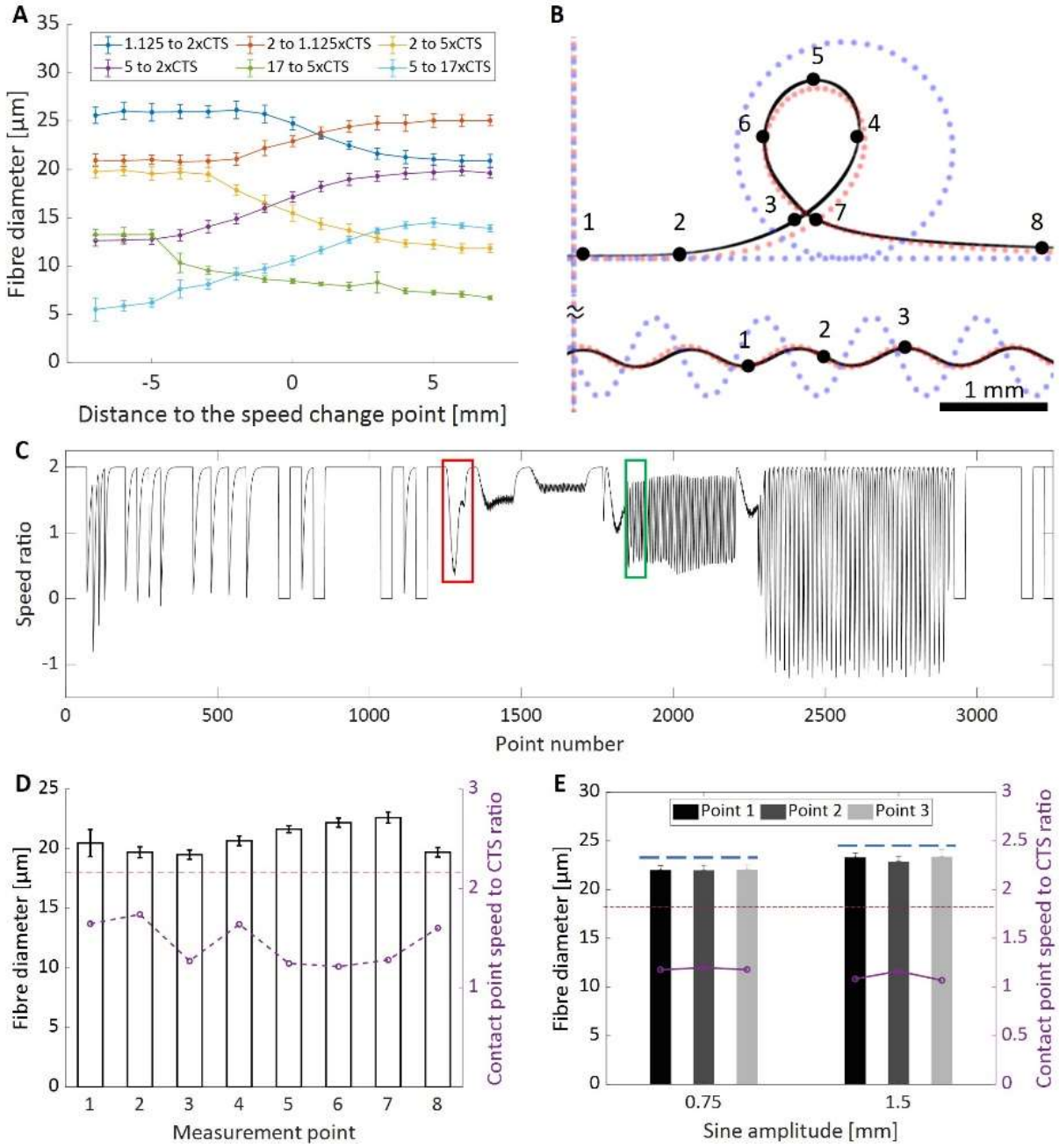

Figure 6.8. A: Fibre diameter behaviour during collector acceleration and deceleration. B: Image overlay of the printed, predicted, and programmed pattern, in the region where fibre diameter was measured in the indicated points. C: Speed ratio change along the predicted path. Red and green frames highlight the path segments with the loop and sine line from B, respectively. D, E: Fibre diameter measurements compared to the average value at the set collector speed (red line) and predicted values, based on the calculated contact point speed (blue line). B, D and E: Copyright Wiley. Adapted from Ref. [199].

Repetitive V_{MA} change during the printing of non-linear patterns (Figure 6.8B, C) does not allow to use the Equation 4.2 for the diameter calculations, since it is only applicable when the lag is stable. Moreover, for the negative V_{MA} values (Figure 6.8C), which can occur when the collector is rapidly changing direction lag calculation is nonsensical. Instead, the V_{JCP} can be utilized, which is, by definition, always positive. Although, due to the reasons mentioned above a direct and accurate diameter calculation is not possible, a qualitative assessment of a fibre diameters distribution along the path can be made, based on those values: After a predicted segment with low V_{JCP}, an increase in diameter should be expected (Figure 6.8D).

There are two situations, when a fibre diameter in a pattern can be predicted with higher reliability: In addition to the regions where the lag is stable, (constant V_{JCP} or V_{MA}), averaged V_{JCP} or V_{MA} can be substituted into the respective equation (Chapter 4) for the regions of the pattern, where those characteristics are quickly oscillating (Figure 6.8C). The fibre diameter of the sinusoidal did not depend on the position on the fibre. As predicted by the calculation, it was thicker for the sine line with larger amplitude exceeded the characteristic value for 2×CTS (18.03±0.97 µm). The predicted values were, however, higher than the actual ones for both amplitudes (Figure 6.8E).

An increase in prediction accuracy can be expected when a smaller collector distance is applied [151] and while other processing conditions make the jet speed higher, i.e. the length of the jet is smaller. Yet, whether those conditions could make the precise diameter calculation feasible for the segments with non-periodical speed ratio changes needs further investigation. In a study by Jin et. al. [137] a principle of diameter prediction, based on jet lag measurement was been announced, yet no details on the calculation algorithm were presented.

6.3.4 General implications for scaffold printing

Measurements of the jet lag at collector speed, close to the CTS and the quantification of the model validation results added further concerns to the improvement of MEW predictability by the decrease of collector speed. Even at 1.125×CTS distance between the programmed path and the printed fibre cannot be ignored. A further decrease of the collector speed brings a risk of a transition into the coiling mode: The CTS between the print and even during the print can vary due to fluctuations in the environmental conditions and process

parameters such as ambient temperature or collector flatness. Unless the entire programmed path consists of smooth curves, there must exist points where the collector speed would decrease below the given values because of the axis acceleration limits. In the vicinity of those points coiling can appear as well. Those acceleration limits are not considered by the model as well and are partially responsible for the prediction error.

A different way to make the printed laydown pattern closer to the programmed one is to locally decrease the collector speed or even introduce pauses in the movement in the point, where the deviation would be maximal otherwise (e.g., in the corners) [52]. This approach requires additional experiments to determine the optimal magnitude of speed reduction and pause duration, sufficient for the desired local lag decrease. In addition, local speed decrease will cause even greater diameter variation in the pattern than is naturally caused by V_{MA} variation from direction change alone. Here the described model can potentially replace the experiments for pause or decreased speed determination.

Currently, the laydown pattern prediction model cannot be applied universally to any MEW printing setup and requires the preliminary CTS measurement as well as coefficient correction for the Equations 6.2 and 6.3. Optical lag measurements for this purpose can potentially be replaced by an analysis of standard printed shapes, this procedure however requires further development and validation. Ideally, the jet length should be calculated by a physical model instead of an empirical one. With the recent progress in such models [207], an accurate prediction of a fibre diameter should be possible as well as better translation of the model to stacked fibre walls and, potentially, whole scaffolds.

Chapter 7: Control of dorsal root ganglia neurite growth in MEW scaffolds through pore interconnections

7.1 Introduction

Having established the limitations and boundaries of MEW printing parameters and printing approaches, this Chapter focuses on applying these outcomes into advanced cell culture systems, containing an additional element – suspended fibres (SF) and uses fibres with different predefined diameters and deposition patterns in one scaffold.

Fibrous scaffolds are widely used in neural TE as potential implants and research models, due to their inherent guidance properties [211]. Topographical cues have a deep impact on the cell morphology and motility in general [212, 213] and for the neural tissue in particular, where cell location and orientation are of a primary importance. For the study of neuronal and glia behaviour, micro- and nanofibre-patterned 2D substrates are a choice that has potential to be translated into 3D constructs. Indeed, 2D- and 3D fibre arrays have been used for fundamental studies of glia [214, 215] and neuronal behaviour [216, 217]. They can also be integrated into artificial nerve guides [218, 219] for peripheral nerve repair as well as scaffolds, assisting the guidance of cells during spinal cord regeneration [220].

In many instances, the fibres for such substrates and were obtained by electrospinning, due to the strict requirements to the fibre diameter, which should both fit the topographical and mechanical needs of the cells. As previously mentioned in Chapter 1, the use of electrospinning doesn't allow precisely controlled fibre placement in 2D and, especially, 3D, which can be only partially overcome by advanced electrical field control [159] and, for instance, stacking of multiple fibre layer sheets [221, 222].

Several research groups have been investigating the influence of the MEW scaffold pore shape and fibre diameter on the cell orientation [141, 151, 153]. In neural TE, MEW scaffolds have been finding an increasing demand mainly due to a high porosity of MEW scaffolds [114] and their ability to provide a structural support to weak matrices [190, 223]. The guiding ability of MEW fibres for neural model cell line has been recently demonstrated for PC12 cells [56], implying artificial nerve guides as a potential application.

An additional benefit of MEW for neural TE is the mentioned in Chapter 4 ability of MEW to incorporate SFs into a scaffold (Figure 7.1). Under certain processing conditions [224] it is possible to suspend the fibres between the supports, which also can be printed by MEW, at different heights. The attraction force to the collector and underlying fibres is counteracted

by an increased the tension in the jet, achieved by high collector speed and higher jet viscosity due to low printing temperatures (unpublished data). Further printing on top of those SFs allows building of overhanging structures in different directions, thus changing the predominant cell orientation between the layers within one scaffold [191].

Due to a further increased porosity of such scaffolds and reduced amount of fibre interconnections, holding the scaffold together, mechanical integrity of those scaffolds under cell culture handling conditions was an open question. It required an investigation of processing temperature and collector speed as factors, potentially influencing the fusion between the deposited fibres.

In this Chapter it is demonstrated how designed fibre arrays and pore interconnections in MEW scaffolds affect the supporting cell (including Schwann cells and fibroblasts) spreading and neurite growth of embryonic chick dorsal root ganglia (DRG). Combining the idea of topographical neurite guidance with a full control over the pore interconnectivity, granted by SFs, novel MEW scaffold architectures were developed. The potential of those scaffolds to be utilized as a model for controllable 3D environment for neural TE is discussed.

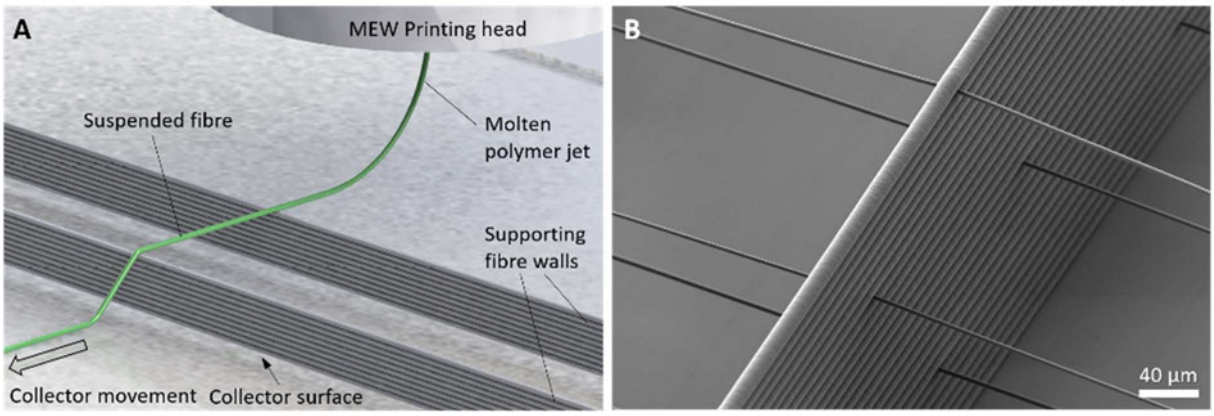

Figure 7.1. Suspended fibres (SF) in MEW. A: A principle of direct writing of SF in MEW. B: SEM image of a SF array.

7.2 Experimental section

Scaffold printing: Scaffolds with adjustable pore interconnectivity were produced on a custom-made MEW printer, described in Ref. [134] while the structures with SF arrays were printed on a near-identical printer but with a motor-driven Z-axis. The polymer (PCL, Purac Purasorb PC12, Corbion Netherlands) was extruded though a 22G nozzle (Nordson EFD, USA) and deposited on 1.1 mm glass slides (VWR Inc., China).

Table 7.1. Printing settings for scaffolds with suspended structures (CD – collector distance).

#	Heater temp. [°C]	CD [mm]	Collector/Nozzle Voltage [kV]	Air temp. [°C], ±2	Relative humidity [%], ±5	Collector speed [mm/min]	Pressure [bar]
1	75	2	-1,5/+2.5	20	40	5000-10000	0.7
2	77	3.5	-1,5/+4.5	20	40	1500	0.8
3	90	6	-1,5/+7.5	20	40	200	2

Printing of the parallel fibre arrays was done under the condition set #1 from the Table 7.1. The speed was linearly decreasing from 10000 mm/min to 5000 mm/min with the increasing height of the scaffold in order to minimize the jet lag effect on the fibre positioning (Chapter 6), while maintaining the fibre suspension. The supporting walls were printed at a significantly lower speed of 200 mm/min. Parameter set #2 was applied for the printing of scaffolds with adjustable pore interconnectivity. Different conditions were applied for the printing of a reinforcement circular frame around the central part of the scaffold (parameter set #3) to improve fibre fusion with the previously deposited SFs and supporting walls for a better mechanical support. Actual temperature inside the syringe was 12±1°C lower than the one set with the temperature controller.

DRG extraction and tissue culture: E10 and E11 chicken embryos were kindly provided by Dr. J. Gerardo-Nava. DRGs were extracted from the embryo's spinal cords, manually cleaned from the surrounding tissue, and placed into the pores of the scaffold. For the extraction, the embryos were decapitated, and relocated into a petri dish with a cold medium. After evisceration, the vertebral column was removed and exposed DRG's, primarily from lumbar and thoracic areas were collected. Detailed description of the surgical procedure is provided in the literature [221].

Prior to DRG seeding, scaffolds were sterilized either for 5 min in 100% ethanol, washed in sterile PBS and left to dry for 30 min under the UV light. Sterilized scaffolds were washed 2×5 mins in Hanks balanced salt solution (HBSS, Life Technologies, Germany), precoated with poly-L-lysine (Merck, Germany, 100 µg/ml in sterile MilliQ water, 30 mins), washed again in sterile MilliQ water and coated with laminin (Merck, Germany), incubating

them for 1h in 10 µg/ml solution in HBSS. Depending on the availability, 1 to 5 DRGs were seeded onto a single scaffold. 2 ml of cell culture medium (DMEM with 1% Glutamax (Invitrogen, Germany), 10% FCS (Capricorn Scientific, Germany) and 1% penicillin/streptomycin/fungizone Thermo Fischer, Germany) was added per well, which was changed every 3-4 days. For chick DRG in total, five extractions were performed, and, for each scaffold type, three to four samples were seeded. Scaffolds with controlled pore interconnectivity and chick DRG were removed for SEM, 3,3'-Diaminobenzidine (DAB) and immunofluorescent (IF) staining after three, six and seven days. After removal from the culture medium the scaffolds were fixated in 4% paraformaldehyde (IF and DAB staining) or 3.9% buffered glutaraldehyde. The protocol for SEM preparation is described in detail in Chapter 4. SF containing scaffolds with mouse DRG were fixated after 21 days *in vitro* in in cold 4% paraformaldehyde (AppliChem, Germany).

Immunocytochemistry: For DAB staining, samples were washed three times for 5 min in PBS with 0.5% Triton X-100 (PBS-T). Afterwards the endogenous peroxidase blocking (1% NaN_3 and 1% H_2O_2 in PBS-T) was applied for 10 min. After washing in PBS-T, a primary antibody (1:500, Anti-β-Tubulin III, produced in rabbit, Sigma, USA) solution in antibody diluent (1% Bovine serum albumin, 0.05% NaN_3 solution in PBS-T) was applied and left overnight. The 1:500 secondary biotinylated antibody (Goat-anti-rabbit, Vector, UK) solution in antibody diluent was applied for 1 h with 1% Normal rat serum (Abcam, USA). After 3×5 min wash in PBS, a 0.8% ABC kit (Vector, UK) solution in PBS-T was added and kept for 1h. Samples were washed in PBS and incubated in DAB solution for 5 min, containing 0.025% H_2O_2.

Before the start of the immunofluorescent staining: Scaffolds were washed in PBS three time and put into a blocking solution (5% skim milk powder (Merck, Germany) in antibody diluent for 1h. After the blocking was removed, a primary antibody (1:500, Anti-β-Tubulin III) and 1:100 Alexa Fluor 488 Phalloidin (Thermo Fisher Scientific Inc., USA) solutions in antibody diluent were applied overnight. On the next day, a 1:500 secondary biotinylated antibody (Goat-anti-rabbit, Vector, UK) solution in antibody diluent was applied for 1 h with 1% Normal rat serum (Abcam, USA), followed by a 1:250 solution of Cyanine3 conjugated streptavidin (Jackson, USA) and 1:1000 solution of DAPI in PBS, added for 1h after 3×5min wash in PBS.

A mouse DRG culture, staining and imaging experiments for the Figures 7.3E and F, using scaffolds with parallel fibre arrays were conceived and performed by Dr. G. Brook and Mr. P. Achenbach. Mouse DRG experimental procedures complied to Communities Council Directive 24 November 1986; 86/609/EEC and the RWTH Aachen ethics committee guidelines (code: 11525A4) aiming at minimization of the number of animals and their suffering. DRGs were removed from 12 C57BL/6N mouse pups (post-natal day 5-7, Charles River Laboratories, Germany) that had already been sacrificed for tissue dissection by another research group within the University Hospital Aachen, in the context of §4, section 3 of the German animal welfare act (killing of animals for scientific purposes). The dissected DRG were placed into sterile, cold HBSS with 6.2 mg/ml glucose. Scaffolds were sterilized in 70% ethanol for 30 min and coated by poly-L-lysine and laminin as described above. The DRG neurites were labelled with a combination of monoclonal antibodies: mouse anti-phosphorylated neurofilament 200 kDa (1:2000, Sigma-Aldrich, USA) and mouse anti-ß III tubulin (1:1000, Sigma-Aldrich, USA). Schwann cells were identified using polyclonal anti-S100ß (1:2000, DAKO, USA). After the overnight incubation, biotinylated goat anti-mouse or biotinylated goat anti-rabbit secondary antibodies (1:500, Vector, UK) were added, followed by washing in PBS-T and ABC kit application (Vector, UK) and a 5 min incubation in a 0.5mg/ml 3,3'-diaminobenzidine solution with 0.0003% H_2O_2.

Mechanical testing for fibre fusion: The force, required for fibre detachment was measured with an ElectroForce 5500 test instrument (TA Instruments, USA) by a 250 g load cell. The force was measured on a test sample (Figure 7.2), that allowed a mixed tension and shear loading of the fibre junctions, emulating the actual handling loads.

Microscopy: Fluorescent and light microscopy was performed on an Axioplan epifluorescence microscope, connected to an AxioVision CCD camera (Carl Zeiss Microscopy, Germany). Confocal microscope images were obtained on a DMI 6000B microscope (Leica Microsystems, Germany). Slice thickness for Z-stacks was set to 1 µm. Prior to the light microscopy, samples were immersed into 8:1 glycerol-PBS mixture. SEM imaging was performed with a Crossbeam340 electron microscope (Carl Zeiss Microscopy, Germany).

Statistical analysis: For the data presented as mean ± standard deviation n=7 samples were analysed and a two-way ANOVA with Tukey post-hoc correction was done to prove the significant difference of the results (p<0.05).

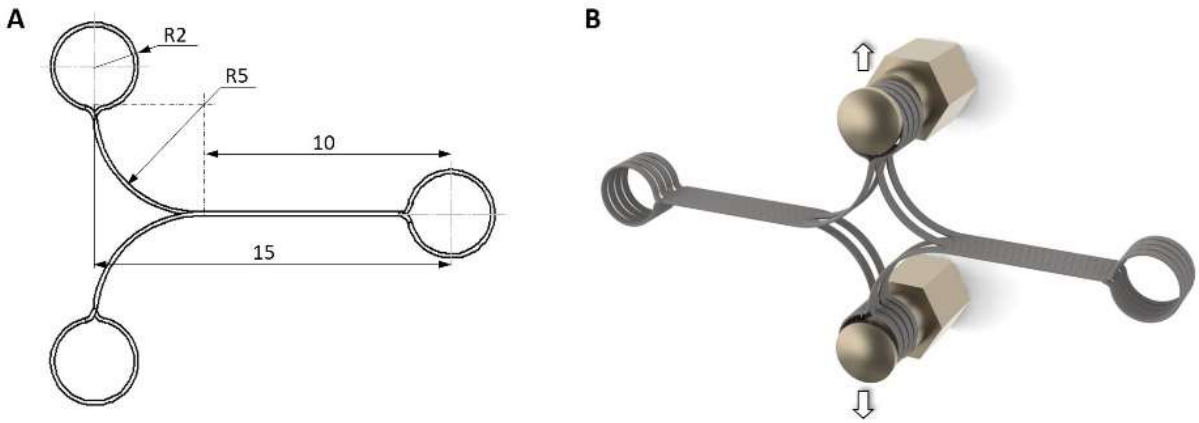

Figure 7.2. Mechanical testing setup. A: Top view schematic of a sample. B: A rendered schematic of a test setup with two samples simultaneously undergoing mechanical loading by cylindrical clamps.

7.3 Results and discussion

7.3.1 Scaffold printing

Printing of dense suspended membranes (Chapter 4) and defined single layer fibre arrays has been established previously (unpublished data beyond the scope of this thesis). In the latter case, similar to the fibre printing on the collector surface, MFS is limited and prevents accurately controlled orientation and density of the fibres, potentially decreasing the cell seeding efficiency. In addition, high printing speed, required for the fibre suspension increases the probability of the fibre misplacement (Figure 7.3A) due to large lag values (Chapter 6). An increase of SF density parallel with the Increase of amount of SF layers and scaffold height can lead to the loss of the intended fibre positioning pattern (Figure 7.3B). Nevertheless, it was found that a smaller fibre spacing can be achieved by locating the SF in a 'ladder' pattern [54], i.e. by having a large spacing between the fibres in the same layer (hundreds of µm) and adding an offset (tens of µm) between the layers (Figure 7.3C, D). When this offset is eliminated the spacing between the fibres is equal to the supporting wall segment height between SF layers (Figure 7.3E) yet requires vertical or tilted fibre positioning during the cell seeding to maximise the number of cells, trapped in the scaffold. The 'ladder' arrangement of the SF was considered beneficial due to a higher achievable fibre density in the projection on the XY plane and scaffolds with such SF arrangement could be successfully utilized for mouse DRG culture (Figure 7.3F, G). In these scaffolds, SFs with an approximate diameter of 2.5 µm, positioned with a 36 µm offset from each other, supported by 1 mm

spaced fibre walls, printed with 12.5 µm fibres. In the Z-direction the SF layers are separated by two supporting wall fibres. DRG is held by the SFs which serve as a substrate for Schwann cells and neurites spreading. Nevertheless, the main direction of the neurite growth was along the supporting walls, where the also most Schwann cells were located and aligned.

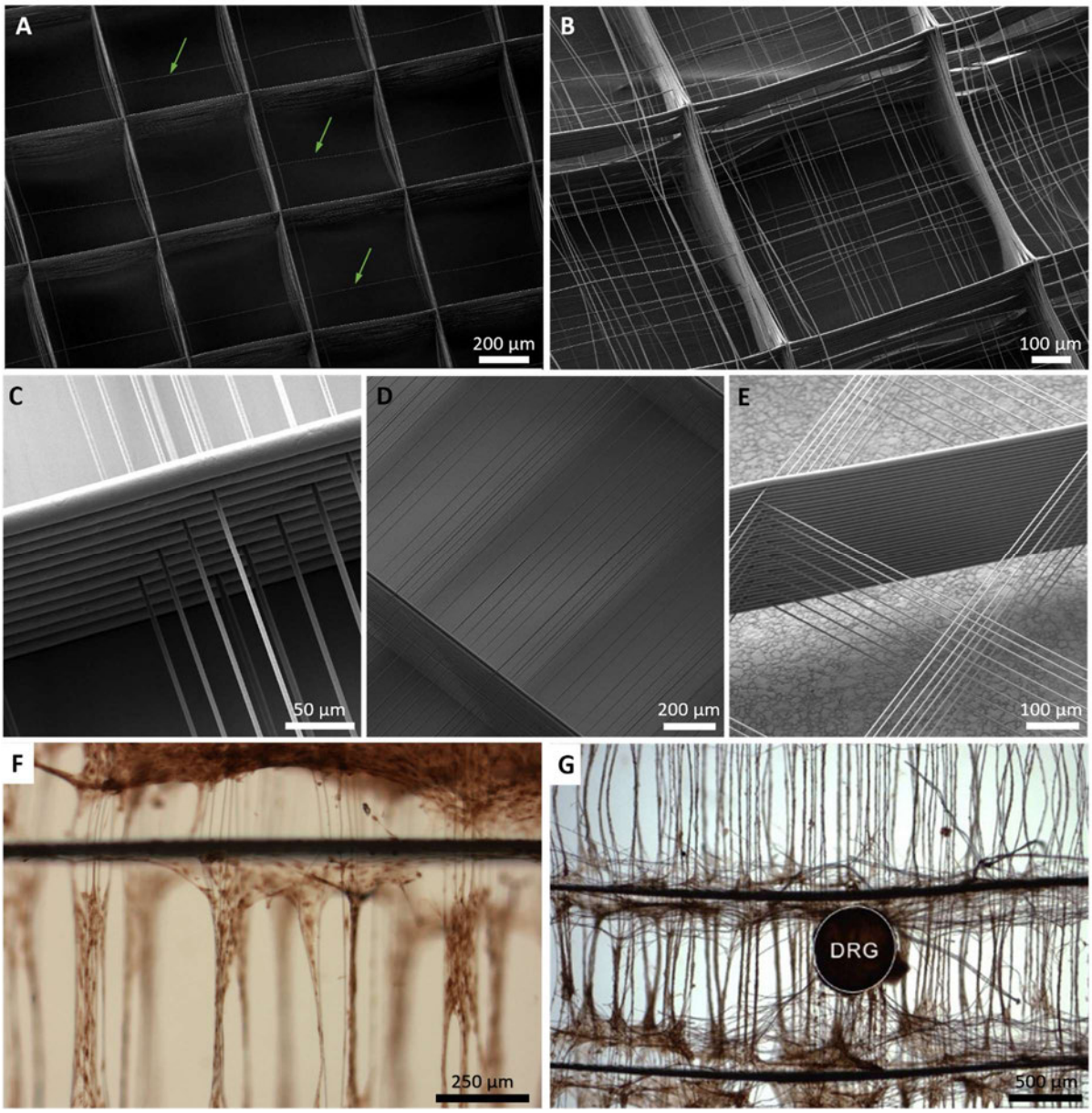

Figure 7.3. Incorporation of suspended fibre arrays into MEW scaffolds. A: Individual suspended fibres (shown by green arrows) in a square grid scaffold. B: three layers of orthogonal suspended fibre arrays. The positioning is distorted by fibre attraction to the thick fibre walls and each other. C: Parallel fibre arrays D: A construct with high density suspended fibre arrays. E: Crossing suspended fibres. F, G: A Light microscope images of the anti-S100ß stained Schwann cells and the ß-III tubulin/ neurofilament 200 kDa - positive neurite extensions from mouse DRG after 21 days *in vitro* respectively. DRG images kindly provided by Dr. G. Brook.

A notable point regarding the conventional MEW scaffolds produced in the majority of publications (and previous Chapters of this thesis) is the cube-volume of the pore (cuboid) that is oriented in the Z-axis. This means that MEW scaffolds are generally open from the top and the bottom of the scaffold (Z pore scaffold) to cells. With this design, no interconnections between the adjacent pores are present (Figure 7.4A), just small gaps that may occur (shown in Chapter 3; Figure 3.8) in the X or Y-direction, near fibre junction points. In order to estimate the ability of the scaffold to direct the neurite and supporting cells spreading out of DRGs, two alternative scaffold designs were proposed with defined interconnections between the cuboid pores in one (along Y-axis) and two (along X and Y axis) directions (Figure 7.4B, C). Those scaffolds are hereafter termed as Z/Y and Z/Y/X pore scaffolds, respectively.

The size of the pores in Z-direction was set to 400 µm, enabling the seeding of the DRG into the pores, yet preventing their falling through the scaffold. The designed size of interconnecting pores in the X and Y directions was set to 12 fibre diameters, printed in between two adjacent fibre walls.

To maintain the fibre wall morphology constant, the same process parameters were used for all three scaffold types. To achieve that the parameters for the scaffold manufacturing had to be adjusted in the way that would simultaneously enable fibre suspension and maintain the satisfactory fibre placement accuracy throughout the desired scaffold thickness (>500 µm). However, those two requirements require contradicting parameter changes: For improved fibre suspension, the minimal possible temperature [224] and voltage are required, as well as a fast collector speed (unpublished data). On the other hand, higher temperature would facilitate the removal of unwanted gaps between the fibres whereas higher voltage improves the fibre placement precision (see Chapter 3) and allows the printing of thicker scaffolds.

Due to a different thickness of parallel stacked fibres and the crossing ones (see Chapter 3), the number of fibre layers had to be adjusted individually for each scaffold type, taking into account that the mean fibre diameter was 8.03±1.33 µm and absolute scaffold thickness had to be at least 550 µm. Z pore scaffolds had 72 fibre layers in each direction. The structure of a Z/Y pore scaffold included a set of 12-fibre wall in Y direction with eight intersecting fibres on top, repeated three times. For the bottommost layer four additional scaffolds Increase of the height of the first walls, printed on the collector was intended to

improve the suspension of the fibres (data not published), printed over it. In a Z/Y/X scaffolds a total of 6 fibre walls (three per orthogonal direction) with 13 fibres in each were printed don top of each other. An increase both in the number of stacked walls or the fibres in a single wall led to an unacceptable number of stray fibres in the top layers of the scaffold (Figure 7.4D-F).

As seen in Figure 7.3G-H, certain defects were not possible to avoid. In the upper layers of a Z-pores scaffold gaps can appear in the fibre walls due to a partial fibre suspension between the scaffold height peaks in the fibre intersection points (Figure 7.4G). Those gaps were also present in the Z/Y pore scaffolds (Figure 7.4E). Another critical defect that was occasionally appearing on the printed scaffold were stray fibres. Those could be both misplaced direct-written fibres as well as nanofibers, generated by secondary jets. The misplacement of the fibres is likely to occur due to a charge accumulation in the top layers of the scaffold while the secondary jets are appearing from melt droplets, attracted from the collector back to the nozzle and a brass electrode (Figure A.1 , Appendix A) around it [60].

An additional design element, an interlocking fibre (Figure 7.4F), had to be implemented into the design of a Z/Y/X pore scaffolds to improve the structural stability during the handling and prevent fibre wall separation (Figure 7.4I). Without those fibres, the contact area between the perpendicular walls was limited to the intersection points, making the scaffold delamination practically inevitable already at the stage of a scaffold removal from the collector.

Apart from the scaffold design, the contact area that defines the force, needed for the detachment of one fibre from another depends on the temperature of the polymer. Typical force-displacement curves (Figure 7.5A) and maximal registered forces (Figure 7.5B) indicate that by decreasing the polymer temperature the fusion between the fibres is almost eliminated. At a faster collector speed, it is likely that the increased length of the jet leads to a decrease of a jet temperature in the contact point down to the values when the stored heat is not sufficient to melt the fibre underneath and form a junction.

The contact area was not equally distributed along the fibre length (Figure 7.5C, D). During mechanical testing, when a such an individual junction was broken, an instant force drop was observed (Figure 7.5A).

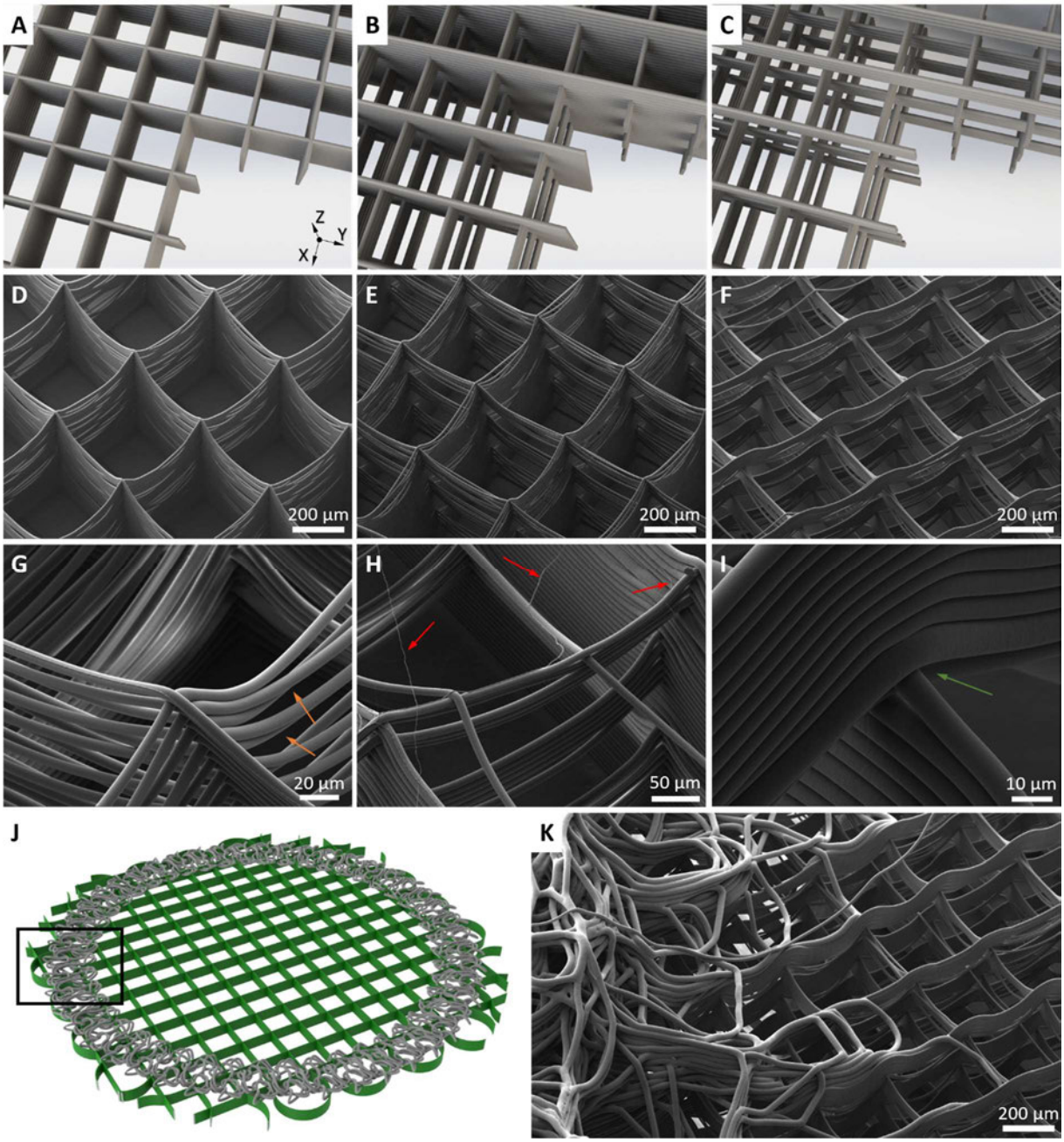

Figure 7.4. MEW scaffolds designed for dorsal root ganglia seeding. A-C Scaffold designs with pores in Z, Z/Y, and X/Y/Z directions, respectively. D-F: Scanning electron microscope (SEM) images of the corresponding MEW scaffolds. G: Unwanted gaps in the walls of the Z pore direction scaffold (orange arrows). E: Stray randomly located fibres with a diameter in the range of several hundred nanometres, indicated by red arrows. F: An “interlocking” fibre, added for the improvement of the structural integrity of the scaffolds during handling (green arrow). J: A rendering of a scaffold (green) with a reinforcing frame (white), printed with thicker buckling fibres. K: A SEM image of an edge part of a scaffold.

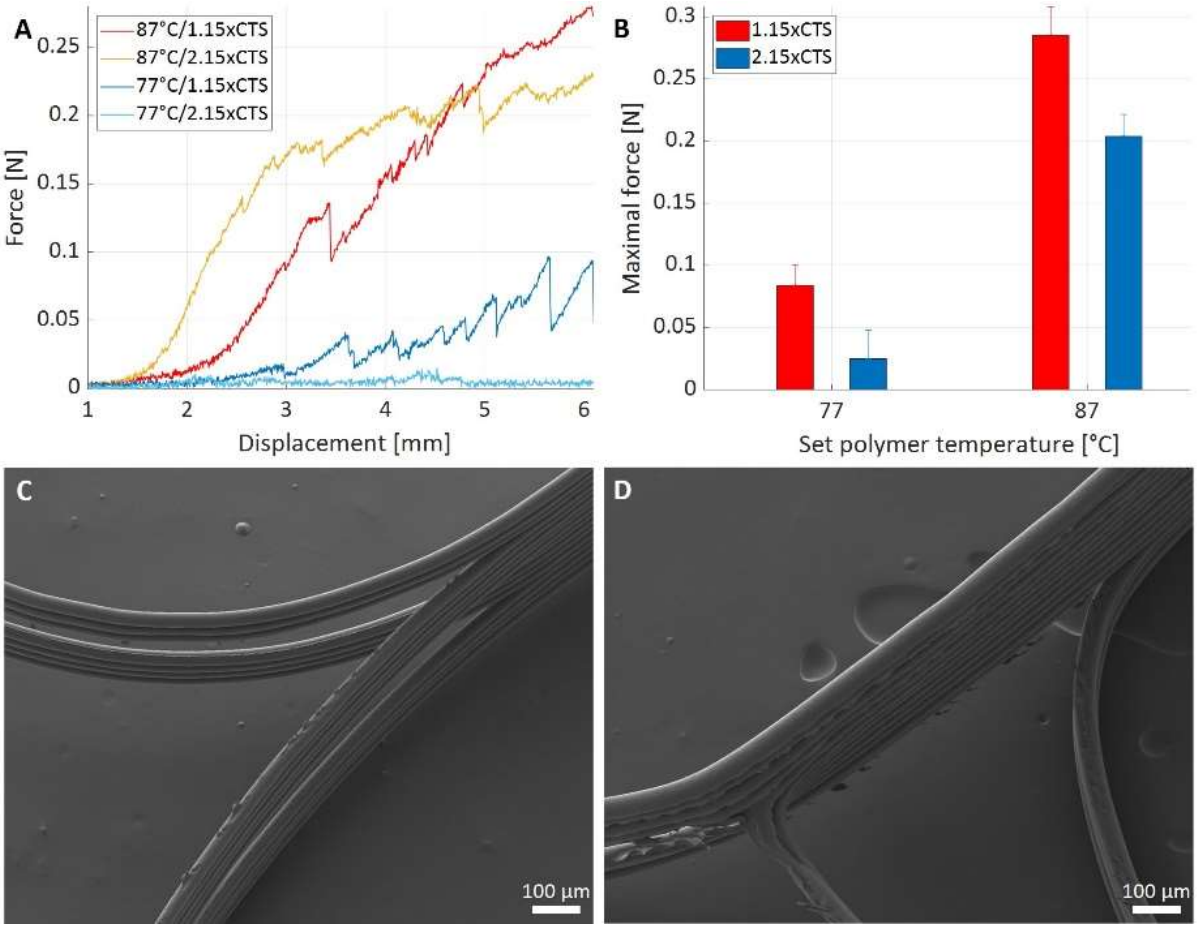

Figure 7.5. Mechanical testing of fibre fusion. A: Characteristic force-displacement curves. B: Average maximal force, measured during the tensile test. C, D: SEM images of the fibre junction area after the test of a sample, printed at a set polymer temperature of 77°C and 89°C, respectively.

It is also remarkable how the degree of fibre fusion changes with the structure height: Whereas the bottom layers of a sample, printed at 89°C can be detached from each other with the destruction of the inter-fibre junctions, the upper fibres are plastically deformed by tension instead of detachment (Figure 7.5D). These results explain the sensitivity of the Z/X/Y pore scaffolds integrity to mechanical loads, revealed below.

7.3.2 DRG explantation and visualization

The general morphology of the embryonic chick DRG, seeded on the scaffolds could be demonstrated with the SEM images. The area of the cell spreading was varying from one DRG to another and did not depend on the scaffold type (Figure 7.6A-C). From the observations it can be inferred that for all scaffold types the predominant spreading of the cells primarily occurred on the top of the scaffolds, parallel to a slower migration down into the Z pore (Figure 7.6D), similar to the hMSCs behaviour, described in Chapter 4. The presence of the

designed pore interconnections could influence guidance of the neurites and supporting cells but was not feasible to quantify. Particularly clear it was visible in the Z/Y/X pore scaffolds, where the cells could spread along the perpendicular fibre walls without interruptions (Figure 7.6E, F). For a better demonstration of this effect, the unwanted gaps in the walls of Z pore scaffolds must be eliminated together with an increased scaffold thickness and controlled positioning of a DRG in a pore. Further reinforcement of Z/Y/X pore scaffolds is also needed to maintain the straight wall shape and prevent the delamination in the bottom part of the scaffold, ensuring the cell spreading throughout the whole designed scaffold thickness (Figure 7.6G).

Although SEM images were helpful in visualization of the supporting cells and neurite bundles coming out of the cell mass (Figure 7.6H, I), it was often not feasible to follow the neurites on the walls or undoubtably distinguish them from the stray nanofibers and cells of different types (Figure 7.6I).

A selective visualization of the DRG neurons was done with immunostaining of the cytoskeleton component, neuron specific protein ß-III-tubulin. With a secondary DAB staining the location of the neuronal cell bodies and neurite projections inside the DRG was revealed after three days *in vitro* (Figure 7.7). The neuron cell bodies were usually compactly localized within one pore (Figure 7.7A) but could also be distributed over a larger area. It might be related to the initial DRG size, shape, and positioning during the seeding. After the neurite left the DRG, their extensions on the fibre walls were harder to detect. Partially it was related to the small neurite diameter compared to the PCL fibres.

Immunofluorescent staining was more efficient in the demonstration of the neurites spreading along the fibre walls. Adding the phalloidin staining against F-actin in the non-neuronal cell cytoskeleton and DAPI clearly shows how the neurites exit the DRG and extend along the scaffold fibre walls (Figure 7.8A-C). Because of the preferential spreading of the DRG on top of the scaffold, it was problematic to guide the neurite outgrowth (Figure 7.8D-F). The initial directions of the neurite extension in the scaffold mainly depended on the DRG size and position in the scaffold. In case when all the neuron cell bodies were contained in one cuboid pore, the neurites were spreading along the walls forming that pore. A DRG, that was covering the top of several pores allowed the neurites to spread along all the top fibres of the covered area. The immunocytochemical staining confirmed that some DRGs were emitting multiple

neurites, which were spanning over the pore lumen. This morphology could be strictly addressed neither to the scaffold type, nor to the time spent in culture (Figure 7.8F, G).

Since the neurite outgrowth requires a hard substrate surface, fibres, hydrogel or at least a vicinity of a liquid-air interface [225-227], it can be speculated that the neurite processes, spanning the pores could appear either during a gradual movement of a neurite growth cone from one wall, forming a pore onto a perpendicular one, while detaching from the first wall or due to a presence of a medium-air interface around a DRG, when a scaffold is not fully submerged under the surface of the medium in the well during and after seeding.

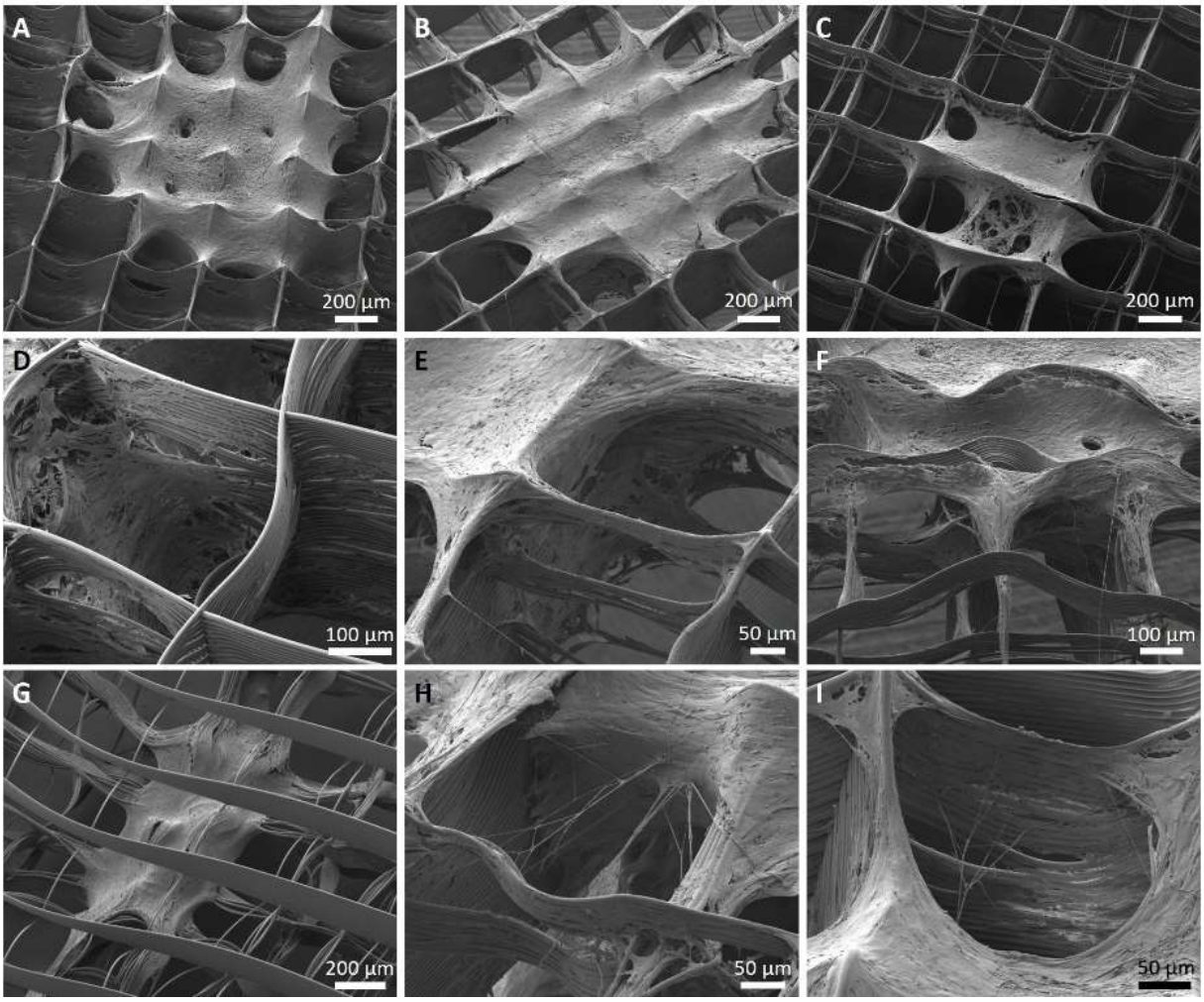

Figure 7.6. SEM imaging of dorsal root ganglia on MEW scaffolds. A-C: Tilted SEM Images of the E10 chicken dorsal root ganglia (day 7), seeded onto the scaffolds with pores in Z, Z/Y, and X/Y/Z directions, respectively. images of a sample and mechanical testing setup. B: Characteristic force-displacement curves. C: Average maximal force, measured during the tensile test. D, E: SEM images of the fibre junction area after the test of a sample, printed at 77°C and 89°C, respectively.

In most cases, with the longer time *in vitro*, both the supporting cells and neurites were spreading further from the initial DRG position. Along with that, DRGs with no supporting cell spreading (Figure 7.8G) or neurite growth (Figure 7.8H) could also be found although most of them demonstrated neurite outgrowth already at day 1 (Figure 7.8I).

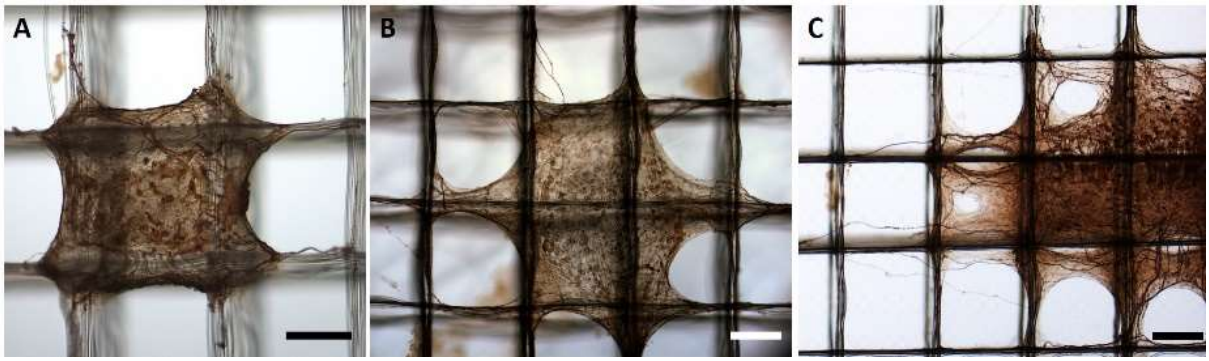

Figure 7.7. A microscopic image of 3,3'-Diaminobenzidine (DAB) stained E10-11 chick dorsal root ganglia (DRG), immunolabelled for β-Tubulin III on Day 3 *in vitro*. A: A small DRG in a Z pore scaffold. B: Medium sized DRG in a Z/Y pore scaffold. In the background the stained blocking solution agglomerates are visible. C: A large DRG, spanning multiple Z pores in Z/Y/X pore scaffolds. Scale bars are 200 µm.

The difference in the character of the neurite spreading between different scaffold types could only be properly visualized with a confocal microscope (Figure 7.9): Both the signal amplification and the Z-stack option for an increased depth of focus (up to 400 µm) in thick samples were crucial for the neurite visualization. In contrast to the glia spreading, practically unaffected by the scaffold type (excluding the cases of Z/Y/X pore scaffolds with delamination), neurites on the Z/Y and Z/Y/X pore scaffolds were observed passing through the designed Y and X direction pores. Those neurite outgrows could be located on several depth levels in a scaffold, e.g., three separate neurite bundles, corresponding to the pore levels are clearly visible in Figure 7.9D, E. The absolute majority of the neurites, growing through the pores stayed on the same level: When a growth direction was changed, it happened parallel to the XY plane instead of growing in the Z direction. It is possible that the grooves, formed by the fibres in the wall provide an additional directional guidance [228] which limits the outgrowth direction range of the neurites.

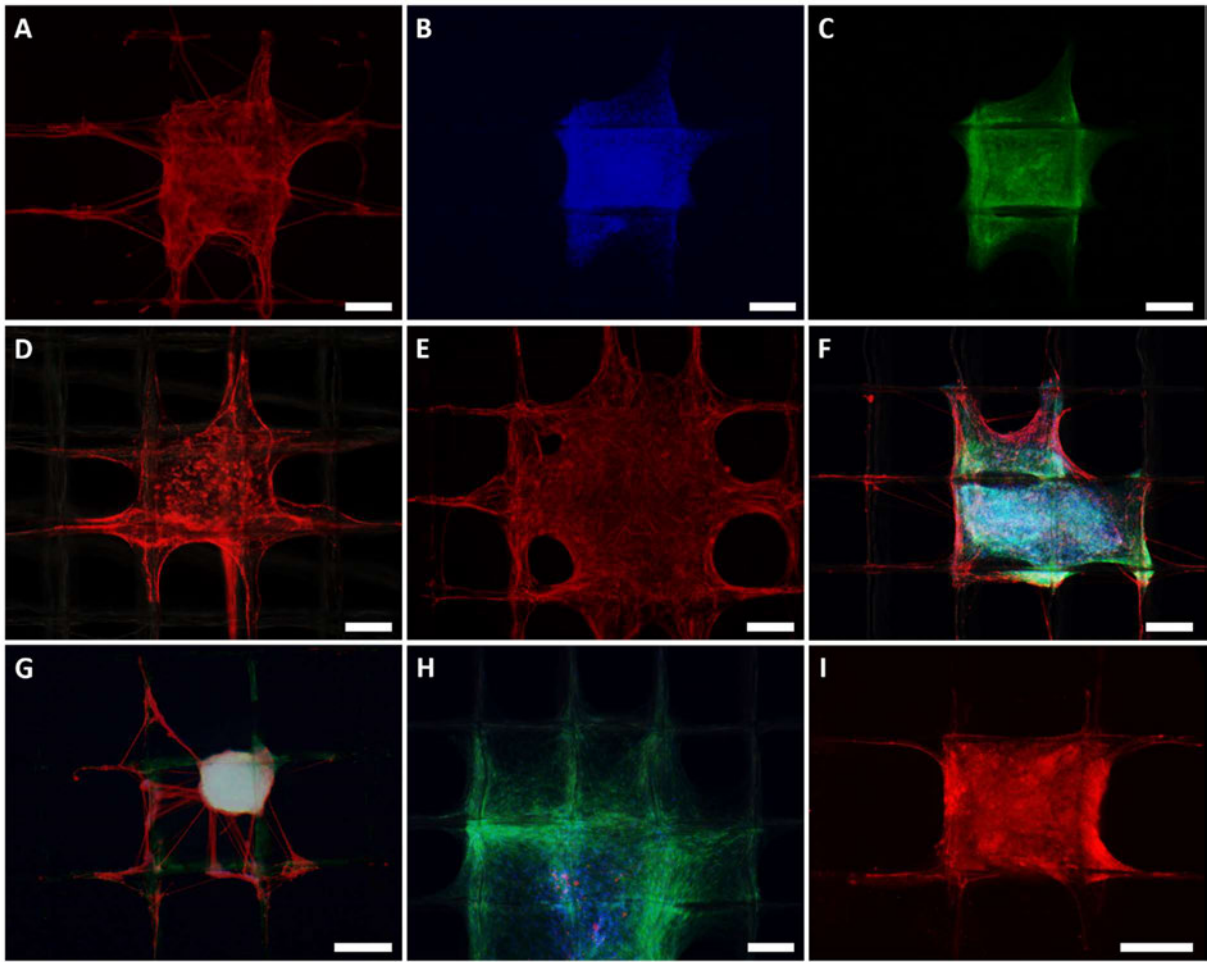

Figure 7.8. Immunofluorescent imaging of the E10-11 chick DRGs in MEW scaffolds, stained with anti-β-Tubulin III (red), Phalloidin (green) and DAPI (blue). A-C: Day 3, Z/Y pore scaffold. Separate channel in each image. D: Day 3, Z/Y/X pore scaffold. Neurites, growing along the lower walls are out of focus. Red channel only. E: Day 3, Z pore scaffold. Red channel only. F: Day 3, Z/Y pore scaffold. G: Day 7, Z pore scaffold, merged channels. H: Day 7, Z/Y pore scaffold, merged channels. I: Day 1, Z pore scaffold, red channel only. All scale bars are 200 µm.

The presented results suggest that the tested scaffold architectures are capable of only a limited control over the DRG cell behaviour. Although the neurites can use the whole depth of the scaffold and have a preferred direction of spreading, the growth of the neurite network on the top of the scaffolds was similar for all scaffold types. The neurites that are following the pore sequences also could change their direction, while meeting a perpendicular fibre wall (Figure 7.9E). Apart from that, the presence of the unwanted gaps between the fibres and weak mechanical properties of a Z/Y/X pore scaffold, could not guarantee a fully controlled geometrical environment.

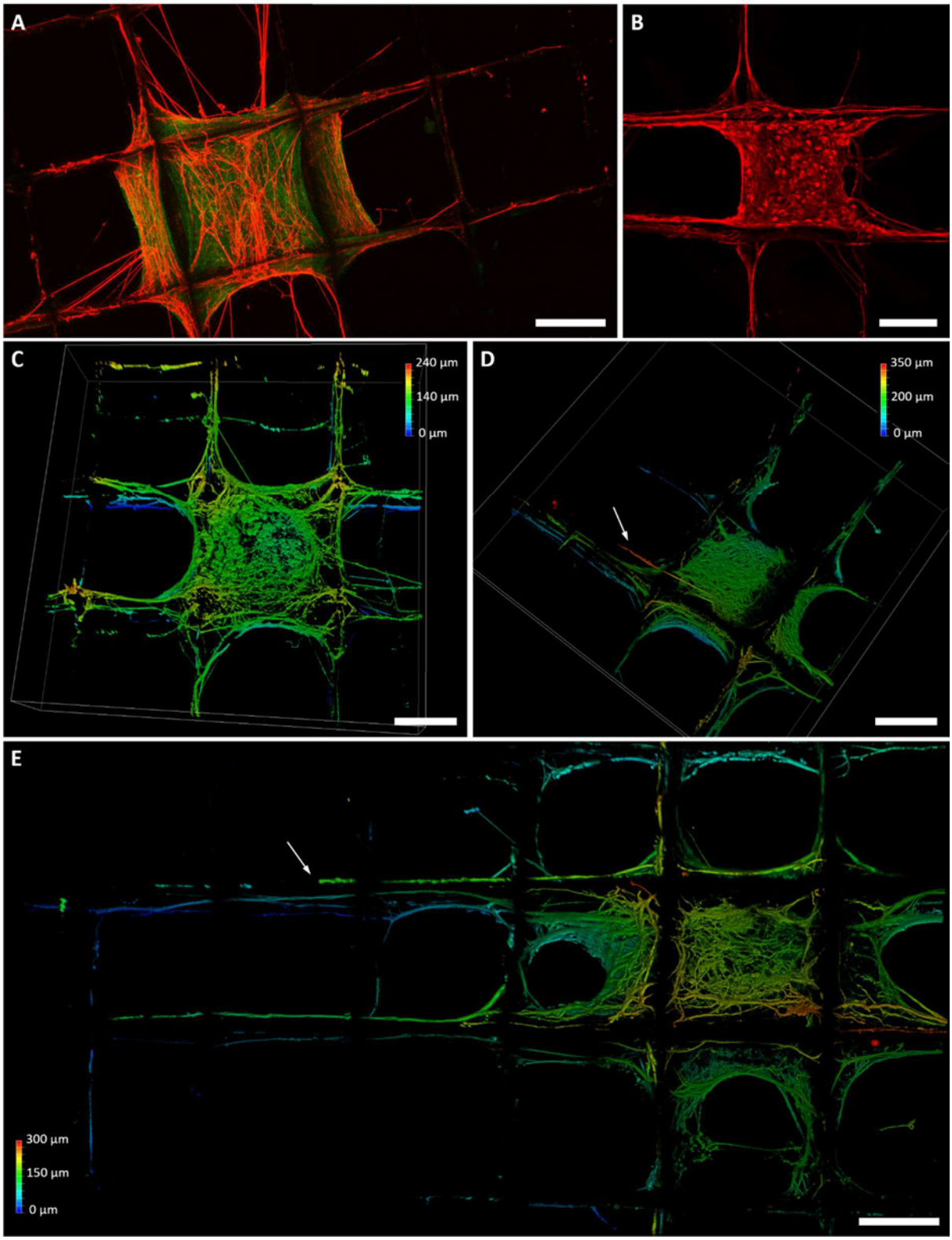

Figure 7.9. Confocal micrographs the E10-11 chick DRGs in MEW scaffolds stained with anti-β-Tubulin III (red) and Phalloidin (green). A: Day 6, Z-pore scaffold, stacked top view. B: Day 6, Z-pore scaffold, stacked top view, red channel only. C-E: 3D reconstructions anti-β-Tubulin III-stained neurons, coloured according to the position depth on the scaffolds with Z, Z/Y/X and Z/Y pores, respectively. White arrows point at neurite bundles, corresponding to the pore levels. All scale bars are 200 µm.

Nevertheless, an application of 3D scaffolds with accurately controlled architectures could demonstrate various cell behaviour patterns, such as neurite spreading with or without supporting cells and neurite spanning thought the scaffold pore voids, which has not been properly described so far.

A further improvement of such scaffolds in regards of increased thickness and fidelity is obstructed by conflicting requirements to the process parameters, is yet considered feasible. Improvement of this test system can be achieved by a complete elimination of the scaffolds defects and a more precise location of a DRG in the pores. Changes in the scaffold design, such as the introduction of catching fibres (see Chapter 4), assisting in precise determination of the DRG location in a pore can be implemented to reduce the influence of a DRG position in a scaffold on the direction of neurite growth. Potential use of such scaffolds may be further realised in the studies of tissue innervation by seeding a DRG and, for instance, tissue spheroids in a single scaffold.

Chapter 8: Summary and outlook

This thesis spans multiple aspects of MEW; hardware construction, processing and scaffold designs were developed and optimized so that it is generically applicable across multiple biomedical applications. In Chapter 3, important aspects of the MEW head design are discussed, and the influence of selected processing parameters and ambient conditions was investigated. In the context of the improvement of the printing speed, it was found that voltage and collector distance can increase the CTS without affecting the fibre morphology, whereas polymer temperature and feed pressure affect the fibre diameter. A weaker, yet significant CTS increase is also achieved by the application of a positive nozzle and negative collector voltage over the reverse polarity. Simultaneous decrease of collector distance and applied voltage could help achieve decreased minimal fibre spacing values. Ambient conditions, such as air temperature and humidity also had influence on the printing results, leading to higher CTS values. A combination of high ambient temperature and humidity lead to insufficient cooling of the jet and deposition of partially molten fibres. In other situations, e.g., when the polymer temperature is lowered, such higher humidity can potentially have a positive effect on the mechanical stability of the scaffold by improving fibre fusion. Those effects need further investigation in a study, where polymer temperature is altered together with the ambient temperature and humidity, to find the optimal printing regimes in terms of printing speed, scaffold fidelity and mechanical stability.

The defects which appear in the scaffold with small pore sizes (<2×minimum fibre spacing) with the increasing layer height could not be compensated with both charge removal techniques investigated here. Nevertheless, it is possible that under the test conditions, the reason behind the defect appearance does not solely lie in the charge accumulation and includes the effects from the changing jet lag length. Therefore, both techniques as well as the air humidity require further investigation with thicker (hundreds of layers) scaffolds, printed at a speed, close to the CTS.

Accurate and predictable fibre diameter adjustment during the printing of MEW scaffolds is explained in Chapter 4 so that this outcome can be part of design criteria. The fibre diameter changes nearly instantly during collector speed alterations. The transition to a new pressure should be followed by a jet stabilization, during which a sham construct has to be printed off-sample for up to 5 min. Used concurrently, those parameters allow to combine fibres with diameter ratio above 20-fold in one continuously printed scaffold. This opens new

perspectives in design of the MEW scaffolds with higher complexity, which can combine areas with different morphologies and mechanical properties. The fact that the effect of those parameters can be calculated with a satisfactory accuracy by means of simple equations facilitates the scaffold manufacturing: The calculated pressure and speed values can be directly programmed into the G-code. Two novel scaffold designs were presented as a demonstration of the multimodal and multiphasic scaffolds that can be successfully manufactured, using the proposed approach.

The attraction of the fibres to the previously printed fibres and fibre walls was quantified in Chapter 5 by defining the minimal possible programmed spacing between the fibre that is being deposited and the existing fibres. Additionally, the actual distance between the fibre and the fibre wall was measured, suggesting possible inaccuracies during scaffold production with non-uniform height. An investigation of fibre separation from the wall, lead to the discovery of a technique for the compensation of the shape deformation, growing with the height of curved structures by a printing path update layer-by layer. A linear increase of the amplitude and phase shift correction, proportional to the layer count, was successfully applied for a sinusoidal structure. For the other curved shapes, a general law, connecting the correction magnitude to the structure height, needs to be found.

Even when the aforementioned structure tilt is eliminated, non-linear patterns rarely correspond to the G-code programmed toolpath, since the first deposited layer is already off-position due to the presence of a jet lag. The geometrical model, described in Chapter 6 is a ready to use tool for the prediction of MEW fibre laydown pattern, deposited with a constant collector speed on a flat surface. Input data for the model are the CTS and stable jet lag values, measured for different collector speeds. The model was successful in the approximate prediction of the fibre deposition, independent of the pattern shape and collector speed. The equation for jet lag calculation was tested for various parameter combinations and demonstrated the general applicability of the model for various printing setups with necessary of the lag equation coefficients adjustment. Accurate prediction of the stacked structures was not decreased but able to indicate the regions with the largest wall tilt. Fibre diameter calculation is limited to sufficiently long straight lines and periodic curves but also allows qualitative assessment of the printed structures. The proposed model MEW can become a

part of an iterative MEW scaffold design workflow accelerating the transition from the design to a MEW printed object.

In Chapter 7 the design and manufacturing of MEW scaffold with defined pore size and direction by means of the introduction of suspended fibres was demonstrated and discussed, incorporating suspended fibre elements into the design. These scaffolds were tested with the embryonic chick DRGs and demonstrated the principal ability to guide the neurite growth. The results indicate that MEW scaffolds with arbitrary designed pore interconnectivity can be successfully applied to represent a controlled 3D environment in neural TE.

There are several directions of further MEW development, crucial for the expansion of the application range and commercialization of MEW products. Despite the significant progress, achieved in the field of MEW in the recent years and a constantly growing list of scaffold materials, architectures, and biomedical applications, the lack of knowledge and the inherent limitations of MEW are still preventing the realization of its full range of capabilities regarding accuracy, feature size and shape freedom.

With the introduction of large volume constructs, printing times of dozens of hours are already affecting the research efficiency with MEW scaffolds and are a clear issue in commercialization. Nevertheless, the approach of jet manipulation, proposed by Liashenko et al. for solution electrohydrodynamic printing is a potential key to a dramatic increase in MEW production performance.

MEW has shown an impressive growth in the number of publications and research groups, working with it but there is a visible threshold in printing of complex geometries. The reason behind was the manual g-code programming and discrepancy between the coded paths and the resulting scaffold shape because of jet lag in combination with electrostatic attraction and repulsion, which depend on multiple factors, constantly changing during the printing process. In order to overcome that barrier, computational models based on the process physics and machine learning approach will be competing to provide the most accurate result and the ease of use in order to enable a straightforward pathway from CAD design to a ready scaffold. This deposited pattern prediction also needs to be expanded to the printing on a 3D surface, where surface curvature is the major factor for the spatial electrical field irregularity. The creation of physical model will require an in depth understanding of

various physical aspects such as electrostatics, viscoelastic jet mechanics and cooling and solidification processes. For the machine learning approach, appropriate data collection and analysis systems are required, including the capturing of the scaffold shape in 3D and registration of the influence of all the MEW printing and environmental parameters.

In summary, the progress on MEW process characterisation, fibre diameter and printed structures, demonstrated here facilitates the application of MEW scaffolds for biomedical applications. The importance of those improvements was shown on several scaffold types for various biomedical applications, focusing on neural TE. This progress might be crucial in utilizing the full potential of MEW.

Appendix

Appendix A. Technical drawings of a MEW printer

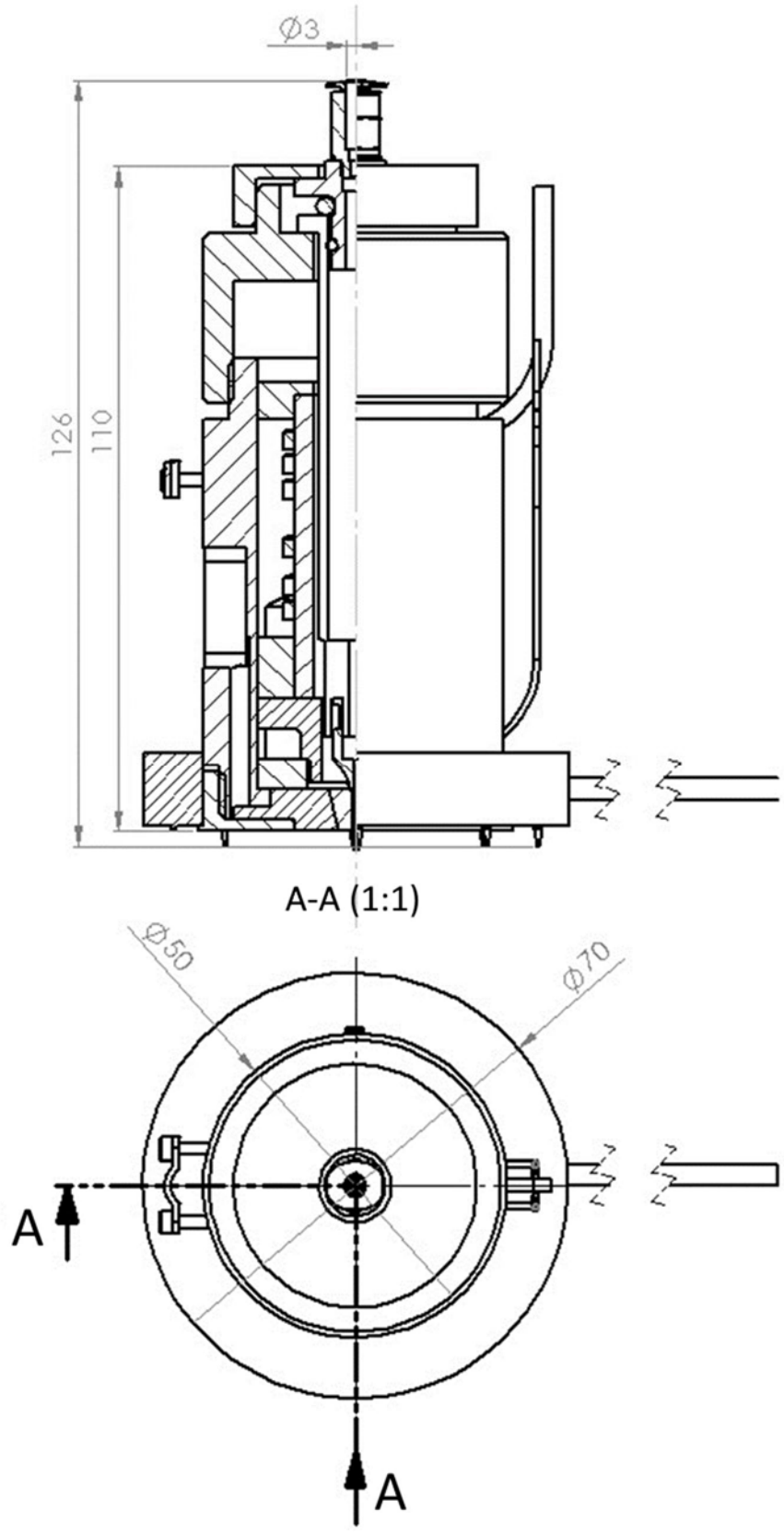

Figure A.1.1. Design of a MEW printing head

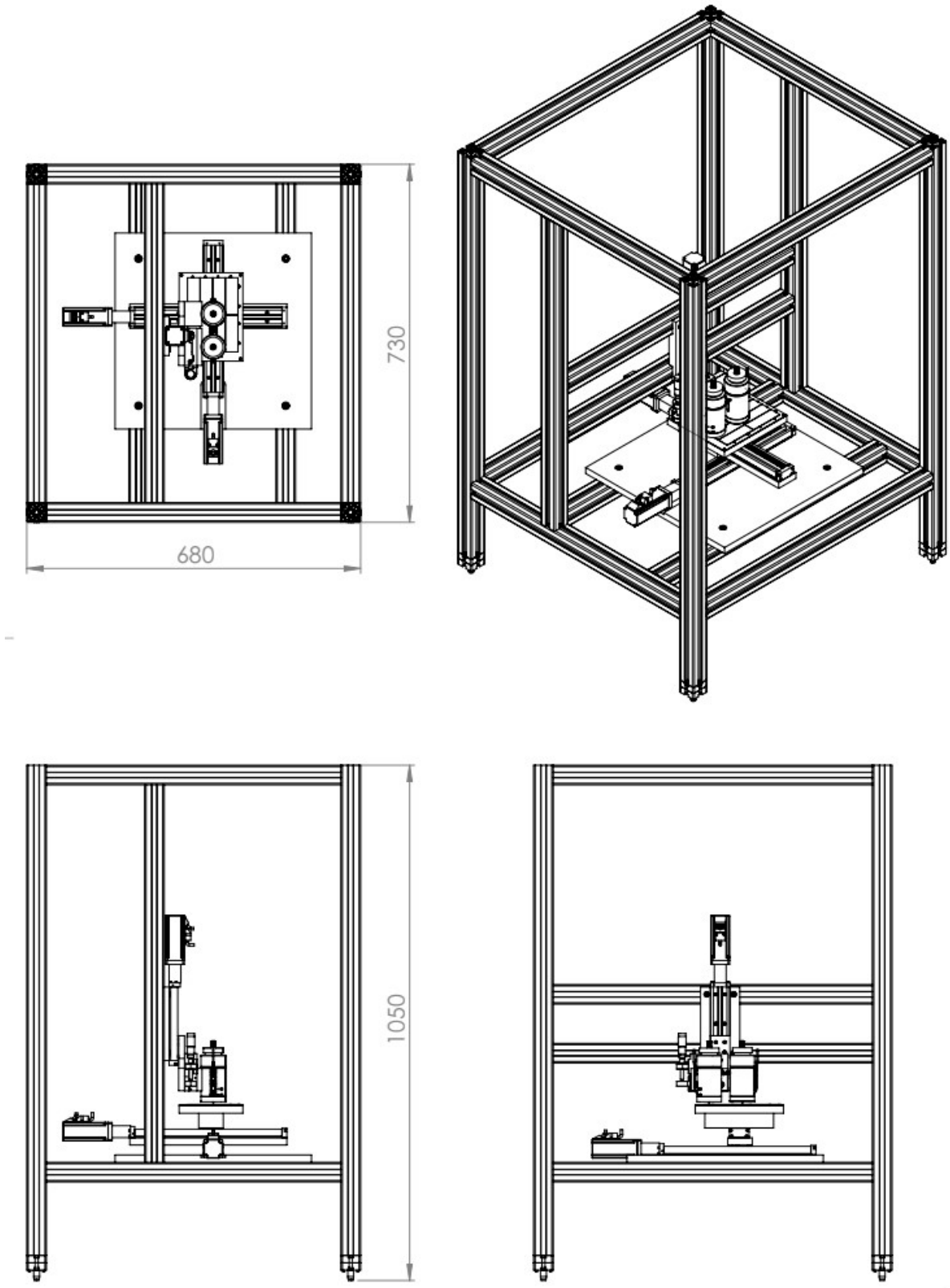

Figure A.1.2. General design of a MEW printer with two printing heads

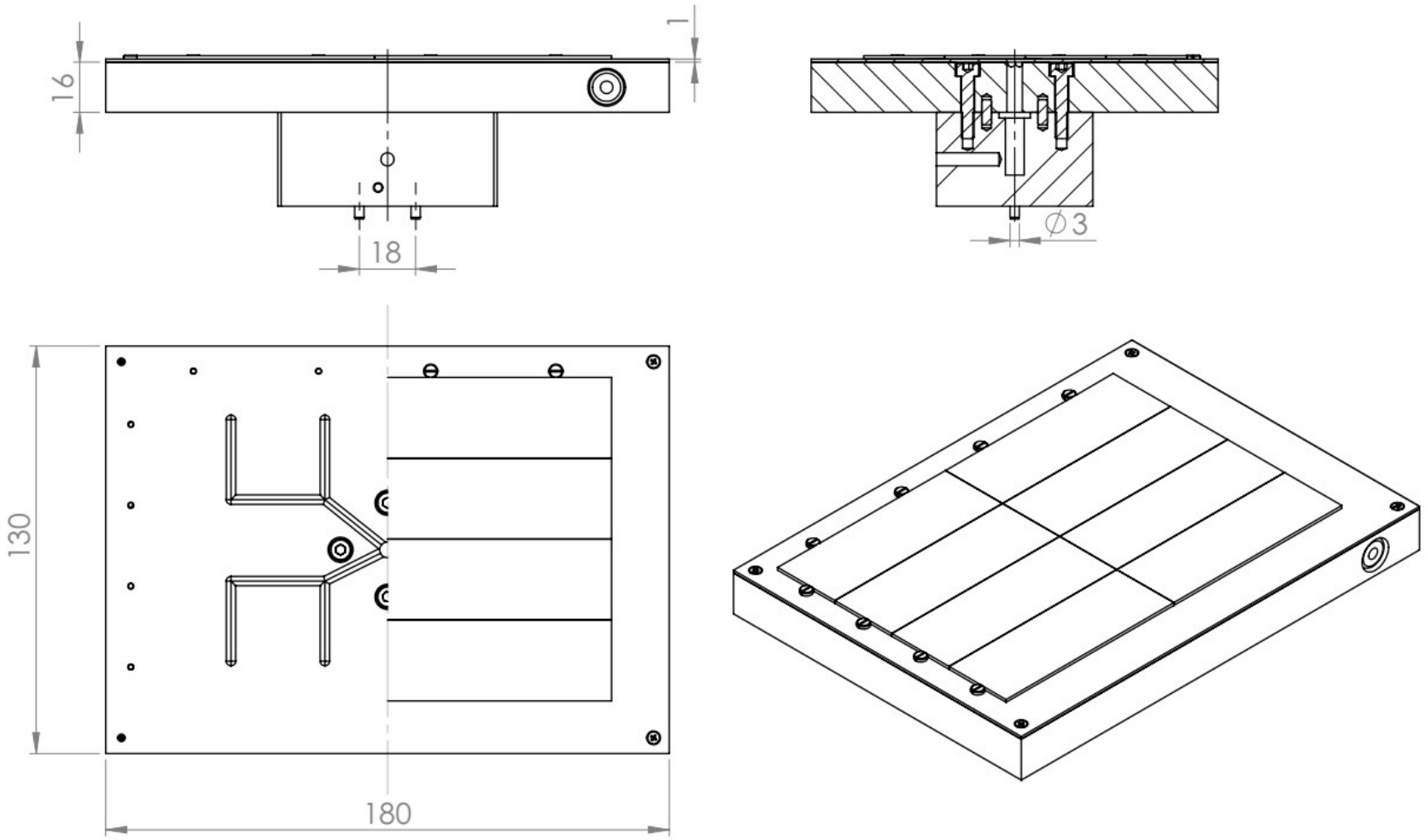

Figure A.1.3. Design of a collector with a vacuum fixation of glass slides

Appendix B Example G-code programs

All codes presented here are written for Rexroth IndraMotion MTX control system

G-code for a multiphasic scaffold with square, pseudorandom and triangular pores

```
; 8 layers of triangles+1 layer of suspended 24-gons+ 5 layers of boxes
; 500 µm fibre spacing
; external subroutines: SRRBv1, SRRRGv2
; duration measurement, written in the file "TM"
; Voltage: -1,5+4 kV; Collector distance: 3.5 mm,
; Needle gauge: 22G; Applied feed pressure: 1 bar;
;21.0°C, 32% rH; 85°C

;Parameter variables
(-------------------------------------------------------------------)
; Temperature and pressure configuration
T1=850
T2=850
P=10

;Working area
1 #XMAX=230
1 #XMIN=45
1 #YMAX=152
1 #YMIN=40

;Base feedrate for the linear and circular movement
1 #FEEDF=500
1 #FEEDR=400

;Pause before (TI) and after (TO) the loop
1 #TI=0.2
1 #TO=0.1

;main program
(-------------------------------------------------------------------)

N010 G17 G8 G90
;Starting time
0015 STARTTIME%=CLOCK

;stabilization;
N020 G1     X[#XMAX]    Y[#YMAX]    F[#FEEDF]
N030 G91
0040 CALL SRCMv1 (3,5.8,8,10,1,1500)
;stabilization time 6 min 23 sec

N050 G90
N060 G1     X212  Y[#YMAX]    F[#FEEDF]
N070 G91

;three zones scaffold
N080 LP TRIL (24, 8, 24, 5, 0.5, 0.1)
;P1 - construct size, P2 - tri height, P3 - #SF layers, P4 - box height
;P5 - box size, P6 - SF spacing,


;Measure the time, switch off the pressure and go to initial position
0090 ENDTIME%=CLOCK
0100 TIMEH%=INT((ENDTIME%-STARTTIME%)/3600000)
0110 TIMEM%=INT((ENDTIME%-STARTTIME%-(TIMEH%*3600000))/60000)
0120 OPENW(1, "TM")
0130 REWRITE(1)
```

```
0140 PRN#(1, "Running time was:",TIMEH%,"h",TIMEM%,"min")
0150 CLOSE(1)

P=0
N160 G90
N170 G1     X[#XMAX] Y[#YMAX] F[#FEEDF]
M30

;Internal subroutines
(-----------------------------------------------------------------)
LPS TRIL
;triangles +SF mesh + boxes
;P1 - construct size, P2 - tri height, P3 - #SF layers, P4 - box height
;P5 - box size, P6 - SF spacing,

1 CSIZE=P1
1 BSPEED=500
1 SFLENGTH=40
1 SFSPEED=6000
1 BOXSIZE=P5
1 SFSPACING=P6
1 SFWIDTH=CSIZE-4

G91
G1 X-5 Y-5 F[BSPEED]
1 WAIT
1 POLECX= MCS(1) - CSIZE/2
1 POLECY= MCS(2) - CSIZE/2
POP([POLECX], [POLECY])
PLS(X[POLECX], Y[POLECY])
;Triangles
CALL SRRRGv2 (CSIZE, CSIZE, BOXSIZE, 3, P2, BSPEED)
;P1 - X size, P2 - Y size, P3 - spacing, P4 - number of rotations, P5
- Height, P6 – speed
;Suspended membrane
CALL SRRRGv2 (SFWIDTH, SFLENGTH, SFSPACING, P3, 1, SFSPEED)
;Squares
CALL SRRRGv2 (CSIZE, CSIZE, BOXSIZE, 2, P4, BSPEED)
PEND
```

External subroutines.

1. Rectangular pore scaffold subroutine

```
;Rectangular construct with a circular pattern for constant speed
during stabilization
;Parameters: P1-hight(layers), P2 - circle radius, P3 - Size in X-
direction
;P4 - size in Y-direction, P5 - circle spacing, P6 - linear speed

1 H=P1
1 CRAD=P2
1 XSIZE=P3
1 YSIZE=P4
1 CSPC=P5
1 FEEDL=P6

1 NCX%=INT(XSIZE/CSPC)
1 NDCY%=INT(YSIZE/(2*CSPC))

G91
G1    X0    Y[-CSPC*(NDCY%-1)+CRAD]       F[FEEDL]
G3    X[CRAD]     Y[-CRAD]    R[CRAD]     F[FEEDL]

1 FOR I%=1 TO H
1     FOR J%=1 TO NDCY%
1           FOR K%=1 TO (NCX%-1)
```

```
                G2 X0       Y0    I0 J[-CRAD] F[FEEDL]
                G1 X[CSPC]  Y0    F[FEEDL]
      1         NEXT K%
            G2 X0       Y0          I0 J[-CRAD] F[FEEDL]
            G2 X[CRAD]  Y[-CRAD]    R[CRAD]     F[FEEDL]
            G1 X0       Y[-CSPC*(1+2*(J%-1))]               F[FEEDL]
            G2 X[-CRAD] Y[-CRAD]    R[CRAD]     F[FEEDL]
      1         FOR K%=1 TO (NCX%-1)
                G2 X0       Y0    I0 J[CRAD]  F[FEEDL]
                G1 X[-CSPC] Y0    F[FEEDL]
      1         NEXT K%
            G2 X0       Y0    I0 J[CRAD]  F[FEEDL]
            G2 X[-CRAD] Y[CRAD]     R[CRAD]     F[FEEDL]
      1         IF J%<NDCY% THEN
                G1    X0    Y[CSPC*2*J%]
                G2 X[CRAD]  Y[CRAD]     R[CRAD]     F[FEEDL]
      1         ELSE
                G1    X0    Y[CSPC*J%]
      1               IF I%<H THEN
                      G2    X[CRAD]     Y[CRAD]     R[CRAD]     F[FEEDL]
      1               ELSE
                      G1 X0 Y[CSPC*(J%-1)]          F[FEEDL]
                      G3    X[-CRAD]    Y[CRAD]     R[CRAD]     F[FEEDL]
      1               ENDIF
      1         ENDIF
      1     NEXT J%
      1 NEXT I%
      M30
```

2. Rotated rectangles subroutine

```
      ;rotated linear arrays, even angular distribution
      ;external SR for the "CALL" command
      ;P1 - X size, P2 - Y size, P3 - spacing, P4 - number of rotations, P5
- Height, P6 - speed
      ;Used External SRs: SRYLv1

      1 POSRAD=0.5*SQRT(EXP(2,P1)+EXP(2,P2))
      G90
      G1(POL) X[POSRAD] A[ATAN(P2/P1)]    F[P6]
      G91
      1 FOR J%=1 TO P5
      1     FOR I%=1 TO P4
            ROT([180*(I%-1)/P4])
      1           CALL SRYLvRG(P3, P1, P2, P6)
            ;P1 - lines spacing, P2 - X-dimension, P3 - Y-dimension; P4 -
linear speed
            ROT()
            G90
            G1 (POL)  X[POSRAD] A[ATAN(P2/P1)+(180*I%/P4)]  F[P6]
            G91
      1     NEXT I%
      G90
      G3(POL) X[POSRAD] A[ATAN(P2/P1)] R[POSRAD]      F[P6]
      G91
      1 NEXT J%
      M30
```

Bibliography

[1] K. Markatos, G. Tsoucalas, M. Sgantzos, Hallmarks in the history of orthopaedic implants for trauma and joint replacement, Acta Med Hist Adriat 14(1) (2016) 161-76.
[2] A. Youssef, S.J. Hollister, P.D. Dalton, Additive manufacturing of polymer melts for implantable medical devices and scaffolds, Biofabrication 9(1) (2017) 012002.
[3] S.J. Hollister, Scaffold design and manufacturing: from concept to clinic, Adv Mater 21(32-33) (2009) 3330-42.
[4] B.P. Chan, K.W. Leong, Scaffolding in tissue engineering: general approaches and tissue-specific considerations, Eur Spine J 17 Suppl 4 (2008) 467-79.
[5] H. Jinnouchi, S. Torii, A. Sakamoto, F.D. Kolodgie, R. Virmani, A.V. Finn, Fully bioresorbable vascular scaffolds: lessons learned and future directions, Nat Rev Cardiol 16(5) (2019) 286-304.
[6] F.J. O'Brien, Biomaterials & scaffolds for tissue engineering, Materials Today 14(3) (2011) 88-95.
[7] S.J. Hollister, W.L. Murphy, Scaffold translation: barriers between concept and clinic, Tissue Eng Part B Rev 17(6) (2011) 459-74.
[8] L.F. Tapias, H.C. Ott, Decellularized scaffolds as a platform for bioengineered organs, Curr Opin Organ Transplant 19(2) (2014) 145-52.
[9] S. Ullah, X. Chen, Fabrication, applications and challenges of natural biomaterials in tissue engineering, Applied Materials Today 20 (2020).
[10] X. Liu, J.M. Holzwarth, P.X. Ma, Functionalized synthetic biodegradable polymer scaffolds for tissue engineering, Macromol Biosci 12(7) (2012) 911-9.
[11] M. Guvendiren, S. Fung, J. Kohn, C. De Maria, F. Montemurro, G. Vozzi, The control of stem cell morphology and differentiation using three-dimensional printed scaffold architecture, MRS Commun 7(3) (2017) 383-390.
[12] P. Roach, D. Eglin, K. Rohde, C.C. Perry, Modern biomaterials: a review - bulk properties and implications of surface modifications, J Mater Sci Mater Med 18(7) (2007) 1263-77.
[13] S. Franz, S. Rammelt, D. Scharnweber, J.C. Simon, Immune responses to implants - a review of the implications for the design of immunomodulatory biomaterials, Biomaterials 32(28) (2011) 6692-709.
[14] R.J. Mondschein, A. Kanitkar, C.B. Williams, S.S. Verbridge, T.E. Long, Polymer structure-property requirements for stereolithographic 3D printing of soft tissue engineering scaffolds, Biomaterials 140 (2017) 170-188.
[15] S. Gomez, M.D. Vlad, J. Lopez, E. Fernandez, Design and properties of 3D scaffolds for bone tissue engineering, Acta Biomater 42 (2016) 341-350.
[16] S.J.P. Callens, R.J.C. Uyttendaele, L.E. Fratila-Apachitei, A.A. Zadpoor, Substrate curvature as a cue to guide spatiotemporal cell and tissue organization, Biomaterials 232 (2020) 119739.
[17] A. Ranella, M. Barberoglou, S. Bakogianni, C. Fotakis, E. Stratakis, Tuning cell adhesion by controlling the roughness and wettability of 3D micro/nano silicon structures, Acta Biomater 6(7) (2010) 2711-20.
[18] J. Wang, A. Quach, M.E. Brasch, C.E. Turner, J.H. Henderson, On-command on/off switching of progenitor cell and cancer cell polarized motility and aligned morphology via a cytocompatible shape memory polymer scaffold, Biomaterials 140 (2017) 150-161.
[19] J.W. Lee, G. Ahn, J.Y. Kim, D.W. Cho, Evaluating cell proliferation based on internal pore size and 3D scaffold architecture fabricated using solid freeform fabrication technology, J Mater Sci Mater Med 21(12) (2010) 3195-205.

[20] S. Miot, T. Woodfield, A.U. Daniels, R. Suetterlin, I. Peterschmitt, M. Heberer, C.A. van Blitterswijk, J. Riesle, I. Martin, Effects of scaffold composition and architecture on human nasal chondrocyte redifferentiation and cartilaginous matrix deposition, Biomaterials 26(15) (2005) 2479-89.
[21] J. Wang, H. Ma, X. Jin, J. Hu, X. Liu, L. Ni, P.X. Ma, The effect of scaffold architecture on odontogenic differentiation of human dental pulp stem cells, Biomaterials 32(31) (2011) 7822-30.
[22] E.M. Sussman, M.C. Halpin, J. Muster, R.T. Moon, B.D. Ratner, Porous implants modulate healing and induce shifts in local macrophage polarization in the foreign body reaction, Ann Biomed Eng 42(7) (2014) 1508-16.
[23] S.I. Roohani-Esfahani, P. Newman, H. Zreiqat, Design and Fabrication of 3D printed Scaffolds with a Mechanical Strength Comparable to Cortical Bone to Repair Large Bone Defects, Sci Rep 6 (2016) 19468.
[24] A.L. Olivares, E. Marsal, J.A. Planell, D. Lacroix, Finite element study of scaffold architecture design and culture conditions for tissue engineering, Biomaterials 30(30) (2009) 6142-9.
[25] H. Jiang, Y. Qian, C. Fan, Y. Ouyang, Polymeric Guide Conduits for Peripheral Nerve Tissue Engineering, Front Bioeng Biotechnol 8 (2020) 582646.
[26] C. Cha, F. Piraino, A. Khademhosseini, Microfabrication Technology in Tissue Engineering, Tissue Engineering2014, pp. 283-310.
[27] X. Wang, M. Lin, Y. Kang, Engineering Porous beta-Tricalcium Phosphate (beta-TCP) Scaffolds with Multiple Channels to Promote Cell Migration, Proliferation, and Angiogenesis, ACS Appl Mater Interfaces 11(9) (2019) 9223-9232.
[28] D.W. Hutmacher, Scaffolds in tissue engineering bone and cartilage, Biomaterials 21(24) (2000) 2529-2543.
[29] Y. Cao, G. Mitchell, A. Messina, L. Price, E. Thompson, A. Penington, W. Morrison, A. O'Connor, G. Stevens, J. Cooper-White, The influence of architecture on degradation and tissue ingrowth into three-dimensional poly(lactic-co-glycolic acid) scaffolds in vitro and in vivo, Biomaterials 27(14) (2006) 2854-64.
[30] F. Chen, M. Wang, J. Wang, X. Chen, X. Li, Y. Xiao, X. Zhang, Effects of hydroxyapatite surface nano/micro-structure on osteoclast formation and activity, J Mater Chem B 7(47) (2019) 7574-7587.
[31] D. Yang, J. Xiao, B. Wang, L. Li, X. Kong, J. Liao, The immune reaction and degradation fate of scaffold in cartilage/bone tissue engineering, Mater Sci Eng C Mater Biol Appl 104 (2019) 109927.
[32] B.D. Smith, D.A. Grande, The current state of scaffolds for musculoskeletal regenerative applications, Nat Rev Rheumatol 11(4) (2015) 213-22.
[33] R.S. Ambekar, B. Kandasubramanian, Progress in the Advancement of Porous Biopolymer Scaffold: Tissue Engineering Application, Industrial & Engineering Chemistry Research 58(16) (2019) 6163-6194.
[34] A. Alblawi, A.S. Ranjani, H. Yasmin, S. Gupta, A. Bit, M. Rahimi-Gorji, Scaffold-free: A developing technique in field of tissue engineering, Comput Methods Programs Biomed 185 (2020) 105148.
[35] D.W. Hutmacher, T.B.F. Woodfield, P.D. Dalton, Chapter 10 - Scaffold Design and Fabrication, in: C.A.V. Blitterswijk, J. De Boer (Eds.), Tissue Engineering (Second Edition), Academic Press, Oxford, 2014, pp. 311-346.

[36] D. Hutmacher, T. Woodfield, P. Dalton, J. Lewis, Chapter 14 - Scaffold design and fabrication, Tissue Eng, Academic Press, Burlington, 2008, pp. 403-454.
[37] H.A. Declercq, T. Desmet, P. Dubruel, M.J. Cornelissen, The role of scaffold architecture and composition on the bone formation by adipose-derived stem cells, Tissue Eng Part A 20(1-2) (2014) 434-44.
[38] V.A. Parfenov, Y.D. Khesuani, S.V. Petrov, P.A. Karalkin, E.V. Koudan, E.K. Nezhurina, F.D.A.S. Pereira, A.A. Krokhmal, A.A. Gryadunova, E.A. Bulanova, I.V. Vakhrushev, I.I. Babichenko, V. Kasyanov, O.F. Petrov, M.M. Vasiliev, K. Brakke, S.I. Belousov, T.E. Grigoriev, E.O. Osidak, E.I. Rossiyskaya, L.B. Buravkova, O.D. Kononenko, U. Demirci, V.A. Mironov, Magnetic levitational bioassembly of 3D tissue construct in space, Science Advances 6(29) (2020) eaba4174.
[39] P.N. Bernal, P. Delrot, D. Loterie, Y. Li, J. Malda, C. Moser, R. Levato, Volumetric Bioprinting of Complex Living-Tissue Constructs within Seconds, Adv Mater 31(42) (2019) e1904209.
[40] F.P.W. Melchels, K. Bertoldi, R. Gabbrielli, A.H. Velders, J. Feijen, D.W. Grijpma, Mathematically defined tissue engineering scaffold architectures prepared by stereolithography, Biomaterials 31(27) (2010) 6909-6916.
[41] J. Song, C. Michas, C.S. Chen, A.E. White, M.W. Grinstaff, From Simple to Architecturally Complex Hydrogel Scaffolds for Cell and Tissue Engineering Applications: Opportunities Presented by Two-Photon Polymerization, Adv Healthc Mater 9(1) (2020) e1901217.
[42] A. Gleadall, D. Visscher, J. Yang, D. Thomas, J. Segal, Review of additive manufactured tissue engineering scaffolds: relationship between geometry and performance, Burns Trauma 6 (2018) 19.
[43] W. Chu, Y. Tan, P. Wang, J. Xu, W. Li, J. Qi, Y. Cheng, Centimeter-Height 3D Printing with Femtosecond Laser Two-Photon Polymerization, Advanced Materials Technologies 3(5) (2018).
[44] Q. Geng, D. Wang, P. Chen, S.C. Chen, Ultrafast multi-focus 3-D nano-fabrication based on two-photon polymerization, Nat Commun 10(1) (2019) 2179.
[45] U. Jammalamadaka, K. Tappa, Recent Advances in Biomaterials for 3D Printing and Tissue Engineering, J Funct Biomater 9(1) (2018).
[46] E.B. Bagley, H.J. Duffey, Recoverable Shear Strain and the Barus Effect in Polymer Extrusion, Transactions of the Society of Rheology 14(4) (1970) 545-553.
[47] T.D. Brown, P.D. Dalton, D.W. Hutmacher, Direct writing by way of melt electrospinning, Adv Mater 23(47) (2011) 5651-7.
[48] S.E. Felix M. Wunner, Joachim Maartens, Onur Bas, Paul D. Dalton, Elena M. De-Juan-Pardo, and Dietmar W. Hutmacher, Design and Development of a Three-Dimensional Printing High-Throughput Melt Electrowriting Technology Platform, 3D Printing and Additive Manufacturing 6(2) (2019) 82-90.
[49] J. Visser, F.P. Melchels, J.E. Jeon, E.M. van Bussel, L.S. Kimpton, H.M. Byrne, W.J. Dhert, P.D. Dalton, D.W. Hutmacher, J. Malda, Reinforcement of hydrogels using three-dimensionally printed microfibres, Nat Commun 6 (2015) 6933.
[50] M. Castilho, V. Mouser, M. Chen, J. Malda, K. Ito, Bi-layered micro-fibre reinforced hydrogels for articular cartilage regeneration, Acta Biomater 95 (2019) 297-306.
[51] N.T. Saidy, F. Wolf, O. Bas, H. Keijdener, D.W. Hutmacher, P. Mela, E.M. De-Juan-Pardo, Biologically Inspired Scaffolds for Heart Valve Tissue Engineering via Melt Electrowriting, Small 15(24) (2019) e1900873.

[52] M. Castilho, A. van Mil, M. Maher, C.H.G. Metz, G. Hochleitner, J. Groll, P.A. Doevendans, K. Ito, J.P.G. Sluijter, J. Malda, Melt Electrowriting Allows Tailored Microstructural and Mechanical Design of Scaffolds to Advance Functional Human Myocardial Tissue Formation, Advanced Functional Materials 28(40) (2018).
[53] T. Jungst, I. Pennings, M. Schmitz, A.J.W.P. Rosenberg, J. Groll, D. Gawlitta, Heterotypic Scaffold Design Orchestrates Primary Cell Organization and Phenotypes in Cocultured Small Diameter Vascular Grafts, Advanced Functional Materials 29(43) (2019).
[54] N. Abbasi, S. Ivanovski, K. Gulati, R.M. Love, S. Hamlet, Role of offset and gradient architectures of 3-D melt electrowritten scaffold on differentiation and mineralization of osteoblasts, Biomater Res 24 (2020) 2.
[55] J.G. Baldwin, F. Wagner, L.C. Martine, B.M. Holzapfel, C. Theodoropoulos, O. Bas, F.M. Savi, C. Werner, E.M. De-Juan-Pardo, D.W. Hutmacher, Periosteum tissue engineering in an orthotopic in vivo platform, Biomaterials 121 (2017) 193-204.
[56] Z. Zhang, M.L. Jorgensen, Z. Wang, J. Amagat, Y. Wang, Q. Li, M. Dong, M. Chen, 3D anisotropic photocatalytic architectures as bioactive nerve guidance conduits for peripheral neural regeneration, Biomaterials 253 (2020) 120108.
[57] C. Blum, K. Schlegelmilch, T. Schilling, A. Shridhar, M. Rudert, F. Jakob, P.D. Dalton, T. Blunk, L.E. Flynn, J. Groll, Extracellular Matrix-Modified Fiber Scaffolds as a Proadipogenic Mesenchymal Stromal Cell Delivery Platform, ACS Biomaterials Science & Engineering 5(12) (2019) 6655-6666.
[58] B. Delalat, F. Harding, B. Gundsambuu, E.M. De-Juan-Pardo, F.M. Wunner, M.L. Wille, M. Jasieniak, K.A.L. Malatesta, H.J. Griesser, A. Simula, D.W. Hutmacher, N.H. Voelcker, S.C. Barry, 3D printed lattices as an activation and expansion platform for T cell therapy, Biomaterials 140 (2017) 58-68.
[59] L.C. Martine, B.M. Holzapfel, J.A. McGovern, F. Wagner, V.M. Quent, P. Hesami, F.M. Wunner, C. Vaquette, E.M. De-Juan-Pardo, T.D. Brown, B. Nowlan, D.J. Wu, C.O. Hutmacher, D. Moi, T. Oussenko, E. Piccinini, P.W. Zandstra, R. Mazzieri, J.P. Levesque, P.D. Dalton, A.V. Taubenberger, D.W. Hutmacher, Engineering a humanized bone organ model in mice to study bone metastases, Nat Protoc 12(4) (2017) 639-663.
[60] F.M. Wunner, M.L. Wille, T.G. Noonan, O. Bas, P.D. Dalton, E.M. De-Juan-Pardo, D.W. Hutmacher, Melt Electrospinning Writing of Highly Ordered Large Volume Scaffold Architectures, Adv Mater 30(20) (2018) e1706570.
[61] T. Tylek, C. Blum, A. Hrynevich, K. Schlegelmilch, T. Schilling, P.D. Dalton, J. Groll, Precisely defined fiber scaffolds with 40 mum porosity induce elongation driven M2-like polarization of human macrophages, Biofabrication 12(2) (2020) 025007.
[62] F. Afghah, C. Dikyol, M. Altunbek, B. Koc, Biomimicry in Bio-Manufacturing: Developments in Melt Electrospinning Writing Technology Towards Hybrid Biomanufacturing, Applied Sciences 9(17) (2019).
[63] T.M. Robinson, D.W. Hutmacher, P.D. Dalton, The Next Frontier in Melt Electrospinning: Taming the Jet, Advanced Functional Materials 29(44) (2019).
[64] G. Taylor, Electrically Driven Jets, Proceedings of the Royal Society of London. Series A, Mathematical and Physical Sciences 313(1515) (1969) 453-475.
[65] J. Melcher, G. Taylor, Electrohydrodynamics: a review of the role of interfacial shear stresses, Annual review of fluid mechanics 1(1) (1969) 111-146.
[66] Y. Pan, L. Zeng, Simulation and Validation of Droplet Generation Process for Revealing Three Design Constraints in Electrohydrodynamic Jet Printing, Micromachines (Basel) 10(2) (2019).

[67] S.K. Singh, A. Subramanian, Phase-field simulations of electrohydrodynamic jetting for printing nano-to-microscopic constructs, RSC Advances 10(42) (2020) 25022-25028.
[68] A.L. Yarin, S. Koombhongse, D.H. Reneker, Bending instability in electrospinning of nanofibers, Journal of Applied Physics 89(5) (2001) 3018-3026.
[69] D.H. Reneker, A.L. Yarin, H. Fong, S. Koombhongse, Bending instability of electrically charged liquid jets of polymer solutions in electrospinning, Journal of Applied Physics 87(9) (2000) 4531-4547.
[70] M.M. Hohman, M. Shin, G. Rutledge, M.P. Brenner, Electrospinning and electrically forced jets. I. Stability theory, Physics of Fluids 13(8) (2001) 2201-2220.
[71] S. Chiu-Webster, J.R. Lister, The fall of a viscous thread onto a moving surface: a 'fluid-mechanical sewing machine', Journal of Fluid Mechanics 569 (2006) 89-111.
[72] T.D. Brown, F. Edin, N. Detta, A.D. Skelton, D.W. Hutmacher, P.D. Dalton, Melt electrospinning of poly(epsilon-caprolactone) scaffolds: phenomenological observations associated with collection and direct writing, Mater Sci Eng C Mater Biol Appl 45 (2014) 698-708.
[73] D.H. Reneker, A.L. Yarin, Electrospinning jets and polymer nanofibers, Polymer 49(10) (2008) 2387-2425.
[74] T. Han, D.H. Reneker, A.L. Yarin, Buckling of jets in electrospinning, Polymer 48(20) (2007) 6064-6076.
[75] G. Collins, J. Federici, Y. Imura, L.H. Catalani, Charge generation, charge transport, and residual charge in the electrospinning of polymers: A review of issues and complications, Journal of Applied Physics 111(4) (2012).
[76] A. Alj, A. Denat, J.P. Gosse, B. Gosse, I. Nakamura, Creation of Charge Carriers in Nonpolar Liquids, IEEE Transactions on Electrical Insulation EI-20(2) (1985) 221-231.
[77] W.F. Schmidt, Elementary Processes in the Development of the Electrical Breakdown of Liquids, IEEE Transactions on Electrical Insulation EI-17(6) (1982) 478-483.
[78] F.J. Higuera, Electrohydrodynamic flow of a dielectric liquid due to autonomous injection of charge by a needle electrode, Physics of Fluids 14(1) (2002) 423-426.
[79] R. Coelho, J. Debeau, Properties of the tip-plane configuration, Journal of Physics D: Applied Physics 4(9) (1971) 1266-1280.
[80] V.E. Kalayci, P.K. Patra, Y.K. Kim, S.C. Ugbolue, S.B. Warner, Charge consequences in electrospun polyacrylonitrile (PAN) nanofibers, Polymer 46(18) (2005) 7191-7200.
[81] G.B. Brière, Electrical conduction in purified polar liquids, British Journal of Applied Physics 15(4) (1964) 413-417.
[82] H.J. Plumley, Conduction of Electricity by Dielectric Liquids at High Field Strengths, Physical Review 59(2) (1941) 200-207.
[83] S. Tripatanasuwan, D.H. Reneker, Corona discharge from electrospinning jet of poly(ethylene oxide) solution, Polymer 50(8) (2009) 1835-1837.
[84] G.M. Sessler, Chapter 6 - Polymeric Electrets, in: D.A. Seanor (Ed.), Electrical Properties of Polymers, Academic Press1982, pp. 241-284.
[85] Y. Arita, S. Sha Shiratori, K. Ikezaki, A method for detection and visualization of charge trapping sites in amorphous parts in crystalline polymers, Journal of Electrostatics 57(3) (2003) 263-271.
[86] K. Hayashi, K. Yoshino, Y. Inuishi, Temperature Dependence of Carrier Mobility in Polyethylene Terephthalate, Japanese Journal of Applied Physics 12(7) (1973) 1089-1090.
[87] J. Lowell, Absorption and conduction currents in polymers: a unified model, Journal of Physics D: Applied Physics 23(2) (1990) 205-210.

[88] Y. Filatov, A. Budyka, V. Kirichenko, Electrospinning of micro-and nanofibers: fundamentals in separation and filtration processes, J. Eng. Fibers Fabrics 3 (2007) 488.
[89] Q.C. Peiffer, M. de Ruijter, J. van Duijn, D. Crottet, E. Dominic, J. Malda, M. Castilho, Melt electrowriting onto anatomically relevant biodegradable substrates: Resurfacing a diarthrodial joint, Materials & Design (2020).
[90] H. Ding, K. Cao, F. Zhang, W. Boettcher, R.C. Chang, A Fundamental Study of Charge Effects on Melt Electrowritten Polymer Fibers, Materials & Design 178 (2019).
[91] M. Ignatova, T. Yovcheva, A. Viraneva, G. Mekishev, N. Manolova, I. Rashkov, Study of charge storage in the nanofibrous poly(ethylene terephthalate) electrets prepared by electrospinning or by corona discharge method, European Polymer Journal 44(7) (2008) 1962-1967.
[92] H. Gao, W. He, Y.-B. Zhao, D.M. Opris, G. Xu, J. Wang, Electret mechanisms and kinetics of electrospun nanofiber membranes and lifetime in filtration applications in comparison with corona-charged membranes, Journal of Membrane Science 600 (2020).
[93] L.H. Catalani, G. Collins, M. Jaffe, Evidence for Molecular Orientation and Residual Charge in the Electrospinning of Poly(butylene terephthalate) Nanofibers, Macromolecules 40(5) (2007) 1693-1697.
[94] L.S. McCarty, G.M. Whitesides, Electrostatic charging due to separation of ions at interfaces: contact electrification of ionic electrets, Angew Chem Int Ed Engl 47(12) (2008) 2188-207.
[95] E. Németh, V. Albrecht, G. Schubert, F. Simon, Polymer tribo-electric charging: dependence on thermodynamic surface properties and relative humidity, Journal of Electrostatics 58(1-2) (2003) 3-16.
[96] E. Zhmayev, H. Zhou, Y.L. Joo, Modeling of non-isothermal polymer jets in melt electrospinning, Journal of Non-Newtonian Fluid Mechanics 153(2-3) (2008) 95-108.
[97] G. Floudas, L. Hilliou, D. Lellinger, I. Alig, Shear-Induced Crystallization of Poly(ε-caprolactone). 2. Evolution of Birefringence and Dichroism, Macromolecules 33(17) (2000) 6466-6472.
[98] E. Zhmayev, D. Cho, Y.L. Joo, Modeling of melt electrospinning for semi-crystalline polymers, Polymer 51(1) (2010) 274-290.
[99] J.I. Lauritzen, J.D. Hoffman, Theory of Formation of Polymer Crystals with Folded Chains in Dilute Solution, J Res Natl Bur Stand A Phys Chem 64A(1) (1960) 73-102.
[100] G. Lamberti, A direct way to determine iPP density nucleation from DSC isothermal measurements, Polymer Bulletin 52(6) (2004) 443-449.
[101] E. Zhmayev, D. Cho, Y.L. Joo, Electrohydrodynamic quenching in polymer melt electrospinning, Physics of Fluids 23(7) (2011) 073102.
[102] D. Sun, C. Chang, S. Li, L. Lin, Near-Field Electrospinning, Nano Letters 6(4) (2006) 839-842.
[103] J.U. Park, M. Hardy, S.J. Kang, K. Barton, K. Adair, D.K. Mukhopadhyay, C.Y. Lee, M.S. Strano, A.G. Alleyne, J.G. Georgiadis, P.M. Ferreira, J.A. Rogers, High-resolution electrohydrodynamic jet printing, Nat Mater 6(10) (2007) 782-9.
[104] M. Lee, H.Y. Kim, Toward nanoscale three-dimensional printing: nanowalls built of electrospun nanofibers, Langmuir 30(5) (2014) 1210-4.
[105] Y.S. Park, J. Kim, J.M. Oh, S. Park, S. Cho, H. Ko, Y.K. Cho, Near-Field Electrospinning for Three-Dimensional Stacked Nanoarchitectures with High Aspect Ratios, Nano Lett 20(1) (2020) 441-448.

[106] B. Zhang, J. He, X. Li, F. Xu, D. Li, Micro/nanoscale electrohydrodynamic printing: from 2D to 3D, Nanoscale 8(34) (2016) 15376-88.
[107] S. Chiu-Webster, J.R. Lister, The fall of a viscous thread onto a moving surface: a 'fluid-mechanical sewing machine', Journal of Fluid Mechanics 569 (2006).
[108] N.M. Ribe, J.R. Lister, S. Chiu-Webster, Stability of a dragged viscous thread: Onset of "stitching" in a fluid-mechanical "sewing machine", Physics of Fluids 18(12) (2006).
[109] P.T. Brun, N.M. Ribe, B. Audoly, A numerical investigation of the fluid mechanical sewing machine, Physics of Fluids 24(4) (2012).
[110] G. Hochleitner, J.F. Hümmer, R. Luxenhofer, J. Groll, High definition fibrous poly(2-ethyl-2-oxazoline) scaffolds through melt electrospinning writing, Polymer 55(20) (2014) 5017-5023.
[111] Y. Su, Z. Zhang, Y. Wan, Y. Zhang, Z. Wang, L.H. Klausen, P. Huang, M. Dong, X. Han, B. Cui, M. Chen, A hierarchically ordered compacted coil scaffold for tissue regeneration, NPG Asia Materials 12(1) (2020).
[112] S.W. Morris, J.H. Dawes, N.M. Ribe, J.R. Lister, Meandering instability of a viscous thread, Phys Rev E Stat Nonlin Soft Matter Phys 77(6 Pt 2) (2008) 066218.
[113] G. Hochleitner, F. Chen, C. Blum, P.D. Dalton, B. Amsden, J. Groll, Melt electrowriting below the critical translation speed to fabricate crimped elastomer scaffolds with non-linear extension behaviour mimicking that of ligaments and tendons, Acta Biomater 72 (2018) 110-120.
[114] A. Youssef, A. Hrynevich, L. Fladeland, A. Balles, J. Groll, P.D. Dalton, S. Zabler, The Impact of Melt Electrowritten Scaffold Design on Porosity Determined by X-Ray Microtomography, Tissue Eng Part C Methods 25(6) (2019) 367-379.
[115] O. Bas, D. D'Angella, J.G. Baldwin, N.J. Castro, F.M. Wunner, N.T. Saidy, S. Kollmannsberger, A. Reali, E. Rank, E.M. De-Juan-Pardo, D.W. Hutmacher, An Integrated Design, Material, and Fabrication Platform for Engineering Biomechanically and Biologically Functional Soft Tissues, ACS Appl Mater Interfaces 9(35) (2017) 29430-29437.
[116] F.M. Wunner, S. Florczak, P. Mieszczanek, O. Bas, E.M. De-Juan-Pardo, D.W. Hutmacher, 5.13 Electrospinning With Polymer Melts – State of the Art and Future Perspectives, Comprehensive Biomaterials II2017, pp. 217-235.
[117] T.D. Brown, A. Slotosch, L. Thibaudeau, A. Taubenberger, D. Loessner, C. Vaquette, P.D. Dalton, D.W. Hutmacher, Design and fabrication of tubular scaffolds via direct writing in a melt electrospinning mode, Biointerphases 7(1-4) (2012) 13.
[118] J.C. Kade, P.D. Dalton, Polymers for Melt Electrowriting, Adv Healthc Mater (2020) e2001232.
[119] M.A. Woodruff, D.W. Hutmacher, The return of a forgotten polymer—Polycaprolactone in the 21st century, Progress in Polymer Science 35(10) (2010) 1217-1256.
[120] D. Nahm, F. Weigl, N. Schaefer, A. Sancho, A. Frank, J. Groll, C. Villmann, H.-W. Schmidt, P.D. Dalton, R. Luxenhofer, A versatile biomaterial ink platform for the melt electrowriting of chemically-crosslinked hydrogels, Materials Horizons 7(3) (2020) 928-933.
[121] J.N. Haigh, T.R. Dargaville, P.D. Dalton, Additive manufacturing with polypropylene microfibers, Mater Sci Eng C Mater Biol Appl 77 (2017) 883-887.
[122] S. Florczak, T. Lorson, T. Zheng, M. Mrlik, D.W. Hutmacher, M.J. Higgins, R. Luxenhofer, P.D. Dalton, Melt electrowriting of electroactive poly(vinylidene difluoride) fibers, Polymer International 68(4) (2019) 735-745.

[123] Q. Chen, X. Mei, Z. Shen, D. Wu, Y. Zhao, L. Wang, X. Chen, G. He, Z. Yu, K. Fang, D. Sun, Direct write micro/nano optical fibers by near-field melt electrospinning, Opt Lett 42(24) (2017) 5106-5109.
[124] F.-L. He, X. Deng, Y.-Q. Zhou, T.-D. Zhang, Y.-L. Liu, Y.-J. Ye, D.-C. Yin, Controlled release of antibiotics from poly-ε-caprolactone/polyethylene glycol wound dressing fabricated by direct-writing melt electrospinning, Polymers for Advanced Technologies 30(2) (2019) 425-434.
[125] G. Hochleitner, M. Kessler, M. Schmitz, A.R. Boccaccini, J. Teßmar, J. Groll, Melt electrospinning writing of defined scaffolds using polylactide-poly(ethylene glycol) blends with 45S5 bioactive glass particles, Materials Letters 205 (2017) 257-260.
[126] M. Castilho, D. Feyen, M. Flandes-Iparraguirre, G. Hochleitner, J. Groll, P.A.F. Doevendans, T. Vermonden, K. Ito, J.P.G. Sluijter, J. Malda, Melt Electrospinning Writing of Poly-Hydroxymethylglycolide-co-epsilon-Caprolactone-Based Scaffolds for Cardiac Tissue Engineering, Adv Healthc Mater 6(18) (2017).
[127] J. He, P. Xia, D. Li, Development of melt electrohydrodynamic 3D printing for complex microscale poly (epsilon-caprolactone) scaffolds, Biofabrication 8(3) (2016) 035008.
[128] T. Jungst, M.L. Muerza-Cascante, T.D. Brown, M. Standfest, D.W. Hutmacher, J. Groll, P.D. Dalton, Melt electrospinning onto cylinders: effects of rotational velocity and collector diameter on morphology of tubular structures, Polymer International 64(9) (2015) 1086-1095.
[129] N.C. Paxton, R. Daley, D.P. Forrestal, M.C. Allenby, M.A. Woodruff, Auxetic tubular scaffolds via melt electrowriting, Materials & Design 193 (2020).
[130] J.T. McCann, M. Marquez, Y. Xia, Melt Coaxial Electrospinning: A Versatile Method for the Encapsulation of Solid Materials and Fabrication of Phase Change Nanofibers, Nano Letters 6(12) (2006) 2868-2872.
[131] C. Grosshaus, E. Bakirci, M. Berthel, A. Hrynevich, J.C. Kade, G. Hochleitner, J. Groll, P.D. Dalton, Melt Electrospinning of Nanofibers from Medical-Grade Poly(epsilon-Caprolactone) with a Modified Nozzle, Small (2020) e2003471.
[132] N.T. Saidy, T. Shabab, O. Bas, D.M. Rojas-González, M. Menne, T. Henry, D.W. Hutmacher, P. Mela, E.M. De-Juan-Pardo, Melt Electrowriting of Complex 3D Anatomically Relevant Scaffolds, Frontiers in Bioengineering and Biotechnology 8 (2020).
[133] D. Shin, S. Choi, J. Kim, A. Regmi, J. Chang, Direct-Printing of Functional Nanofibers on 3D Surfaces Using Self-Aligning Nanojet in Near-Field Electrospinning, Advanced Materials Technologies 5(6) (2020).
[134] G. Hochleitner, A. Youssef, A. Hrynevich, J.N. Haigh, T. Jungst, J. Groll, P.D. Dalton, Fibre pulsing during melt electrospinning writing, BioNanoMaterials 17(3-4) (2016).
[135] P.B. Warren, Z.G. Davis, M.B. Fisher, Parametric control of fiber morphology and tensile mechanics in scaffolds with high aspect ratio geometry produced via melt electrowriting for musculoskeletal soft tissue engineering, J Mech Behav Biomed Mater 99 (2019) 153-160.
[136] D. Shin, J. Kim, J. Chang, Experimental study on jet impact speed in near-field electrospinning for precise patterning of nanofiber, Journal of Manufacturing Processes 36 (2018) 231-237.
[137] Y. Jin, Q. Gao, C. Xie, G. Li, J. Du, J. Fu, Y. He, Fabrication of heterogeneous scaffolds using melt electrospinning writing: Design and optimization, Materials & Design 185 (2020).
[138] M. Castilho, G. Hochleitner, W. Wilson, B. van Rietbergen, P.D. Dalton, J. Groll, J. Malda, K. Ito, Mechanical behavior of a soft hydrogel reinforced with three-dimensional printed microfibre scaffolds, Sci Rep 8(1) (2018) 1245.

[139] F.M. Wunner, J. Maartens, O. Bas, K. Gottschalk, E.M. De-Juan-Pardo, D.W. Hutmacher, Electrospinning writing with molten poly (ε-caprolactone) from different directions – Examining the effects of gravity, Materials Letters 216 (2018) 114-118.
[140] A. Hrynevich, B.S. Elci, J.N. Haigh, R. McMaster, A. Youssef, C. Blum, T. Blunk, G. Hochleitner, J. Groll, P.D. Dalton, Dimension-Based Design of Melt Electrowritten Scaffolds, Small 14(22) (2018) e1800232.
[141] K.F. Eichholz, D.A. Hoey, Mediating human stem cell behaviour via defined fibrous architectures by melt electrospinning writing, Acta Biomater 75 (2018) 140-151.
[142] F. Tourlomousis, H. Ding, D.M. Kalyon, R.C. Chang, Melt Electrospinning Writing Process Guided by a "Printability Number", Journal of Manufacturing Science and Engineering 139(8) (2017).
[143] F.M. Wunner, P. Mieszczanek, O. Bas, S. Eggert, J. Maartens, P.D. Dalton, E.M. De-Juan-Pardo, D.W. Hutmacher, Printomics: the high-throughput analysis of printing parameters applied to melt electrowriting, Biofabrication 11(2) (2019) 025004.
[144] C.B. Dayan, F. Afghah, B.S. Okan, M. Yıldız, Y. Menceloglu, M. Culha, B. Koc, Modeling 3D melt electrospinning writing by response surface methodology, Materials & Design 148 (2018) 87-95.
[145] S. Liao, B. Langfield, N. Ristovski, C. Theodoropoulos, J. Hardt, K.A. Blackwood, S.D. Yambem, S.D. Gregory, M.A. Woodruff, S. Powell, Effect of humidity on melt electrospun polycaprolactone scaffolds, BioNanoMaterials 17(3-4) (2016).
[146] S. De Vrieze, T. Van Camp, A. Nelvig, B. Hagström, P. Westbroek, K. De Clerck, The effect of temperature and humidity on electrospinning, Journal of Materials Science 44(5) (2009) 1357-1362.
[147] T.D. Brown, P.D. Dalton, D.W. Hutmacher, Melt electrospinning today: An opportune time for an emerging polymer process, Progress in Polymer Science 56 (2016) 116-166.
[148] K.A. Blackwood, N. Ristovski, S. Liao, N. Bock, J. Ren, G.T.S. Kirby, M.M. Stevens, R. Steck, M.A. Woodruff, Improving Electrospun Fibre Stacking with Direct Writing for Developing Scaffolds for Tissue Engineering for Non-load Bearing Bone, Springer International Publishing, Cham, 2015, pp. 125-128.
[149] N. Ristovski, N. Bock, S. Liao, S.K. Powell, J. Ren, G.T. Kirby, K.A. Blackwood, M.A. Woodruff, Improved fabrication of melt electrospun tissue engineering scaffolds using direct writing and advanced electric field control, Biointerphases 10(1) (2015) 011006.
[150] G. Hochleitner, T. Jungst, T.D. Brown, K. Hahn, C. Moseke, F. Jakob, P.D. Dalton, J. Groll, Additive manufacturing of scaffolds with sub-micron filaments via melt electrospinning writing, Biofabrication 7(3) (2015) 035002.
[151] C. Xie, Q. Gao, P. Wang, L. Shao, H. Yuan, J. Fu, W. Chen, Y. He, Structure-induced cell growth by 3D printing of heterogeneous scaffolds with ultrafine fibers, Materials & Design 181 (2019).
[152] C.M. Brennan, K.F. Eichholz, D.A. Hoey, The effect of pore size within fibrous scaffolds fabricated using melt electrowriting on human bone marrow stem cell osteogenesis, Biomed Mater 14(6) (2019) 065016.
[153] Y. Zhang, Z. Zhang, Y. Wang, Y. Su, M. Chen, 3D myotube guidance on hierarchically organized anisotropic and conductive fibers for skeletal muscle tissue engineering, Materials Science and Engineering: C 116 (2020).
[154] F. Blaudez, S. Ivanovski, D. Ipe, C. Vaquette, A comprehensive comparison of cell seeding methods using highly porous melt electrowriting scaffolds, Materials Science and Engineering: C 117 (2020).

[155] S. Bertlein, D. Hikimoto, G. Hochleitner, J. Hummer, T. Jungst, M. Matsusaki, M. Akashi, J. Groll, Development of Endothelial Cell Networks in 3D Tissues by Combination of Melt Electrospinning Writing with Cell-Accumulation Technology, Small 14(2) (2018).
[156] Y. Han, J. Dong, Design, modeling and testing of integrated ring extractor for high resolution electrohydrodynamic (EHD) 3D printing, Journal of Micromechanics and Microengineering 27(3) (2017).
[157] N. Martinez-Prieto, M. Abecassis, J. Xu, P. Guo, J. Cao, K.F. Ehmann, Feasibility of Fiber-Deposition Control by Secondary Electric Fields in Near-Field Electrospinning, Journal of Micro and Nano-Manufacturing 3(4) (2015).
[158] I. Liashenko, J. Rosell-Llompart, A. Cabot, Ultrafast 3D printing with submicrometer features using electrostatic jet deflection, Nat Commun 11(1) (2020) 753.
[159] I.E. Rebrov, K.I. Lukanina, T.E. Grigoriev, A.V. Bakirov, S.V. Krasheninnikov, P.V. Dmitryakov, R.A. Kamyshinsky, C.G. Antipova, S.N. Chvalun, V. Yu. Khomich, Enhanced electrospinning: multi-level fiber alignment by control of electrohydrodynamic jet motion for tissue engineering, Chemical Engineering Journal (2020).
[160] X. You, P. Guo, Active Control of Fabricating Nanofibrous Wavy/Helical Arrays Using Near-Field Electrospinning, ASME 2018 13th International Manufacturing Science and Engineering Conference, 2018.
[161] G. Hochleitner, E. Fursattel, R. Giesa, J. Groll, H.W. Schmidt, P.D. Dalton, Melt Electrowriting of Thermoplastic Elastomers, Macromol Rapid Commun 39(10) (2018) e1800055.
[162] O. Urbanek, P. Sajkiewicz, F. Pierini, The effect of polarity in the electrospinning process on PCL/chitosan nanofibres' structure, properties and efficiency of surface modification, Polymer 124 (2017) 168-175.
[163] U. Stachewicz, C.A. Stone, C.R. Willis, A.H. Barber, Charge assisted tailoring of chemical functionality at electrospun nanofiber surfaces, Journal of Materials Chemistry 22(43) (2012).
[164] F.P.W. Melchels, M.A.N. Domingos, T.J. Klein, J. Malda, P.J. Bartolo, D.W. Hutmacher, Additive manufacturing of tissues and organs, Progress in Polymer Science 37(8) (2012) 1079-1104.
[165] J.S. Lee, J.M. Hong, J.W. Jung, J.H. Shim, J.H. Oh, D.W. Cho, 3D printing of composite tissue with complex shape applied to ear regeneration, Biofabrication 6(2) (2014) 024103.
[166] D.W. Hutmacher, Scaffolds in tissue engineering bone and cartilage, Biomaterials 21(24) (2000) 2529-43.
[167] T.B.F. Woodfield, J. Malda, J. de Wijn, F. Peters, J. Riesle, C.A. van Blitterswijk, Design of porous scaffolds for cartilage tissue engineering using a three-dimensional fiber-deposition technique, Biomaterials 25(18) (2004) 4149-4161.
[168] B.S. Kim, J.S. Lee, G. Gao, D.W. Cho, Direct 3D cell-printing of human skin with functional transwell system, Biofabrication 9(2) (2017) 025034.
[169] J.E. Jeon, C. Vaquette, T.J. Klein, D.W. Hutmacher, Perspectives in multiphasic osteochondral tissue engineering, Anat Rec (Hoboken) 297(1) (2014) 26-35.
[170] J. Li, L. He, C. Zhou, Y. Zhou, Y.Y. Bai, F.Y. Lee, J.J. Mao, 3D printing for regenerative medicine: From bench to bedside, Mrs Bulletin 40(2) (2015) 145-153.
[171] A.M. Yousefi, M.E. Hoque, R.G. Prasad, N. Uth, Current strategies in multiphasic scaffold design for osteochondral tissue engineering: A review, J Biomed Mater Res A 103(7) (2015) 2460-81.
[172] D.W. Hutmacher, T.B.F. Woodfield, P.D. Dalton, Scaffold design and fabrication, in: C. van Blitterswijk, J. De Boer (Eds.), Tissue Engineering, Elsevier, Amsterdam, 2014, pp. 311-346.

[173] P.D. Dalton, C. Hostert, K. Albrecht, M. Moeller, J. Groll, Structure and Properties of Urea-Crosslinked Star Poly[(ethylene oxide)-ran-(propylene oxide)] Hydrogels, Macromolecular Bioscience 8(10) (2008) 923-931.
[174] S.J. Kim, D.H. Jang, W.H. Park, B.M. Min, Fabrication and characterization of 3-dimensional PLGA nanofiber/microfiber composite scaffolds, Polymer 51(6) (2010) 1320-1327.
[175] S. Soliman, S. Pagliari, A. Rinaldi, G. Forte, R. Fiaccavento, F. Pagliari, O. Franzese, M. Minieri, P. Di Nardo, S. Licoccia, E. Traversa, Multiscale three-dimensional scaffolds for soft tissue engineering via multimodal electrospinning, Acta Biomaterialia 6(4) (2010) 1227-1237.
[176] L. Moroni, R. Schotel, D. Hamann, J.R. de Wijn, C.A. van Blitterswijk, 3D Fiber-Deposited Electrospun Integrated Scaffolds Enhance Cartilage Tissue Formation, Advanced Functional Materials 18(1) (2008) 53-60.
[177] G.-H. Yang, F. Mun, G. Kim, Direct electrospinning writing for producing 3D hybrid constructs consisting of microfibers and macro-struts for tissue engineering, Chemical Engineering Journal 288 (2016) 648-658.
[178] S.W. Chung, N.P. Ingle, G.A. Montero, S.H. Kim, M.W. King, Bioresorbable elastomeric vascular tissue engineering scaffolds via melt spinning and electrospinning, Acta Biomaterialia 6(6) (2010) 1958-1967.
[179] G.M. Gratson, F. Garcia-Santamaria, V. Lousse, M.J. Xu, S.H. Fan, J.A. Lewis, P.V. Braun, Direct-write assembly of three-dimensional photonic crystals: Conversion of polymer scaffolds to silicon hollow-woodpile structures, Advanced Materials 18(4) (2006) 461-465.
[180] G.M. Gratson, M.J. Xu, J.A. Lewis, Microperiodic structures - Direct writing of three-dimensional webs, Nature 428(6981) (2004) 386-386.
[181] M.L. Muerza-Cascante, D. Haylock, D.W. Hutmacher, P.D. Dalton, Melt electrospinning and its technologization in tissue engineering, Tissue Engineering Part B-Reviews 21(2) (2015) 187-202.
[182] G. Hochleitner, A. Youssef, A. Hrynevich, J.N. Haigh, T. Jungst, J. Groll, P.D. Dalton, Fibre pulsing during melt electrospinning writing, BioNanoMaterials 17(3) (2016) 159-171.
[183] R. McMaster, C. Hoefner, A. Hrynevich, C. Blum, M. Wiesner, K. Wittmann, T.R. Dargaville, P. Bauer-Kreisel, J. Groll, P.D. Dalton, T. Blunk, Tailored Melt Electrowritten Scaffolds for the Generation of Sheet-Like Tissue Constructs from Multicellular Spheroids, Adv Healthc Mater 8(7) (2019) e1801326.
[184] M.D. Monzón, I. Gibson, A.N. Benítez, L. Lorenzo, P.M. Hernández, M.D. Marrero, Process and material behavior modeling for a new design of micro-additive fused deposition, The International Journal of Advanced Manufacturing Technology 67(9-12) (2013) 2717-2726.
[185] T. Jungst, M.L. Muerza-Cascante, T.D. Brown, M. Standfest, D.W. Hutmacher, J. Groll, P.D. Dalton, Melt electrospinning onto cylinders: effects of rotational velocity and collector diameter on morphology of tubular structures, Polym Int 64(9) (2015) 1086-1095.
[186] P.T. Brun, B. Audoly, N.M. Ribe, T.S. Eaves, J.R. Lister, Liquid Ropes: A Geometrical Model for Thin Viscous Jet Instabilities, Physical Review Letters 114(17) (2015) 174501.
[187] M.K. Jawed, F. Da, J. Joo, E. Grinspun, P.M. Reis, Coiling of elastic rods on rigid substrates, Proc Natl Acad Sci U S A 111(41) (2014) 14663-8.
[188] B. Zhang, B. Seong, V. Nguyen, D. Byun, 3D printing of high-resolution PLA-based structures by hybrid electrohydrodynamic and fused deposition modeling techniques, Journal of Micromechanics and Microengineering 26(2) (2016) 025015.
[189] H. Yuk, X. Zhao, A New 3D Printing Strategy by Harnessing Deformation, Instability, and Fracture of Viscoelastic Inks, Adv Mater 30(6) (2018).

[190] N. Schaefer, D. Janzen, E. Bakirci, A. Hrynevich, P.D. Dalton, C. Villmann, 3D Electrophysiological Measurements on Cells Embedded within Fiber-Reinforced Matrigel, Adv Healthc Mater 8(5) (2019) e1801226.
[191] M. Mao, J. He, Z. Li, K. Han, D. Li, Multi-directional cellular alignment in 3D guided by electrohydrodynamically-printed microlattices, Acta Biomater 101 (2020) 141-151.
[192] M. de Ruijter, A. Hrynevich, J.N. Haigh, G. Hochleitner, M. Castilho, J. Groll, J. Malda, P.D. Dalton, Out-of-Plane 3D-Printed Microfibers Improve the Shear Properties of Hydrogel Composites, Small 14(8) (2018).
[193] Z. Yin, Y. Huang, Y. Duan, H. Zhang, Mechano-electrospinning (MES), Electrohydrodynamic Direct-Writing for Flexible Electronic Manufacturing, Springer Singapore, Singapore, 2018, pp. 31-65.
[194] I. Liashenko, A. Hrynevich, P.D. Dalton, Designing Outside the Box: Unlocking the Geometric Freedom of Melt Electrowriting using Microscale Layer Shifting, Adv Mater (2020) e2001874.
[195] O. Diegel, A. Nordin, D. Motte, DfAM Strategic Design Considerations, A Practical Guide to Design for Additive Manufacturing, Springer Singapore, Singapore, 2019, pp. 41-70.
[196] A. Bauhofer, C. Daraio, Neural networks for trajectory evaluation in direct laser writing, The International Journal of Advanced Manufacturing Technology 107(5-6) (2020) 2563-2577.
[197] N.M. Ribe, M. Habibi, D. Bonn, Liquid Rope Coiling, Annual Review of Fluid Mechanics 44(1) (2012) 249-266.
[198] M.K. Jawed, P.-T. Brun, P.M. Reis, A Geometric Model for the Coiling of an Elastic Rod Deployed Onto a Moving Substrate, Journal of Applied Mechanics 82(12) (2015).
[199] A. Hrynevich, I. Liashenko, P.D. Dalton, Accurate Prediction of Melt Electrowritten Laydown Patterns from Simple Geometrical Considerations, Advanced Materials Technologies (2020).
[200] E. Bakirci, N. Schaefer, O. Dahri, A. Hrynevich, P. Strissel, R. Strick, P.D. Dalton, C. Villmann, Melt Electrowritten In Vitro Radial Device to Study Cell Growth and Migration, Advanced Biosystems (2020).
[201] M.J. Divvela, Y.L. Joo, Discretized modeling of beads-on-a-string morphology from electrically driven, conducting, and viscoelastic polymer jets, Journal of Applied Physics 121(13) (2017).
[202] M.J. Divvela, L.M. Shepherd, M.W. Frey, Y.L. Joo, Discretized Modeling of Motionless Printing Based on Retarded Bending Motion and Deposition Control of Electrically Driven Jet, 3D Printing and Additive Manufacturing 5(3) (2018) 248-256.
[203] M.J. Divvela, Y.L. Joo, Design principles in continuous inkjet electrohydrodynamic printing from discretized modeling and image analysis, Journal of Manufacturing Processes 54 (2020) 413-419.
[204] C.P. Carroll, Y.L. Joo, Discretized modeling of electrically driven viscoelastic jets in the initial stage of electrospinning, Journal of Applied Physics 109(9) (2011).
[205] C. Ru, J. Chen, Z. Shao, M. Pang, J. Luo, A novel mathematical model for controllable near-field electrospinning, AIP Advances 4(1) (2014).
[206] G. Zheng, W. Li, X. Wang, H. Wang, D. Sun, L. Lin, Experiment and simulation of coiled nanofiber deposition behavior from near-field electrospinning, 2010 IEEE 5th International Conference on Nano/Micro Engineered and Molecular Systems, 2010, pp. 284-288.
[207] J. Tonkin, Modelling electrospun fibres using differential equations, (2020).
[208] J. Schindelin, I. Arganda-Carreras, E. Frise, V. Kaynig, M. Longair, T. Pietzsch, S. Preibisch, C. Rueden, S. Saalfeld, B. Schmid, J.Y. Tinevez, D.J. White, V. Hartenstein, K. Eliceiri, P.

Tomancak, A. Cardona, Fiji: an open-source platform for biological-image analysis, Nat Methods 9(7) (2012) 676-82.
[209] Y. Fukushima, curvspace, 2020. https://www.mathworks.com/matlabcentral/fileexchange/7233-curvspace. (Accessed May 23 2020).
[210] I. Arganda-Carreras, R. Fernandez-Gonzalez, A. Munoz-Barrutia, C. Ortiz-De-Solorzano, 3D reconstruction of histological sections: Application to mammary gland tissue, Microsc Res Tech 73(11) (2010) 1019-29.
[211] P.D. Dalton, J. Mey, Neural interactions with materials, Front Biosci (Landmark Ed) 14 (2009) 769-95.
[212] A.T. Nguyen, S.R. Sathe, E.K. Yim, From nano to micro: topographical scale and its impact on cell adhesion, morphology and contact guidance, J Phys Condens Matter 28(18) (2016) 183001.
[213] J. Kim, W. Kim, G. Kim, Scaffold with micro/nanoscale topographical cues fabricated using E-field-assisted 3D printing combined with plasma-etching for enhancing myoblast alignment and differentiation, Applied Surface Science 509 (2020).
[214] D. Hodde, J. Gerardo-Nava, V. Wohlk, S. Weinandy, S. Jockenhovel, A. Kriebel, H. Altinova, H.W. Steinbusch, M. Moller, J. Weis, J. Mey, G.A. Brook, Characterisation of cell-substrate interactions between Schwann cells and three-dimensional fibrin hydrogels containing orientated nanofibre topographical cues, Eur J Neurosci 43(3) (2016) 376-87.
[215] S. Lee, M.K. Leach, S.A. Redmond, S.Y. Chong, S.H. Mellon, S.J. Tuck, Z.Q. Feng, J.M. Corey, J.R. Chan, A culture system to study oligodendrocyte myelination processes using engineered nanofibers, Nat Methods 9(9) (2012) 917-22.
[216] A. Omidinia-Anarkoli, J.W. Ephraim, R. Rimal, L. De Laporte, Hierarchical fibrous guiding cues at different scales influence linear neurite extension, Acta Biomater 113 (2020) 350-359.
[217] L.R. Lizarraga-Valderrama, C.S. Taylor, F. Claeyssens, J.W. Haycock, J.C. Knowles, I. Roy, Unidirectional neuronal cell growth and differentiation on aligned polyhydroxyalkanoate blend microfibres with varying diameters, J Tissue Eng Regen Med 13(9) (2019) 1581-1594.
[218] H.K. Frost, T. Andersson, S. Johansson, U. Englund-Johansson, P. Ekstrom, L.B. Dahlin, F. Johansson, Electrospun nerve guide conduits have the potential to bridge peripheral nerve injuries in vivo, Sci Rep 8(1) (2018) 16716.
[219] J.I. Kim, T.I. Hwang, L.E. Aguilar, C.H. Park, C.S. Kim, A Controlled Design of Aligned and Random Nanofibers for 3D Bi-functionalized Nerve Conduits Fabricated via a Novel Electrospinning Set-up, Sci Rep 6 (2016) 23761.
[220] Y. Hu, F. Zhang, W. Zhong, Y. Liu, Q. He, M. Yang, H. Chen, X. Xu, K. Bian, J. Xu, J. Li, Y. Shen, H. Zhang, Transplantation of neural scaffolds consisting of dermal fibroblast-reprogrammed neurons and 3D silk fibrous materials promotes the repair of spinal cord injury, J Mater Chem B 7(47) (2019) 7525-7539.
[221] A. Kriebel, M. Rumman, M. Scheld, D. Hodde, G. Brook, J. Mey, Three-dimensional configuration of orientated fibers as guidance structures for cell migration and axonal growth, J Biomed Mater Res B Appl Biomater 102(2) (2014) 356-65.
[222] E.L. Gill, W. Wang, R. Liu, Y.Y.S. Huang, Additive batch electrospinning patterning of tethered gelatin hydrogel fibres with swelling-induced fibre curling, Additive Manufacturing 36 (2020).
[223] D. Janzen, E. Bakirci, A. Wieland, C. Martin, P.D. Dalton, C. Villmann, Cortical Neurons form a Functional Neuronal Network in a 3D Printed Reinforced Matrix, Adv Healthc Mater 9(9) (2020) e1901630.

[224] N.T. Nguyen, J.H. Kim, Y.H. Jeong, Identification of sagging in melt-electrospinning of microfiber scaffolds, Mater Sci Eng C Mater Biol Appl 103 (2019) 109785.
[225] R.J. McMurtrey, Patterned and functionalized nanofiber scaffolds in three-dimensional hydrogel constructs enhance neurite outgrowth and directional control, J Neural Eng 11(6) (2014) 066009.
[226] D. Tarus, L. Hamard, F. Caraguel, D. Wion, A. Szarpak-Jankowska, B. van der Sanden, R. Auzely-Velty, Design of Hyaluronic Acid Hydrogels to Promote Neurite Outgrowth in Three Dimensions, ACS Appl Mater Interfaces 8(38) (2016) 25051-9.
[227] G.J. Bryce, R.R. Ribchester, Culture of isolated embryonic chick dorsal root ganglia at an air-liquid interface: a simple method for studying the mechanism and control of neurite outgrowth, Journal of Neuroscience Methods 48(1) (1993) 89-97.
[228] J.G. Hardy, Z.Z. Khaing, S. Xin, L.W. Tien, C.E. Ghezzi, D.J. Mouser, R.C. Sukhavasi, R.C. Preda, E.S. Gil, D.L. Kaplan, C.E. Schmidt, Into the groove: instructive silk-polypyrrole films with topographical guidance cues direct DRG neurite outgrowth, J Biomater Sci Polym Ed 26(17) (2015) 1327-42.

Acknowledgements

I would like to thank the people who were around during the work on this thesis for their guidance, friendship and exchange of ideas, concerns, achievements and failures. I am happy I have met all of you during my time at FMZ. In more detail I want to express my gratitude to my PhD committee members, Prof. Dr. Paul D. Dalton for the inspiration and excitement for science throughout his career, PD Dr. Gary G. Brook for introducing me to neuroscience back in my Master's and our collaboration work, including the research visit in Aachen and Prof. Dr. Robert Luxenhofer for his help in improving this thesis.

I also want to thank the head of the department, Prof. Dr. Jürgen Groll for gathering excellent people and facilities under one roof and giving me the opportunity to be a part of the FMZ team, and the platform leaders, Dr. Jörg Teßmar, Prof. Dr. Uwe Gbureck and Dr. Andrea Ewald for valuable discussions.

In this journey I owe a ton of appreciation to Moataz, Jodie, Daimon and Mylene for being the best colleague and friend, sharing SEM tricks and the apartment with me and an inspiring transformation of a hybrid student through a competitor (the toughest one) into a colleague, respectively. While Tomasz and Gernot were my examples in research expertise at the start, Ievgenii and Ezgi made my last half a year phenomenally efficient and fun! More thanks go to Carina, Christoph, June, Fleurine, Bilge, Juliane, Tom, Berat, Ali, Philipp, Judith, Michael and Kai as well as the rest of my colleagues in Würzburg.

My research would have been much harder, if at all possible, without the technical skills of Harald Hümpfer and Anton Hofmann, an assistance with the organizational matters from Tanja Dambach, Birgit Langner-Bischof and Dr. Schröder-Köhne, and funding by the European Research Council, German Federation of Industrial Research Associations and Volkswagen Foundation.

The most personal part of this section is addressed to my family and friends for their love, support in difficult times and rare, yet critically valuable moments together. The very last and the most special thanks go to my mom for her belief in me combined with a continuous motivational support and my significant other, Sylvia, for her adorable stubbornness, patience and understanding.

Affidavit

I hereby confirm that my thesis entitled “Enhancement of geometric complexity and predictability of melt electrowriting for biomedical applications” is the result of my own work. I did not receive any help or support from commercial consultants. All sources and / or materials applied are listed and specified in the thesis.

Furthermore, I confirm that this thesis has not yet been submitted as part of another examination process neither in identical nor in similar form.

Place, Date Signature

Eidesstattliche Erklärung

Hiermit erkläre ich an Eides statt, die Dissertation „Fortentwicklung von geometrischer Komplexität und Kalkulierbarkeit des Melt Electrowriting für biomedizinische Anwendungen“ eigenständig, d.h. insbesondere selbständig und ohne Hilfe eines kommerziellen Promotionsberaters, angefertigt und keine anderen als die von mir angegebenen Quellen und Hilfsmittel verwendet zu haben.

Ich erkläre außerdem, dass die Dissertation weder in gleicher noch in ähnlicher Form bereits in einem anderen Prüfungsverfahren vorgelegen hat.

Ort, Datum Unterschrift